Chapter 20
HF Over-the-Horizon Radar

James M. Headrick

Naval Research Laboratory (retired)

Stuart J. Anderson

Australian Defence Science and Technology Organisation

20.1 INTRODUCTION

Beyond-the-horizon detection of terrestrial targets at ranges of thousands of kilometers can be achieved by radars operating in the high-frequency (HF) band (3 to 30 MHz). This very long range coverage is obtained by using *skywave* propagation, that is, reflecting the radar signals from the ionosphere. HF ground wave (surface wave) propagation over the sea has been used for intermediate but still over-the-horizon distances, up to several hundred kilometers. Occasionally HF radar systems also find applications in line-of-sight applications at short range. This chapter focuses predominantly on skywave radar, though much of the discussion applies equally to surface wave radar. Rather than amalgamate discussion of the two radar configurations throughout the chapter, the distinctive features of HF surface wave radar are treated separately in an appendix at the end of the chapter.

In one sense. the development of HF skywave radar can be traced back to the 1920s, when skywave echoes were identified,[1] but the first HF radar systems were not deployed until the 1950s.[2] Since then, skywave radar has evolved to address applications such as the detection and tracking of aircraft, ballistic and cruise missiles, and ships.[3–15] In addition to detecting "skin" echoes from targets of interest, HF radar is useful for observing various forms of high-altitude atmospheric ionization, both natural, including those associated with aurorae and meteors, and artificial, including the interaction of spacecraft and ballistic missiles with the ionospheric plasma.[16–19] Further, the wavelengths used are of the same order as ocean surface gravity waves, and this correspondence can be exploited to provide information on the wave directional spectrum, ocean currents, and, by inference, surface winds.[5] Indeed, scattering from the sea can often be employed as a radar cross section (RCS) amplitude reference and is a widely used diagnostic tool. The narrow-band waveforms employed, the low frequencies, and the nature of the transmission path make the spatial resolution coarse when compared with higher-frequency radars, but the doppler resolution can be exceedingly fine. The magnitude and doppler distribution of the echoes from the distant Earth's surface (often termed *backscatter*, though that term should be reserved for monostatic radars) are major factors in setting system dynamic range, spectral purity, and signal processing requirements.
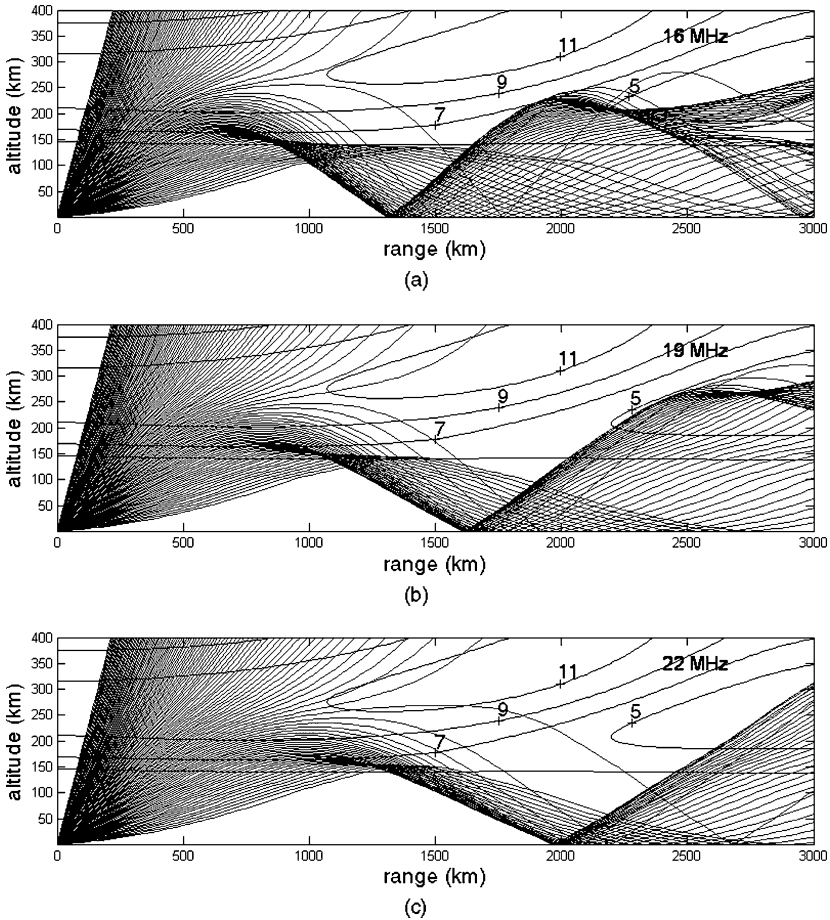
FIGURE 20.1   Ray-tracing through a model ionosphere, showing the variation of the radar footprint with carrier frequency. The contours map the plasma frequency or electron density.

For effective radar operation, environmental parameters that affect radar performance need to be determined in real time, defined as that interval in which there are no large-scale changes in the ionosphere. Typically, this is of the order of 10–30 minutes. Transmission-path information is generally derived from adjunct vertical and oblique sounders as well as by using the radar itself as a sounder. An ionospheric electron density model complex enough to enable adequate sounding interpretation is required. Ionospheric or transmission path statistical climatologies and forecasts are necessary for radar design and for development of site-specific models. In addition, other users in the HF spectrum must be observed continuously and operating frequencies selected to avoid interference.

The essential features of skywave propagation can be seen in Figure 20.1. The ionosphere, being an ionized gas with free electrons, will reflect all radar signals when the radar frequency is less than the *plasma frequency* given by

$$f_P \cong 9 \times 10^{-6} \sqrt{N_e} \tag{20.1}$$
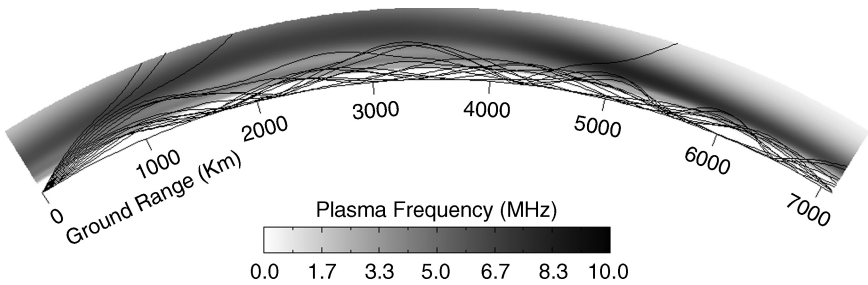
FIGURE 20.2 Numerically computed rays illustrating multiple hop propagation across the equatorial zone. The elevated peak electron density near the equator at ~2500 km is the Appleton anomaly.

where f_P is in MHz and N_e is in electrons per cubic meter. For a given elevation angle α, if the radar frequency exceeds $f_p/\sin\alpha$ at the height of maximum ionization, rays launched at higher elevation angles will escape, resulting in a so-called *skip* or *dead* zone within which the Earth's surface is not illuminated. Beyond this skip zone, energy is returned to the Earth, reaching a maximum range when the rays leaving the antenna are horizontal. Useful range coverage will lie between these limits, which define the *one-hop zone*.

As shown in Figure 20.2, a multiplicity of hops may exist, and energy may even circle the earth; clutter echoes from these long ranges can seriously degrade radar performance. A comparison of Figures 20.1*a,* 20.1*b,* and 20.1*c* reveals that different range extents are illuminated by using different operating frequencies, with longer starting ranges requiring higher frequencies. In the examples shown, 16 MHz illuminates ranges from 1300 to 3000 km, whereas 19 MHz illuminates ranges from 1650 to 2750 km whereas 22 MHz illuminates from 1950 to 2750 km. Hence, the farthest edge of the footprint need not increase with frequency, depending on the prevailing ionospheric conditions. In this example, a single ionospheric layer is considered. Normally, there are two or three distinct layers such that signals may partially penetrate the lower layers to be reflected by a higher layer. As a consequence, the relationship between the range to a target and the measured echo time delay becomes multivalued, with unknown parameters such as layer heights that must be estimated by various techniques as described later in this chapter.

To illustrate the operating principles of a skywave radar, Figure 20.3 presents a map showing multiple surveillance tasks assigned to a hypothetical radar with 360° azimuthal coverage. Five sectors of current surveillance activity are shown, each addressing a particular mission as indicated, each mission consisting of a number of *dwell interrogation regions (DIRs)*. The electronically steered radar transmit beam steps through these DIRs, in some assigned sequence, illuminating each DIR with an appropriate waveform for a corresponding interval during which the receiving system acquires a coherent time series of echo samples. The coherent integration time (CIT) depends on the type of observation but is almost always in the range of 1–100 seconds. Each transmitter footprint is analyzed by forming simultaneous contiguous receive beams, on the order of 1/2° wide at 15 MHz in the case of the U.S. Navy ROTHR and the Australian Jindalee and JORN radars, which equates to a 10 km cross-range resolution at a 1200 km range. The task-specific requirements on DIR revisit rates determine the sequencing of the DIR interrogations and, of course, set the limit on how many tasks can be addressed.
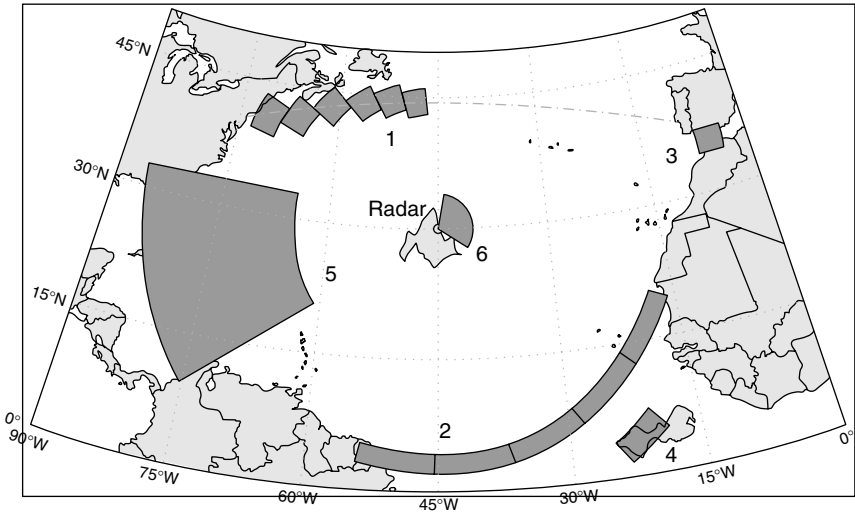
FIGURE 20.3   Some coverage and tasking options for hypothetical HF radars on a (fictitious) mid-Atlantic island. The coverage regions numbered 1–5 correspond to skywave radar missions as follows: 1, air route monitoring; 2, barrier surveillance; 3, strategic waterway monitoring; 4, ballistic missile launch detection; and 5, remote sensing and hurricane tracking. The sector designated 6 is representative of HF surface wave radar coverage.

Consider the set of tasks and DIRs shown in Figure 20.3. Task 1 would require only short CITs, 1–2 s, say, if the aircraft is assumed to be large, and would need revisits perhaps every minute, as the flight is not expected to maneuver so the track will be well-behaved and observed position errors would be due to ionospheric fluctuations. Only the single DIR containing the aircraft need be interrogated. Task 2, barrier surveillance, if concerned with ship traffic, can afford to relax the revisit time to tens of minutes as ships move so slowly, but in order to achieve detection, long CITs of 20–30 s are required to separate the ship echoes from the sea clutter in the doppler spectrum. Even so, the radar can step across the barrier arc, with plenty of time to interleave a Task 1 dwell between addressing successive DIRs in Task 2. If the barrier Task 2 were concerned with aircraft, with a CIT of 1–2 s, the revisits would need to be frequent enough to achieve the desired probability of detection before the aircraft had time to cross the barrier. One approach is to widen the barrier by processing more range cells or by reducing the waveform bandwidth and allowing the range cells to grow wider, but this may fail if the ionosphere does not support propagation over the increased range depth. Another possibility is to increase the revisit interval over a subset of the DIRs. The relative priority of Tasks 1 and 2 would also need to be taken into account.

Task 4 (ballistic missile launch detection) would require much more frequent surveillance if a launch were believed to be imminent, or else the missile might escape from the radar footprint without being detected. Assume a CIT of 5 seconds and a tolerable revisit interval of 10 s. Tasks 1 and 4 could be interleaved, for example, by carrying out five dwells of Task 4, and then one of Task 1, and then repeating this pattern. Task 3 is concerned with slow-moving ships, so the revisit interval could be tens

of minutes, but a long CIT of perhaps 20–30 s is required in order to separate the ship echoes from the sea clutter in the doppler spectrum. During this time, Task 4's requirements would be violated. Tasks 3 and 4, as defined, are incompatible.

Task 5 (remote sensing of ocean conditions) would have a much lower priority as it deals with slowly varying phenomena, so it would need only occasional revisiting. The smaller sector shown as Task 6, extending to a range of 400 km, is representative of the coverage of an HF surface wave radar, as used for protecting the approaches to a port, for example.

This example is typical of the scheduling and resource allocation problem that is central to HF skywave radar operations. Compromises are often unavoidable. The situation is further complicated by the continuous variation of ionospheric propagation conditions, which must be monitored and used to guide tasking, as when bad ionospheric "weather" is likely to preclude certain missions.

Almost invariably, the sectors and, indeed, the individual DIRs within a sector will require different carrier frequencies, even for a given range, as the ionosphere may vary substantially across the full range and azimuth extent of the active coverage. The defining characteristic of HF skywave radar is that the radar operator must select frequencies that are optimum for the various tasks and adapt these frequencies to the ever-changing ionosphere.

This chapter sets out to explain the principal features of HF skywave radar as it is presently implemented, emphasizing the physical considerations that govern system design and performance.

20.2 THE RADAR EQUATION

A form of the radar equation, Eq. 20.2, can be used to point to aspects of HF radar that are significantly different from radars that use higher frequencies. These differences include adaptation to environment, frequency and waveform selection, radar cross section, path losses, multipath effects, noise, interference, antenna gain, spatial resolution, and clutter. For the case of noise-limited detection, the radar equation takes the form

$$\frac{S}{N} = \frac{P_{av}\,G_t\,G_r\,T\lambda^2\sigma\,F_p}{(4\pi)^3 L_p L_s N_0 R^4} \tag{20.2}$$

where

S/N = output signal-to-noise ratio
P_{av} = average transmitted power
G_t = transmitter antenna gain
G_r = receiver antenna gain
T = coherent processing time
λ = wavelength
σ = target radar cross section
F_p = propagation-path factor
N_0 = noise power per unit bandwidth
L_p, L_s = transmission-path and system losses
R = distance between radar and target

These parameters are explained briefly as follows:

Antennas, G_t and G_r: A common convention for HF-band radars is to include the effect of the ground in the antenna performance characterization, and that convention will be used here. For example, a half-wave dipole in free space has a maximum gain over an isotrope of 2.15 dB. If that antenna is oriented vertically, just above but not touching a perfectly conducting earth, its maximum gain will be increased by a factor of 4, or 6 dB, to 8.15 dB at 0° elevation angle. Because the Earth is never perfect, its conductivity and dielectric constant are factors in determining antenna performance. The electrical properties of the Earth are a much stronger factor for vertical polarization than for horizontal; however, terrain features and surface roughness are important for both polarizations.

Coherent processing time, T: For ranges beyond the skip distance, HF radar returns almost invariably contain Earth backscatter at the same ranges as targets. Doppler processing is used to separate targets from Earth backscatter; hence, coherent samples are acquired over an interval *T,* which may exceed 100 s, though it is usually in the range of 1–20 s.

Wavelength (λ): The wavelength or operating frequency must be selected so that the transmitted energy is reflected by the ionosphere to illuminate the desired area of the Earth. The spectrum of the emissions must be constrained not to interfere with other users. Because both the ionosphere and the HF-band occupancy distributions are time-varying parameters, adaptive radar management is required.

Radar cross section (RCS), σ: The radar cross section of conventional targets will generally be a function of frequency, polarization, and aspect angle, but at HF, the target dimensions are typically of the same order as the wavelength, so scattering behavior is different from that observed at higher frequencies. Scattering also occurs from the environment—clutter—so models of the scattering coefficient per unit area of land and ocean surfaces, or per unit volume of the turbulent ionosphere, are used to provide effective RCS values for Eq. 20.2 when those natural scatterers are the "targets" of interest. Thus, for the RCS of Earth clutter, the normalized surface scattering coefficient $\sigma°$ is multiplied by the resolution cell size A. The important resolution cell size factors, viz. receiver antenna beamwidth and spectral bandwidth, are not explicitly contained in Eq. 20.2 (Clutter frequently sets the limit to target detectability; in which case, it is the signal-to-clutter ratio rather than the signal-to-noise ratio that is of interest. Accordingly, a different form of the radar equation must then be employed.)

Propagation factors (F_p): Several propagation phenomena, including Faraday polarization rotation, ground-reflection multipath, multiple hop propagation, and ionospheric focusing may need to be included in the equation, depending on the scenario of interest. Faraday rotation refers to the variation of the polarization of the signal incident on the target as a function of time and distance, arising from its propagation through the magnetized ionospheric plasma; linearly polarized transmitted signals often arrive in the target zone with a rotated axis of polarization but still essentially linearly polarized. Since many targets have RCS that vary with polarization, an important result is that the most favorable polarization will illuminate the target recurrently. The spatial scale of the polarization "fringes" in the radar footprint is typically in the range 10–100 km, and the change of frequency needed to rotate the plane of polarization by 90° at a given location in the radar footprint (the polarization bandwidth) is of the order of 100 kHz, so differential

effects may be significant. Of course, polarization will also fluctuate at the receiving antenna as a consequence of the time-varying return path.

Noise (N_o): For radars operating in the HF band, the receiver internal noise is almost always less than the external noise.

Losses (L_p, L_s): The loss term L_p contains the two-way losses along the path traversed, including ionospheric absorption and ground-reflection losses; L_s represents any radar system losses. Ionospheric losses, while predicted on a statistical basis, can constitute a major unknown in real-time radar operation.

Range (R): The range in Eq. 20.2 is the "slant range," that is, the length of the skywave path between target and radar, not the distance as measured along the Earth's surface. The ionospheric reflection height needs to be used to convert this slant range to great-circle ground distance. The apparent range to a particular target may take on more than one value since multiple paths may exist.

With these interpretations, the radar equation (Eq. 20.2) can be used to model the performance of skywave radars when noise, not clutter, is setting the limit to target detectability, noting that the complexity and statistical nature of ionospheric propagation and the external noise environment means that it is often necessary to apply the equation to probability distributions, not scalar values of the parameters. When the target's velocity places its doppler shift beyond those of any clutter returns, the noise-limited model is appropriate, but there are two important situations where this is not the case. The first is ship detection, where the intrinsic doppler spread of sea clutter routinely extends beyond the typical doppler shifts of most ship echoes. The second case is the phenomenon of spread doppler clutter, which arises from plasma instabilities and turbulence, especially post-sunset and at high and low latitudes. The equivalent velocity of this type of clutter can extend to hundreds of meters per second, masking even fast aircraft returns. These topics are addressed in Section 20.8. Dealing with clutter-limited situations is a vital part of the radar designer's task, requiring a detailed understanding of the phenomena and their distributions.

20.3 FACTORS INFLUENCING SKYWAVE RADAR DESIGN

Principal Differences Between HF and Microwave Radar. Before analyzing HF skywave radar systems in detail in the sections that follow and describing those properties of the environment that impact their design and performance, it is instructive to summarize the principle differences between skywave radar and conventional microwave radar. This provides a cautionary reminder not to extrapolate too readily from the familiar characteristics of the microwave domain to the HF band.

HF skywave radars operate at ranges about an order of magnitude greater than microwave long-range air surveillance radars. The HF radar wavelength is hundreds of times greater, so the antennas are proportionately larger, as much as two or three kilometers in length if they are to see ships, but considerably less if only aircraft are to be detected. Transmitter average power might be on the order of several hundred kilowatts for a skywave radar, but on the order of a few kilowatts for a microwave ATC radar. The observation time (CIT) for skywave systems can range from one to many tens of seconds, but is on the order of tens of milliseconds for microwave radar.

The long observation time for a skywave radar is needed to obtain the necessary echo signal energy to ensure reliable target detection as well as to obtain the long integration times needed for effective doppler processing. The ionosphere has a dominating influence on skywave radar, whereas the normal atmosphere has very little effect on microwave radar. The skywave radar's frequency and other parameters are driven primarily by the need to propagate via the ionosphere. Constraints imposed by propagation and the availability of unoccupied frequency channels dictate that the range resolution of HF radars is not nearly as good as that of microwave systems. The HF transmitter has to maintain stringent control of its radiated signal spectrum so as to avoid interference to other users of the HF spectrum. (A similar consideration applies to microwave radars, but not to the extent that it does at HF. Military microwave radars like to have available a wide spectral width for purposes of electronic protection and to extract more detailed target information, but the increasing demands of civilian wireless services have reduced the available spectrum available to microwave radars to the point where it is limiting performance.)

The sensitivity of microwave radars is limited by receiver noise, but the sensitivity of HF radars is limited by external noise that enters the receiver through the antenna. This external noise is due not only to natural mechanisms such as thunderstorms but to the signals from the many HF transmitters throughout the world. Both microwave and HF radars can be limited by the large echo signals from land or sea, though in HF skywave radars, the problem is particularly severe. Doppler processing is essential under such conditions. For some aircraft, the radar cross section at HF is significantly larger than that at microwaves. Many HF OTH radars utilize an FM-CW waveform, so widely separated sites are needed to minimize the leakage of the transmitter into the receiver. Microwave radars have used FM-CW waveforms in the past, but in most cases, these have been replaced by waveforms that don't require separate transmitter and receiver sites.

Table 20.1 presents a comparison of some key radar parameters for representative radar systems of each type, and contrasts the ways in which the respective modes of propagation, scattering, noise, and deployment constrain the form and function of radar systems.

Implications for Skywave Radar Design.   From an examination of Table 20.1, it is clear that a skywave radar is not simply a microwave radar scaled up in size by a factor of ~ 1000, that is, in proportion to the wavelength. Referring to the radar equation, the R^{-4} loss term means that, for a representative tenfold increase in detection range of HF over microwave, 40 dB extra range loss accumulates. This cannot all be recovered by radiating more power and increasing antenna gain, for practical engineering reasons and cost, apart from constraints imposed by ionospheric propagation. Coherent (doppler) processing provides the necessary processing gain, but the processing times required—from 1 to 100 s—mean that revisit rates when conducting surveillance over an extended region will fall below acceptable levels unless multiple receive beams are processed in parallel. Designers have explored different trade-offs, in most cases, converging on schemes in which 15–30 receive beams are formed within a broader transmitted beam footprint. The reduced transmitting antenna gain may be compensated by increasing power or coherent processing time.

Even under benign conditions, the ionosphere seldom supports highly coherent propagation over bandwidths greater than ~200 kHz, even when clear channels wide enough to accommodate such waveforms are available, which is infrequently. More typically, clear channels range from 10–50 kHz, so the waveform bandwidth is normally chosen to lie in this range. The corresponding range resolutions extend

from 3–15 km. The cross-range resolution cell dimension $L(R)$ at range R is given by $L \approx \frac{R\lambda}{D}$ where D is the receiving array aperture and λ is the radar wavelength.

TABLE 20.1 Key Differences Between Microwave Radar and HF Skywave Radar (The parameter values quoted here are intended to be broadly representative, rather than an attempt to span all known systems.)

	I. MICROWAVE RADAR	II. HF SKYWAVE RADAR
Type chosen for comparison	Long-range air traffic control such as ARSR-3	Joint aircraft and ship detection, two-site radar such as Jindalee, JORN, and ROTHR
Major antenna dimension (m)	10–15	1000–3000
Average transmit power (kW)	4	400
Antenna radiation pattern	Fully defined by antenna construction	Strongly influenced by ground properties around antenna
Typical operating range (km)	280–450	1000–4000
Minimum range (km)		1000
Range resolution (m)	300	1500–15000
Propagation medium	• Homogeneous or stratified • Nondispersive • Isotropic • Stable • Linear • Nearly constant	• Structured horizontally and vertically, both deterministically and randomly, on many scales • Frequency dispersive • Anisotropic (magnetoionic) • Highly dynamic • Weakly nonlinear • Varies dramatically with time of day, season, etc.
Radar signal propagation path	• Line-of-sight • Usually unique; may have simple ground-reflection multipath • Relatively stable	• Reflected from ionosphere • Multiple paths, resulting in multiple echoes from a single target, at different apparent ranges, bearings, elevation angles, and doppler shifts • Unstable • Poorly known, must be inferred from ancillary sounding systems
Dominant propagation effects on the radar signal	• Multipath interference between direct and surface-reflected signals	• Attenuation • Focusing and defocusing • Polarization transformation • Phase modulation • Wavefront distortion
Target scattering regime	Optical (high frequency), i.e., target size ≫ radar wavelength	Rayleigh – resonance, i.e., target size < or ~ radar wavelength
Clutter	• Can be serious, especially at short ranges • Minimized by narrow beam, short pulse, and doppler processing	Look-down viewing geometry inevitably results in strong ground echoes at the same range as the target, typically 20–80 dB stronger than the target echo
Doppler processing	Widely used for detection of moving targets in clutter	Essential to separate moving targets from strong clutter returns

TABLE 20.1 Key Differences Between Microwave Radar and HF Skywave Radar
(The parameter values quoted here are intended to be broadly representative, rather
than an attempt to span all known systems.) (*Continued*)

	I. MICROWAVE RADAR	II. HF SKYWAVE RADAR
Frequency constraints	Can be serious because of the need for wideband radar systems and by competition for the microwave frequency spectrum by communications and other electromagnetic services	• Bounded above by the statistical availability of skywave propagation to ranges of interest • Bounded below by spectrum availability, antenna size, and the rapid fall-off in target RCS • Must not interfere with other users in the crowded HF spectrum, thus limiting choice of frequency and bandwidth • Must adapt continually to the changing ionosphere so as to maintain illumination of current target region
Noise floor dominated by	Internal receiver noise (thermal, etc.)	Sources (atmospheric, galactic, anthropogenic, etc.)
Siting constraints	• Unobstructed, elevated sites preferred	• Receive array site must be EM quiet, generally rural, to avoid city and industrial noise at HF frequencies • Huge arrays require flat, open spaces to minimize topographic effects on beam patterns • If a bistatic or two-site quasi-monostatic design is adopted, it needs two sites with adequate separation (~100 km) and the correct geographical relationship relative to the coverage arc • Location on the Earth must be such that auroral and equatorial spread doppler echoes don't mask targets

Hence, to achieve $L = 10$ km at 1200 km range when the frequency is 15 MHz, and
thus a resolution cell not too eccentric in shape, requires an array aperture of about
2400 m. Feeding arrays of this size can require hundreds of kilometers of cables or, in
some systems, fiber optics, and raises challenging problems in array calibration. The
transmitting array aperture, assuming ≈ 20 receive beams to be fitted into the transmit
beam, need be only ~ 120 m at this frequency.

It follows from the radar equation and the considerations just discussed that trans-
mit power in the range of 200–1000 kW is generally appropriate for detecting small
aircraft targets over a wide range of conditions. In order to radiate power efficiently,
the transmitting antenna elements tend to be large, resonant structures; for example,
the vertical log-periodic antennas used in the JORN system are up to 43 m tall. In
contrast, the choice of receiving antenna element has traditionally been based on the

precept that efficiency is of low importance for HF reception because external noise is almost always far stronger than internal noise. A more efficient receiving element accepts more signal power but equally more external noise so, *prima facie*, nothing is gained in terms of the signal-to-noise ratio. Cost is thus reduced by employing a small receiving antenna element. Heights of 4–6 m are common.

The look-down geometry of skywave illumination results in strong clutter returns in the same range cell as the target, demanding a high dynamic range able to support clutter-to-target energy ratios in excess of 80 dB. This places severe demands on the spectral purity and dynamic range of the radar waveform generator, transmitting, and receiving systems. High sensitivity has the side effect of revealing the echoes from many natural scatterers in the ionosphere, as well as the spectrum of ground clutter that has been spread in doppler by the fluctuations of the signal propagation path. In order to recognize and suppress these unwanted returns, which can obscure target echoes, an understanding of the underlying physics is essential.

A distinctive requirement of a skywave radar is a suite of auxiliary systems to monitor the state of the ionosphere and the availability of unoccupied channels in which to operate. This reliance on continuous environmental monitoring and the associated ability to adapt the radar parameters and tasking to make best use of the prevailing conditions cannot be satisfied with simple, low dynamic range equipment, for that would fail to reveal many of the phenomena that are setting the threshold for target detection and tracking. Further, a high degree of automation is essential to keep up with the changing environment.

A comparison of principle design parameters of several current and former operational HF skywave radars is presented in Table 20.2, illustrating the diversity of engineering solutions that have been implemented to meet specific mission objectives.

TABLE 20.2   Principal Design Parameters for Some Major HF Skywave Radar Systems, Past and Present

(This information has been compiled from sources that, in some cases, are incomplete. Where only partial information is provided, it may still be useful for comparison purposes. Notes: (i) VLPA denotes vertical log-periodic antenna and (ii) 2-band (*n*-band) linear arrays are usually constructed as contiguous collinear arrays.)

	Jindalee Stage B	JORN-Laverton	AN/FPS-118 ECRS/WCRS	AN/TPS-71 ROTHR	Nostradamus	Steel Yard (Komsomolsk na Amur)
Developer	DSTO, Australia	Telecom Australia GEC-Marconi UK RLM USA-Australia	General Electric USA	Raytheon USA	ONERA, France	NIIDAR, Russia
Year of first target detections	1982	2000	1983	1987	1994	1977
Configuration	Quasi-monostatic	Quasi-monostatic	Quasi-monostatic	Quasi-monostatic	True monostatic	Quasi-monostatic
Tx – Rx site separation (km)	100	80	160	100, 160	n/a	
Max. transmitter power (kW)	160	300	1200	200	50	1500
Tx gain (dB)		18–27	23			
ERP	76 dBW	80 dBW	80 dBW	75 dBW		

TABLE 20.2 Principal Design Parameters for Some Major HF Skywave Radar Systems, Past and Present
(This information has been compiled from sources that, in some cases, are incomplete. Where only partial information is provided, it may still be useful for comparison purposes. Notes: (i) VLPA denotes vertical log-periodic antenna and (ii) 2-band (*n*-band) linear arrays are usually constructed as contiguous collinear arrays.) (*Continued*)

	Jindalee Stage B	JORN-Laverton	AN/FPS-118 ECRS/WCRS	AN/TPS-71 ROTHR	Nostradamus	Steel Yard (Komsomolsk na Amur)
Tx array design	2-band linear array of 8 (low band) and 16 (high band) VLPA antennas	2 adjacent 2-band linear arrays of VLPA antennas; arrays oriented at 90° to each other	3 contiguous 6-band linear arrays of canted dipoles with 41-m tall backscreens, 12 elements per band; arrays oriented at 60°	2-band linear array of 2 × 16 VLPA antennas	Y-shaped array of 3 × 32 biconical elements randomly distributed	2 × vertical curtain arrays of 13 masts × 10 vertically stacked horizontal cage dipoles
Frequency range (MHz)	5–28	5–32	5–28	5–12 10.5–28	6–28	4–30
Tx apertures (m)	137	160, 160	304, 224, 167, 123, 92, 68		3 arms × 128 (long) × 80 (wide)	
Tx azimuth beam steer (deg)	± 45°	± 45°	± 30°	± 32°	360°	
Rx array design	Linear array of 462 5-m fan monopole pairs grouped as 32 overlapped subarrays	2 linear arrays of 480 twin monopole elements; arrays at 90°	3 contiguous linear arrays of 246 × 5.4 m vertical monopoles with 20 m backscreens; arrays at 60°	Linear array of 372 × 5.8 m vertical twin monopoles	Y-shaped array of 3 × 96 7 m biconical elements grouped as 3 × 16 subarrays with random distribution	2 × vertical curtain arrays of 30 masts × 10 vertically stacked horizontal cage dipoles
Rx aperture (m)	2766	2970	1518 / 2440	2580	3 arms × 384 (long) × 80 (wide)	500 (long) × 143 (high)
No. of receive channels	32	480	82	372	48	5
Rx azimuth beam steer	± 45°	± 45°	± 30°	± 45°	360°	
Waveform type	Linear FM/CW	Linear FM/CW	Linear FM/CW	Linear FM/ CW Linear FM/CW	Coded pulse	Binary phase coded pulse
Waveform repetition frequency (Hz)	~ 4–80	~ 4–80	10–60	5–60		10, 16, 20
Waveform bandwidth(kHz)	4–40 typical	4–40 typical	5–40	4.17–100		40
Coherent integration time (s)	1.5– 5 Air mode 15–40 Ship mode	1.5–15 Air mode 15–40 Ship mode	0.7–20.5	1.3–49.2		
Primary mission	Aircraft detection	Aircraft detection	Aircraft detection	Aircraft detection	Aircraft detection	Ballistic missile detection
Secondary missions	Ship detection Remote sensing	Ship detection Remote sensing	Cruise missile detection	Ship detection	Ship detection Remote sensing	Aircraft detection Cruise missile detection

The term quasi-monostatic is used to denote configurations in which the transmit and receive sites are separated, as is often done with radars employing FM-CW waveforms, but not so far apart that the angle subtended at the target is more than ~5°, so the scattering behavior is close to what is observed for exactly monostatic geometry.

20.4 THE IONOSPHERE AND RADIOWAVE PROPAGATION

The solar activity that drives the ionization of the Earth's upper atmosphere is variable on a diurnal, seasonal, and long-term basis with a superimposed random component and occasional major storms and other disturbances. Further, the Earth's lower atmosphere is coupled to the ionosphere by a variety of upward-propagating wave and radiation processes, whereas the Earth's magnetosphere, the region beyond the ionosphere where the solar wind interacts with the Earth's magnetic field, is the source or conduit for corresponding perturbations from above. The ionospheric response to all these external forces is governed not only by inertial effects but also by chemical reactions and by the embedded time-varying electric and magnetic fields that link the ionospheric plasma to the Earth and to the interplanetary medium. As a consequence, the structure of the ionosphere undergoes changes on a wide variety of spatial and temporal scales, which drastically affect its properties as a medium for radiowave propagation.

The primary requirement for radar system design is a quantitative description of the propagation characteristics over the proposed coverage region. Specifically, the radar designer needs a statistical description that will enable matching the transmitted signal, power level, and antenna gain pattern to the supported frequency span, noise levels, propagation loss characteristics, and ray paths to the target region. In addition, the radar operator needs a model with enough sophistication to permit full interpretation of the real-time soundings for operating parameter selection, signal processing, and data analysis. With this latter requirement, a statistical description is usually not adequate, as important features may be lost. For example, under rapidly changing ionospheric conditions, the radar echoes will experience a time-varying doppler shift. Averaging over time would result in a doppler shift tending to zero. Clearly, this is of no value to the operator wishing to compensate for ionospheric motion and hence to retrieve a meaningful estimate of target radial velocity. As a second example, consider the situation where an atmospheric gravity wave (AGW) is propagating through the ionosphere in the vicinity of the control point (ionospheric reflection point) while a target is being tracked. The ionosphere is only ~ 0.1% ionized at the altitudes of interest to HF radar, but waves in the neutral gas, under the restoring force of gravity, transfer their motion to the free electrons via collisions. As the distribution of electrons defines the "reflecting surface" experienced by the radar signals, the apparent bearing and range of the target will fluctuate as the ionospheric "reflecting surface" undulates in response to the AGW. This undulation is known as a traveling ionospheric disturbance (TID). TIDs may have wavelengths of hundreds of kilometers and speeds up to 1000 kilometers per hour. Unless the radar makes appropriate real-time corrections to the target coordinates, tracking accuracy will be severely impaired.

To address these various needs, it is advantageous to adopt corresponding descriptions or models, emphasizing different aspects of the ionosphere and its influence on radiowave propagation and, hence, HF radar performance. In many cases of practical interest, ionospheric models developed originally for HF communications purposes

can be adapted to the radar context, where the main difference is the greater sensitivity of radar observations to dynamical processes. This arises primarily because of the extremely high dynamic range required to accommodate and preserve target echoes in the presence of strong clutter and external noise.

Ionospheric Structure.   The basic physics of ionization and recombination processes leads to a natural division of the ionosphere into a number of regions:

D Region.   This region occupies the lowest altitudes considered. It extends from 50 to 90 km, with electron density increasing rapidly with altitude in the daytime. Its properties reflect the balance between free electron production by the incident solar radiation flux and free electron loss via various electron-ion and electron-neutral recombination processes. Accordingly, the maximum ionization in the D region occurs near the sub–solar point and will be greatest during periods of highest solar activity (sunspot maximum), though it does not achieve densities sufficient to reflect or even significantly refract HF radio waves. The key role of the D region in HF radiowave propagation is signal attenuation via electron-neutral collisions that are frequent at these moderate altitudes where the neutral species density is still relatively high. It is not represented explicitly in some ionospheric models where its effects are accounted for with an empirically derived path-loss calculation.

E Region.   This ionization region extends between about 90 and 130 km in altitude with a maximum near 110 km when sunlit. In addition, there may be anomalous ionization referred to as sporadic E. This latter ionization layer is typically only a few kilometers thick and usually short-lived, often lasting less than an hour; it may be either smooth or patchy, is seasonally and diurnally variable, weakly correlated with solar activity, showing a tendency to favor low sunspot numbers, and has marked variation with latitude. From the propagation perspective, sporadic E holds a special place as the layer providing the most stable propagation over coherent integration times typical of skywave radar. Because it is only ~100 km above the Earth's surface, the maximum range that can be reached via one-hop E-layer propagation is only ~2000 km, though normally the layer is not totally reflecting, so some energy continues upward to the F-layer where it is reflected to reach the Earth's surface at much greater ranges.

F Region.   This is the highest-altitude region of interest for skywave propagation, and it is also the region of greatest electron density. In the daylight hours, the F region sometimes manifests two component layers, especially in summer. The Fl region lies between 130 and 200 km and, like the E region, is directly dependent upon solar radiation; it reaches maximum intensity about 1 h after local noon. The F2 region is variable in both time and geographical location. The altitude of the F2 region peak lies typically between 250 and 350 km at middle latitudes. The F2-region ionization shows marked day-to-day variations and, in general, is not the regular sun follower that the E and F1 regions are.

The simple physical picture of the ionosphere as consisting of several more or less concentric layers must be modified substantially at both low and high latitudes to take into account the effects of the impressed electric and magnetic fields. To begin with, the displacement of the Earth's magnetic axis from its rotational axis means that the ionosphere does not preserve a more or less constant form enveloping a rotating earth. Near the magnetic equator, where the geomagnetic field is close to horizontal, atmospheric tides and associated winds drive the so-called E-region and F-region

dynamos, resulting in an upward drift of the ionospheric plasma and its subsequent descent along the geomagnetic field lines. The resulting electron density depletion at the equator and roughly symmetric enhancements in the vicinity of ~ 20° N/S latitude is known as the *Appleton* or *equatorial anomaly*. Besides causing errors in estimated target range and bearing, the tilted ionospheric "reflecting surface" near the equator can support scattering of incident radiowaves into low-loss elevated trans-equatorial modes (chordal modes) that return strong clutter from the opposite hemisphere, often with highly unstable phase characteristics.

In the polar zones, the near-vertical geomagnetic field lines provide a pathway for charged particles and disturbances of solar and magnetospheric origin to reach ionospheric heights and contribute to ionization processes and plasma transport. The best known phenomena here are the aurorae, which are concentrated in ovals pole-ward of the boundary where the Earth's geomagnetic field lines change from closed (connected to their images in the opposite hemisphere) to open, that is, connected to the interplanetary magnetic field. A wide variety of plasma waves and instabilities populate these regions, producing irregularities that achieve high electron densities and hence, provide strong sources of spread-doppler clutter. They have been known to impact skywave radar systems severely.

Ionospheric Variability.　While all ionospheric properties are time-varying, from an OTHR perspective, it is useful to separate the "fast" processes or "dynamics" from the "slow" or "structural" variability. A phenomenon is termed *dynamical* relative to a radar observation process if it occurs on a timescale commensurate with the corresponding process timescale, such as (i) pulse/waveform repetition interval, (ii) coherent integration (dwell) time, (iii) scan revisit time, or (iv) mission / track lifetime. Dynamical processes impact directly on how one should process the received signals or perform tracking. Slow processes, such as the 11-year solar cycle, seasonal changes, and the diurnal cycle of the E- and F-layers can generally be treated as quasi-stationary background processes that set up the ionospheric structure at any given time, within which fast processes may occur. An exception to this classification arises with the dawn and dusk terminators, that is, the day-night boundaries; sweeping around the Earth at 1600 km/hr, they produce abrupt changes in the ionosphere and trigger large-scale instabilities.

Structural Variability.　The day-night cycle produces drastic changes in the ionization distribution within the ionosphere. At night, the D-layer disappears, the E and F regions experience a substantial decrease in ionization, and the equatorial and polar regions are more prone to large-scale perturbations. The extent of diurnal variation can be seen by examining Figure 20.4, which shows measured electron density (expressed in terms of plasma frequency as defined in Eq. 20.1) versus virtual height and time-of-day at a mid-latitude location.* Typically, the diurnal variation requires a radar to vary its operating frequency by more than an octave in frequency to maintain 24-hour surveillance over a fixed target location.

---

* Virtual height is the reflection height computed from signal time delay by assuming that the radiowave travels at the speed of light as if in free space; in fact, the radiowave group velocity in the plasma is lower, so the true height is less. For most purposes, it is more convenient to deal with virtual height, because there are two theorems that dramatically simplify practical calculations. Martyn's theorem shows that complicated oblique skywave ray paths via the true reflection point can be replaced to good approximation with simple rectilinear geometry via the virtual reflection point. The theorem of Breit and Tuve demonstrates that, to good approximation, the time-of-flight is unchanged by this substitution. Davies[21] provides a clear explanation of these useful theorems.
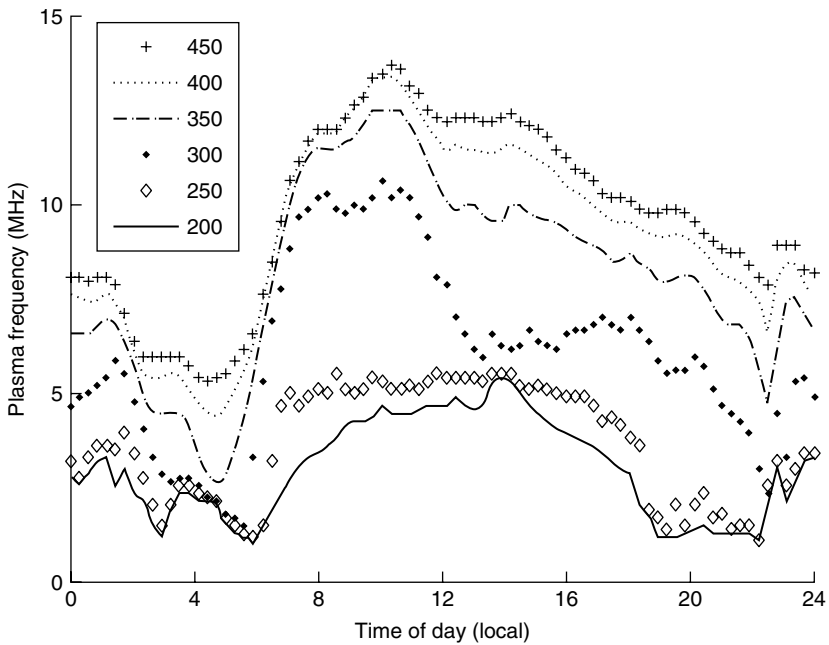
FIGURE 20.4   Diurnal variation of the electron density profile, as measured by the plasma frequency, plotted for various virtual heights (in km). The data was recorded by a vertical incidence sounder at latitude 18.0 S, longitude 144.9 E on 17 September 2002, SSN = 88.

What is more surprising is the day-to-day variability, even at mid-latitudes, which impacts significantly on HF radar performance. The inability to predict reliably even a day in advance is a serious consideration in radar design and scheduling.

An illustration of day-to-day variability is presented in Figure 20.5, which overlays 30 vertical incidence soundings recorded at the same time of day for a month.
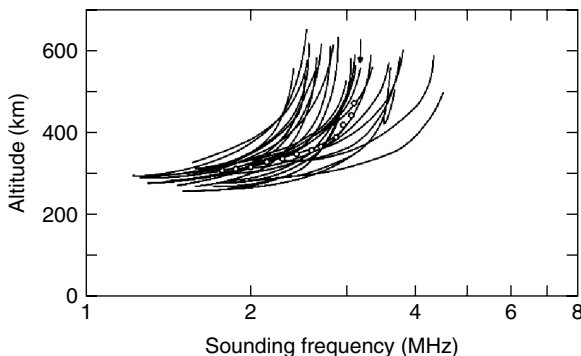

FIGURE 20.5   Comparison of measured vertical incidence ionograms for a fixed time of day over a month with a model-based prediction of the median, denoted by the small circles.

The traces plot the virtual height versus radiowave frequency for the *ordinary* ray (see subsection below on radiowave propagation). Soundings of this type—ionograms— measure the return trip time delay for a signal to travel up to the height at which the electron density is sufficient to reflect it, that is, where the plasma frequency f_p equals the incident radiowave frequency.

Also shown in Figure 20.5 is the corresponding monthly median, taken from the model of Thomason et al.[22] Consider the critical frequency, that is, the highest reflected frequency, corresponding to the ionosphere's peak electron density. The upper and lower deciles depart from the median by typically ± 25%. Over such a range of frequency, terms in the radar equation such as antenna gains, target RCS, and slant range may vary substantially, so radar performance is inevitably statistically distributed. Although it makes sense to use median values for many radar performance modeling calculations, the radar designer should adopt a conservative approach and assume the lowest critical frequency.

Perhaps the most intriguing major cause of systematic variation is the 11-year cycle of solar activity. Various correlated parameters have been defined to measure this activity, including the 10.7 cm solar flux, sunspot number, and various magnetic indices. Figure 20.6 shows the smoothed average sunspot number plotted from 1956, the year of the first validated OTHR detections of military targets (achieved by the *MUSIC* radar at NRL[2]).

Enhanced solar activity impacts on the ionosphere in many ways, but its most significant action from a radar perspective is to produce substantially higher ionization levels that persist at usable levels through the night, so higher radar frequencies can be employed and the minimum achievable range decreases. In addition, the height of the maximum electron density increases, so one-hop propagation can reach greater ranges.
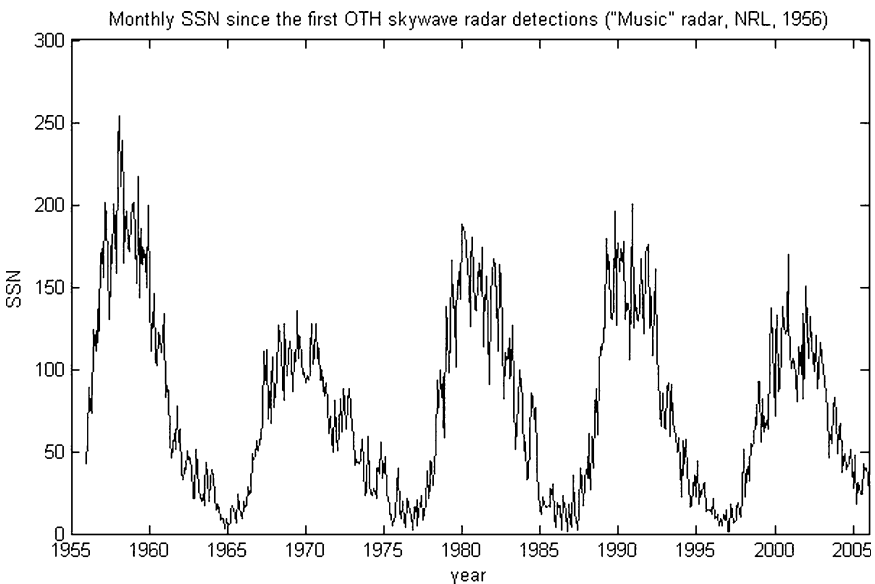
FIGURE 20.6 The variation of the monthly median sunspot number since 1956, the year of the first operational skywave radar detections

Daytime absorption increases for a given frequency because of higher D-layer densities, but this is compensated by access to higher operating frequencies. An increase in the number and severity of magnetic storms and sudden ionospheric disturbances is another consequence of higher solar activity, as are increased post-sunset plasma bubble activity and associated scintillation in equatorial regions, solar flares, and coronal mass ejections all of which disrupt stable propagation. Solar flares are giant explosions on the sun's surface, generally occurring near sunspots, which emit ionizing radiation that penetrates into the D region and dramatically increases absorption. The resulting *sudden ionospheric disturbance* (SID) or *short-wave fade-out* can completely incapacitate a skywave radar for a period from minutes to hours. Perhaps more importantly, although the flare itself is not predictable, the associated burst of particles will start to arrive a few hours later, with most ejected material reaching Earth several days later, seriously disrupting HF propagation. The critical importance of solar activity will be demonstrated in Section 20.13 in the context of radar performance prediction.

Ionospheric Dynamics.   As the radar signals traverse the ionosphere, motions of the plasma medium along the propagation path imprint themselves on the signals in ways that can degrade or obliterate the target information of interest. Skywave radars can be designed to recognize the signatures of these phenomena, adjusting the radar frequency, choice of waveform, and processing to mitigate their effects where necessary. Sometimes the ionospheric motions actually help the radar, for example, by enabling it to discriminate between natural noise and some forms of deliberate interference. Thus, it is vitally important to understand not only the structure of the ionosphere and the opportunities it provides for propagation, but also the motions and disturbances that inhabit it.

The variety of wave types and irregularity of production mechanisms in the ionosphere is enormous, and includes not only those arising naturally but also many induced phenomena such as those resulting from ground-based ionospheric RF heaters or rocket interactions with the ambient plasma. Among the most important from the radar point of view are the following:

- Transient plasma structures associated with ionized meteor trails; at any given location, meteors have a strong diurnal variation and directionality. They are ever-present and constitute a major source of clutter for HF radars.[19]

- Large and medium scale atmospheric gravity waves (AGW) produced by energetic phenomena in the lower atmosphere propagate upward with increasing amplitude until nonlinear processes begin to dominate, resulting in wave breaking. Large AGWs may persist for hours and propagate over global distances, causing serious deviation of incident radiowaves.[23] They are sometimes the major cause of tracking errors.

- Magnetic disturbances originating where the solar wind impacts on the magnetosphere; they propagate earthward and cause resonant oscillations of the geomagnetic field lines permeating the ionosphere. The field lines are "frozen in" to the ionospheric plasma and, hence, the ionosphere vibrates locally at frequencies typically in the range of 10^{-2}–10^0 Hz, imposing a corresponding modulation on any transiting radiowaves.[24] Ship echoes can be obscured by this modulation.

- The equatorial electrojet, part of the global system of fields and currents driven by the dynamo action of winds and tides, is host to small scale field-aligned irregularities with characteristic velocity distributions.[25] Some small-scale plasma instabilities may endure for a fraction of a second, others for tens of seconds, evident to radars as spread-doppler clutter that prevents the detection of small targets.

- Equatorial plasma bubbles often appear after sunset and convect upward through the F region where they contribute to strong diffuse doppler-spread scattering referred to as spread-F.[26] Detection of all targets is difficult when this effect occurs.

- The aurorae are dynamic structures governed by fields and plasma flows in the magnetosphere; strong electric fields aligned with the magnetic field accelerate electrons down into the ionosphere where they produce highly ionized formations that reflect radio waves very efficiently. The resulting doppler-spread echoes are so strong they can incapacitate a radar through its sidelobes.

- Geomagnetic storms and sub-storms result from solar flares and coronal mass ejections. As mentioned earlier, hard X-rays and ultraviolet radiation raise D-layer ionization dramatically with consequent increases in radiowave absorption. Within an hour and for a day or so after, flare-generated particle bursts start to arrive and are channeled down the magnetic field lines at high latitudes, causing ionospheric heating and associated diffusion to lower latitudes, together with a variety of magnetic field perturbations. HF propagation is often severely disrupted.

Models and Their Uses. Knowledge of the conditions to be expected for a particular radar deployment is vital to radar design, as well as providing a guide to echo interpretation and a means to simulation and performance prediction. This type of information, based on decades of ionospheric observations and theory, is conveniently distilled in models that are widely available and used extensively. But even more importantly, from the operational perspective, HF radars must maintain a real-time ionospheric model (RTIM) that is intimately linked with the radar subsystems, serving to guide frequency selection, radiated power, task scheduling, coordinate registration (converting from the radar coordinates of time delay and angle-of-arrival to geographical coordinates), ionospheric mode structure interpretation, and association of multiple tracks from a single target. Unlike the climatological models, RTIMs must be updated continuously with information from an auxiliary network of beacons. Oblique and vertical incidence sounders and transponders have been deployed for this purpose. For instance, the JORN radars exploit approximately 20 sounders and related facilities distributed around the coast of Australia. Radar performance in most operational roles is governed by the fidelity of the adopted RTIM.

It is important to differentiate between models that describe the physical (or physico-chemical) state of the ionosphere and models that describe radiowave propagation characteristics, though the latter are often derived from the former by applying ray-tracing methods, and the former are predominantly derived from radiowave propagation measurements such as point-to-point link statistics and vertical incidence soundings. Both classes are of general applicability to HF communications and geophysical investigations, as well as skywave radar.

Models of the Ionospheric Medium. Models of the ionosphere fall into two categories:

- Climatological models based on sounder, rocket, and satellite measurements. Being derived from statistics, they provide no explicit information on real-time "'weather." that is, irregularities, waves, and other dynamic processes, though measures of variability may be provided. Many early models had their genesis in the large database of recorded ionospheric soundings made during the International Geophysical Year of 1957–1958 and the International Year of the Quiet Sun of 1964–1965. These models,

which focused on the spatial distribution of electron density, were used extensively in early HF radar performance analyses and include ITSA-1, ITS-78, RADAR C, IONCAP, and AMBCOM.[27–32] Lucas [33] provides details of these models and their origins. Some of the prediction methods have not been well documented although widely distributed; also, users frequently "improve" upon a model and prediction method to suit their specific needs. As an example, the model RADAR C[29] is the basic building block of Thomason et al. in NRL Report 8321[22]; however, they added a D region, a collision-frequency distribution, an Earth's magnetic field, a topside electron distribution, an auroral electron-density modification,[34] and other features that make the model more generally useful. The ionospheric model as described in NRL Report 8321 has been used for some of the examples presented in Section 20.13.

The International Reference Ionosphere (IRI) is perhaps the foremost modern example, presently available as version IRI-2001.[35–37] Other climatological models used in HF radar applications are PIM,[38,39] PRISM,[40,41] and FAIM.[42]

- Physics-based or first principles models, such as USU GAIM,[43] JPL/USC GAIM,[44] SAMI3 developed by Huba and Joyce,[45] and Khattatov's model,[46] solve the plasma dynamics and composition equations governing evolution of density, velocity, and temperature for various ion species on a global 3D grid, subject to the Earth's magnetic field and prevailing solar indices. These models required seeding with initial conditions, often a limiting consideration.

For both classes, improved accuracy of forecasting is achieved by assimilating data from ground-based sounders, total electron content (TEC) derived from GPS, UV airglow data, and in situ measurements of electron density from satellites and other sources. Often the assimilation is performed within an extended Kalman filter framework, so accuracy estimates are a byproduct. Further, site-specific applications may benefit from adaptation of the underlying model parameters and coefficients.

The complex structure and dynamics of the ionospheric medium govern HF skywave propagation primarily through the space-time variation of the free electron density distribution. A useful simplification is to regard the large-scale ionospheric structure as defining the propagation geometry throughout the illumination volume, whereas the dynamical processes impose their respective modulations on the transiting signals.

Computational Aspects and Ray-tracing. For many OTHR purposes, it suffices to employ a ray-theoretic representation of the radiowave field. Ray-tracing techniques fall into two categories: analytic and numerical. Analytic methods are fast but rely on fitting parametric models to the electron density profiles and are, hence, of limited use for operational applications where accuracy is critical. They are also limited by their inability to handle magnetoionic effects on propagation. Nevertheless, they provide closed form expressions for group range, phase path, ground range, and other parameters, and therefore, can be very useful for computationally intensive studies such as system optimization. The multi-quasi-parabolic (MQP) model of Hill[47] based on Croft's QP technique[48] is widely used, while quasi-cubic models have been proposed by Newton et al.[49]

Numerical ray-tracing codes are versatile and able to accommodate almost arbitrary ionospheric structure, at the expense of computational burden. Of the many numerical ray-tracing codes developed over the years, the implementation by Jones and Stephenson[50] based on integration of the first-order Haselgrove equations remains the most widely used. Coleman[51] has developed an alternative implementation.

Models of Ionospheric Radiowave Propagation. From the HF skywave radar perspective, interest is usually centered not on the ionosphere per se but on how it determines radiowave propagation. Models such as VOACAP[52] and ASAPS[53] generate predictions of point-to-point (circuit) parameters, including maximum and minimum usable frequency, elevation angle, group path, mode probability, path loss, and signal-to-noise ratio, for user-specified terminal characteristics. A more general capability is available with Proplab.[54]

As these models are based on their respective climatological databases, they are of no use for real-time applications such as RTIM and are inadequate for serious radar design, which should be based on measurements taken at the proposed deployment site, but they can be useful for answering certain questions, such as "Can my signal be heard at X and if so, at what SNR?"

For calculations requiring moderate accuracy, geometrical optics or virtual ray-tracing based on Martyn's Theorem can be applied to stored semi-empirical electron density profiles, or better, stored "snapshots" of the ionosphere generated by an RTIM. Alternatively, analytic ray-tracing can be performed on analytic profiles fitted to RTIM databases. The most accurate predictions come from the application of sophisticated ray-tracing routines to a database of RTIM snapshots. When a radiowave propagation model is combined with radar system parameters, target scattering characteristics, and HF noise distributions, the radar equation (Eq. 20.2) can be solved to predict the radar's performance, as treated in Section 20.13. This is the basic approach employed within RADAR C,[29,55,56] for instance. From the operational HF radar viewpoint, use of these propagation models is limited to statistical studies of radar performance, not real-time radar support applications such as coordinate registration because of the poor fidelity of the assumed electron density distributions and the shortcomings of geometric ray-tracing.

Other Models and Propagation Issues. Studies of HF radar performance at low latitudes have shown that it is often necessary to incorporate models of dynamical processes, either because they manifest themselves directly in the doppler structure of radar echoes or because they are indicators of other phenomena that do. Useful models in this category include HWM93,[57] which describes the structure of the zonal and meridional neutral winds throughout the ionosphere, and WBMOD,[58] which describes scintillation arising from small scale irregularities such as those associated with spread-F in the post-sunset ionosphere. These models find important applications to the analysis and interpretation of doppler-spread clutter.

A number of phenomena have been ignored in the preceding discussion, though their effects can be observed in some skywave radar systems. They include (i) a variety of nonlinear processes that can occur during ionospheric propagation,[59] (ii) delayed echoes,[60] focusing at the antipode, and (iii) round-the-world propagation.[61] The most significant practical exploitation of such phenomena can be found in experiments directed at ionospheric modification.

20.5 WAVEFORMS FOR HF RADAR

The factors that govern the choice of waveform in HF radar systems can be grouped into two classes. First, there are the considerations common to microwave radar, that is, range and doppler resolution as described by the ambiguity function and optimized

for target detection and estimation, realizability in hardware, susceptibility to interference, efficiency, and the electrical properties of the scatterers of interest. In addition:

- HF radar waveforms must fit within available clear channels in the HF frequency band, complying with stringent constraints on leakage into channels occupied by other users.
- They must be compatible with the fact that the radar is operating in a "waveguide," namely the volume between the Earth's surface and the ionosphere, with unique possibilities for multiple propagation paths including round-the-world propagation, significantly modifying the effective ambiguity function.
- They must be able to achieve the desired measurement capability in the presence of extremely strong ground clutter.
- They must be designed so as to minimize distortion or corruption by the ionospheric medium or, at least, enable such distortion to be estimated and mitigated by signal processing after reception.
- They must heed the constraints on peak versus average power imposed by the HF transmitting equipment and antennas.

The waveforms used in most operational HF skywave radars are variations on the periodic linear frequency-modulated continuous wave (LFM-CW) signal. Often, there is some provision for amplitude shaping, normally at the commencement and end of each sweep. The Jindalee radar was designed with the facility to apply a number of amplitude notches within the sweep, thereby enabling the radar to sweep at zero amplitude across narrow-band users in the same frequency band without causing interference. Another class of variations involves departing from a linear frequency modulation. By varying the frequency-time characteristic of the waveform, range sidelobes can be reduced and spectral leakage can be controlled. Controlling the phase discontinuity from the end of one sweep to the beginning of the next provides another dimension in which the waveform properties can be optimized. Further generalization of the FM-CW waveform is possible by relaxing the condition that the waveform be periodic. This is a powerful tool for controlling range-ambiguous echoes, which can be shifted about in the range-doppler plane to uncover previously obscured target echoes. And perhaps most importantly, in the congested HF spectrum where clear channels of adequate bandwidth to achieve the desired resolution may be scarce, FM-CW waveforms defined over two or more separate subbands are readily synthesized.

Most early HF skywave radars employed pulse waveforms, in part because the technology of the day did not support FM-CW waveforms with the required level of spectral purity for this demanding application but also because pulse waveforms enjoy some undeniable advantages. First, they can be employed from a single transmit-receive site, avoiding the cost and complexity of acquiring suitable land, duplicating many facilities and synchronizing two widely separated sites. Second, the ability to gate the echoes in time means that the only clutter power that impacts on the range footprint spanned by a pulse is clutter originating in that footprint. This relaxes the waveform generator dynamic range requirements somewhat, especially when phenomena such as auroral clutter may cause problems, though to achieve the same probability of detection, peak power must increase to maintain equivalent average power. Third, as a consequence of reduced dynamic range requirements and assuming for the moment that strict spectral emission controls are not an issue, more efficient amplifiers can be used, as discussed in the following section. Fourth, pulse waveforms may be less susceptible to some forms of jamming.

But there are disadvantages. First, emission controls are almost invariably a serious matter when it comes to obtaining a license to radiate. Second, there are radar applications beyond basic target detection where extremely high spectral purity is essential, as with detection of small ships at low speeds. Third, the antenna design must be able to handle higher field strengths without arcing and sparking, which introduces noise. Fourth, unlike the FM-CW case, it is not generally feasible to synthesize suitable pulse waveforms from separate subbands of the HF spectrum when wide clear channels are not available. Fifth, there are fewer options for radiating multiple waveforms simultaneously from the same transmitting facility. And sixth, for high power HF radars, the additional power density associated with pulse waveforms in the ionosphere may, in principle, cause self-modulation from nonlinear effects.

20.6 THE TRANSMITTING SYSTEM

Transmitters. Most of the radar designs and missions require transmitter average power levels between 10 kW and 1 MW. Antennas are generally arrays of radiating elements, and the common practice with HF radar is to drive each element with a separate amplifier. This approach permits beam steering at a low power level in the amplifier chain. The active element in each final transmitter stage can be either a traditional vacuum tube[62] or a solid-state device.[63,64] Most operational HF radars employ solid-state amplifiers based on a hierarchy of modules, starting with elemental amplifiers of perhaps 500 W and combining these progressively via passive networks until the final output power is attained. Relative phase shifts or time delays are inserted in the amplifier chain, driving each antenna element to steer the resultant beam. This architecture enhances reliability and provides graceful degradation in the event of module failure.

Solid-state HF radar transmitters operate at power efficiencies lower than those based on vacuum tube amplifiers. Vacuum tube amplifiers are also more robust and have been used successfully in a number of HF skywave radars including the AN/FPS-118. The adoption of solid-state amplifiers in radars such as ROTHR and Jindalee/JORN is driven by the need to accommodate instantaneous frequency switching over wide bandwidths while maintaining high linearity and spectral purity. These radars routinely interleave different surveillance tasks with widely separated carrier frequencies—8 and 24 MHz, for example—switching as often as every one or two seconds while conforming to strict spectral emission standards. Such instantaneous frequency changes would place unachievable switching demands on the high-level vacuum tube radio frequency circuits. Meeting power control and amplitude-shaping of waveform requirements dictates linear operation of amplifiers.

Apart from the requirement to meet emission guidelines laid down by national and international spectrum management authorities, high spectral purity is essential because skywave radar uses doppler processing to separate the targets from the clutter, and hence, the clutter returned on the phase and amplitude noise sidebands radiated by the transmitter must be kept below the echo power of desired targets. This can impose a stringent condition on the emitted signal-to-noise ratio of the transmitter, and hence, on the signal-to-noise ratio of the waveform generator. For example, noise spectral density at 10 Hz from a carrier may need to be as low as −100 dBc in order to detect some targets of interest. For designs employing an amplifier for each

antenna element, the radiated phase noise will generally add noncoherently and thus be suppressed by ~15 dB relative to beamformed noise power for a 32-element array. But that is not the end of the matter—transmitter phase noise will be reflected by the distant Earth surface and integrated across the receiver passband, raising the phase noise contributions to the noise floor by a factor that, for an FM-CW waveform, is roughly equal to the ratio of the waveform bandwidth to the waveform repetition frequency. The lower-level stages of signal amplification can generally be designed to add essentially zero noise, but mechanical vibration in the high-power amplifiers can add appreciable amounts so care must be exercised in the air or liquid coolant flow system design.

If the radar is to perform wide-area surveillance, frequent frequency changes are required in order to cover the various range extents. In addition, relative phase or time-delay changes are required in each amplifier chain to accomplish azimuthal steering. A broad-bandwidth performance and a tolerance to a variable voltage standing-wave ratio load are, therefore, essential features in an HF radar transmitter. Typically, one might specify VSWR < 2 at full power over an operating range of 5–30 MHz, say, with an ability to tolerate higher VSWRs at fractional power outputs. Since the antenna elements will be wideband, harmonic filters may be required. For example, one transmitter and harmonic filter combination might have a 5 to 9 MHz passband and a stopband for 10 MHz and higher frequencies; a second combination might pass up to 17 MHz and reject 18 MHz and higher, and the design would continue in this manner to the highest frequency of operation. Some skywave radar designs call for up to six bands. A related issue is the occurrence of mutual coupling between antenna elements in the transmit array.[65] Energy coupled back into an amplifier from its neighbors can reach levels that result in intermodulation distortion, as well as causing load resonances that stress the amplifier chain.

Antennas. The choice of antenna configuration is intimately linked to the radar mission, generally defined in terms of target types, radar coverage, and coverage rate. The Naval Research Laboratory magnetic-drum recording equipment (MADRE) radar[2] employed a single antenna, duplexed and used for both transmit and receive. This 100-m-wide by 40-m-high aperture provided sufficient gain and angular resolution for aircraft tracking in the upper part of the HF band. The experimental French OTH radar Nostradamus[11–13] likewise employs a single antenna array, configured as three horizontal arms of length 384 m radiating from a central control center, though only a subset of elements are used to transmit, whereas all of the elements are used for reception. Such truly monostatic designs have the special advantage that the outbound propagation path to a target is almost identical to the in-bound path. Monostatic radars with separate transmit and receive antennas experience decorrelation between the paths as the separation increases and different parts of the ionosphere become involved. Either form of monostatic radar avoids the costs of multiple sites and associated communications infrastructure, and the challenge of finding suitable sites with an appropriate geographical relationship, but they are constrained in waveform choice and/or radiated power by the need to avoid simultaneous transmission and reception, as well as being potentially susceptible to range-folded clutter. In particular, the class of FM-CW waveforms has been widely adopted, driven mainly by constraints on spectral emissions outside the nominal radar bandwidth. For these reasons, configurations employing separate transmit and receive antenna sites are employed in radars such as Jindalee, JORN, and ROTHR, usually in a quasi-monostatic arrangement where the

intersite separation is about 50–100 nautical miles, much less than the range to the target zone but sufficient to prevent self-jamming when using continuous waveforms and to separate the transmit and receive range ambiguity zones in azimuth.

Transmit radiating element choice is driven primarily by the range of frequencies to be radiated and the waveform bandwidth, but it must also take into account the range and azimuth coverage required, the associated coverage rate, and concerns about clutter, especially spread-doppler clutter. The vertical radiation pattern controls these issues. The power-handling capabilities of the antenna elements are also a consideration.

A lower bound on the transmit array aperture is set by the need to achieve adequate directivity and hence power density on the target; the sensitivity required depends on the size of the targets of interest. The upper bound is often set by the revisit requirement—in general, the radar will step over a wide arc, but it must sample each region frequently to maintain tracks on maneuvering targets, so the transmit beamwidth should not be too narrow. The need to keep VSWR to modest levels is usually addressed by having 2 to 6 arrays addressing subbands of about one octave of frequency each.

Some of these considerations are influenced by the advantages that attach to employing multiple simultaneous receive beams, so a broad but well-shaped transmit beam that can be filled by perhaps 10 to 30 narrow receive beams is a popular choice. In the limiting case, the transmit array may floodlight the entire sector of coverage, which is filled with receive beams that stare continuously. The nonuniformity of clutter sources can cause serious problems with any design that does not have control over the array pattern. Further, HF antennas seldom achieve high front-to-back ratios, so the risk of signal masking by backlobe clutter cannot be ignored. For linear arrays, offsetting the transmit and receive array boresights is a moderately effective measure that must be traded off against the concomitant reduction in main beam overlap. Linear arrays of vertically polarized log-periodic antennas, vertical planar arrays of horizontal dipoles, stacked Yagi antennas, elevated rhombic elements, linear arrays of tilted monopoles, and a two-dimensional array of biconical antennas have all been used in skywave radar transmit systems, in some cases, with backscreens to improve the otherwise mediocre front-to-back ratios.

In the elevation plane, desirable radiation angles run between 0° and 40° for common values of range and reflection height. The vertical beamwidth needs to be sufficient to illuminate the required range depth; in general, this is automatically satisfied owing to the cost and complexity of an antenna able to form a beam narrower than this in the vertical plane. For most scenarios, any sensitivity gained by directivity in elevation directly improves radar performance, since instantaneous range depth is generally limited by ionospheric effects. This is in contrast with azimuth directivity for transmitting, where an increase in directive gain is accompanied by a decrease in area coverage. For noise-limited detection, this can be compensated by a reduction in dwell time, but for clutter-limited detection there may be a penalty for coverage rate. Some radars use horizontal two-dimensional arrays with up to ~ 100 receive channels to achieve quite high vertical directivity on both transmit and receive. In the past, others, such as MADRE and some former Soviet Union skywave radars, employed vertical two-dimensional arrays, up to 143 m high and 500 m wide in the case of the Soviet radars.

At low elevation angles, the antenna pattern is strongly influenced by the electrical and magnetic properties of the ground around and in front of the array. To achieve

gain at low-angles, it is standard practice to install a ground mesh screen; this has the secondary benefit of avoiding pattern distortion due to inhomogeneities in the soil. For example, the Jindalee transmit arrays sit on ~ 80 hectares (~ 200 acres) of steel mesh, extending ~ 200 m in front of the arrays.

Notwithstanding the merits of vertical directivity, most skywave radars do not employ steerable directivity in elevation but cover all necessary radiation angles with one broad elevation beam. This choice permits the antenna to have a relatively small vertical dimension, and hence reduced cost, though demands on antenna radiation efficiency impose a lower limit.

Another issue is the choice of transmit polarization. Nearly all operational skywave radars radiate with vertical polarization, based on the ease of achieving good vertical coverage at moderate cost by means of the widely used log-periodic broadband antenna. The large curtain arrays of the former Soviet radars used horizontal dipole elements whereas the USAF AN/APS-118 used inclined dipoles to adapt to ground conditions. The potential benefits of full polarization control on transmit have been assessed and a number of experimental studies carried out, but no operational system has gone down this path.

The antennas and power amplifiers used in HF broadcast stations have much in common with HF radar, that is, to maintain a specified level of illumination over a designated area. To achieve this goal, many multiband and steerable broadcast antennas[66–68] employ large vertical apertures. Antennas used for HF radar have an additional severe constraint: the need to minimize mechanical motion due to the wind (*Aeolian vibration*) that would cause signal phase modulation that would then be imposed on the transmitted signals; this requirement is easier to meet with low-antenna-height designs. An under-exploited advantage of broad beams in elevation is the ability to illuminate an extended range depth when conditions permit, providing clutter maps outside the range band of immediate interest for target detection; these can be used to schedule subsequent surveillance tasks.

20.7 RADAR CROSS SECTION

The radar scattering properties of targets determine both their detectability and the prospects for target classification; therefore, much effort has gone into establishing precisely how to describe those properties for a given radar context. In the HF skywave radar case, the inevitability of Faraday rotation that occurs during ionospheric propagation has been used to argue that a fully polarimetric treatment is unnecessary, so it is common practice to represent the scattering behavior in terms of scalar radar cross section (RCS). Fully polarimetric formulations are relevant when modeling complex scattering processes[69,70] and for target classification studies.[71]

In general, aircraft and ships have dimensions that put them within the resonant scattering regime, though the smallest aircraft and cruise missiles will lie in the Rayleigh scattering regime for the lower half of the HF band. Here, the RCS displays limited aspect sensitivity and a strong dependence on the target's gross dimensions. For an aircraft, the span of the wings, the fuselage length, the tail and elevator span, the vertical stabilizer and rudder height, and their relative locations are the main features that influence the RCS. Target shaping on a scale size much less than a wavelength will have little effect. Accurate measurements of radar scattering at HF frequencies is challenging, but facilities for making scale model measurements are

widely available, including anechoic chambers, indoor compact ranges, and outdoor test fields.[72] Full-scale experimental measurements can be made in some circumstances by means of calibrated reference scatterers or transponders deployed in the target zone and modulated to separate their returns from the target and clutter echoes. For bodies with highly conductive surfaces, the scattering cross section can be calculated quite accurately by numerical methods, such as the method-of-moments code NEC.[73.] As a rule of thumb, the HF RCS of aircraft can usually be computed to an accuracy of about 2 or 3 dB (with respect to measured values) without resorting to highly sophisticated techniques.

When precise RCS information is not essential, rough but useful RCS estimates can be made by examining the scattering behavior of a few "canonical" shapes. Figure 20.7 is a family of plots giving RCS versus radar frequency for an oblong-shaped conducting body. The straight line marked 90° $\lambda/2$ dipole gives the RCS of a resonant, conducting half-wavelength rod, where the rod is parallel with the electric field. This geometry gives the maximum RCS for the rod. The upper scale of the abscissa gives the one-half-wavelength dimension of the frequency given on the lower scale. The curve marked 90° is the RCS of the oblong-shaped conducting body of 11 m length and 1 m thickness; again, the target long dimension is aligned with the electric field. The maximum RCS coincides with the nominal half-wavelength dimension or with the first resonance.
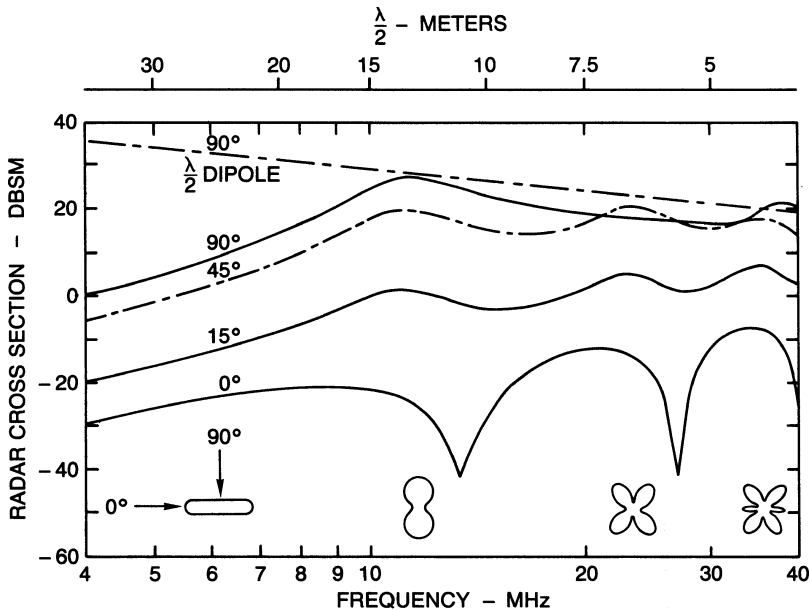
FIGURE 20.7 The frequency dependence of the RCS for an 11 m long by 1 m diameter, perfectly conducting cylinder, presented for various illumination geometries. The E vector and the 11 m dimension are in the same plane; 0° (nose-on), 45°, and 90° (broadside) curves are shown. The top (dashed) curve is for a resonant dipole at 90°. The small sketches at the first, second, and third resonances show the RCS angular pattern near these frequencies.
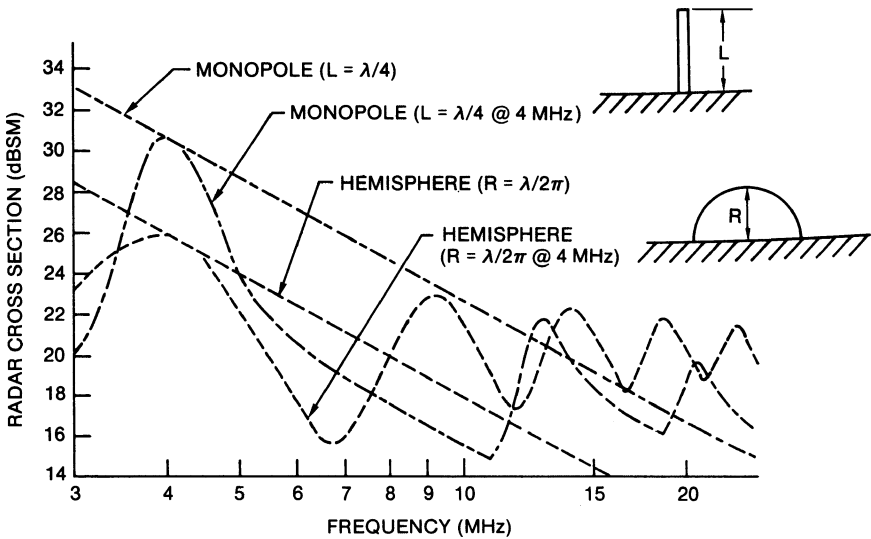
FIGURE 20.8   RCS frequency dependence of a rod (monopole) and a hemisphere on a perfectly conducting plane for vertical incident and scattered polarization

The curves marked 45, 15, and 0° give the RCS as the target is rotated to these angles in the plane that contains the electric vector. The little sketches give, at the left, the body shape, and then the RCS patterns at nominal 1/2 wavelength, 1 wavelength, and 3/2 wavelength, in order to help visualize how the RCS will change as the aspect angle is varied. For targets of other lengths with approximately the same shape factor, the response can be determined by sliding the curve along the $\lambda/2$ line and making the first resonance coincide with the line at the 1/2 wavelength point. As has been mentioned, Faraday rotation results in varying incident polarization, so over time a target will experience both favorable and mismatched polarization, with resultant fading of the scattered signal. Of course, additional fading of the scattered signal occurs due to time-varying polarization mismatch at the receiving antenna.

Figure 20.8 gives the vertical-polarization RCS of a rod and a hemisphere mounted on a perfectly conducting surface. With these canonical shapes, an estimate of RCS can be made for surface craft by matching L and R to the principle dimensions to the target. For small vessels, the mast height will be of most importance.[74] For surface targets, where the maximum RCS occurs with vertical polarization, a 12 dB skywave RCS enhancement results from the image field.

To illustrate the RCS behavior of a typical aircraft in more detail, Figure 20.9 shows the RCS of the F-18 fighter, as computed here by NEC2 applied to a wire-grid representation of the aircraft derived from a plastic kit model. The RCS shown is for monostatic (backscatter) geometry and horizontal copolar (HH) polarization. Calculations are presented for frequencies of 12, 18, and 30 MHz.

Although the fidelity of such RCS calculations of conventional platforms has been confirmed on many occasions, it is not clear that standard computational methods are applicable to the problem of estimating the RCS of aircraft targets that cannot be modeled as simple perfect electrical conductors (PEC) or to small "go-fast" boats in dynamic interaction with the sea surface.[75]
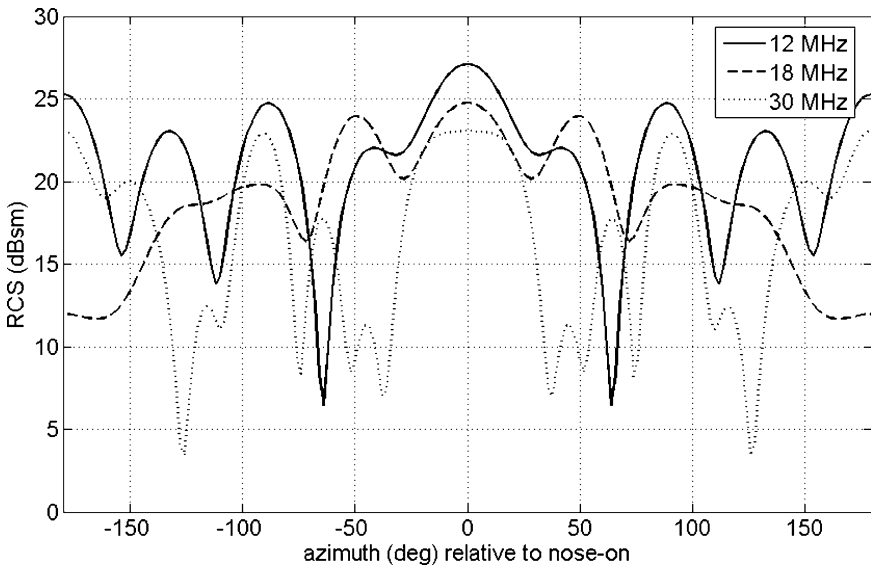
FIGURE 20.9 Monostatic RCS of the F-18 fighter aircraft at 12, 18, and 30 MHz, computed for HH polarization at a look-down angle of 5°

20.8 CLUTTER: ECHOES FROM THE ENVIRONMENT

Earth Surface Clutter.   The geometry of skywave illumination ensures that target echoes will be immersed in returns from the Earth's surface, that is, clutter. In order to detect the targets, the properties of this clutter need to be understood so that the choice of frequency, waveform, and signal processing are compatible with the need to separate target echoes from clutter, and also so that the required dynamic range of the radar can be correctly specified.

Early HF radar experiments established that the strong ground clutter observed via skywave provided an indication of the physical characteristics of the illuminated terrestrial surface. Extensive observations made at the Naval Research Laboratory viewing alternately Atlantic Ocean areas and central United States areas indicated that, averaged over a wide area, sea clutter power levels were usually about an order of magnitude higher than those from an area of similar size in the central United States. Later observers noted extremely low backscatter from ice-covered areas of Greenland. These results are consistent with predicted scattering coefficient variations based on the topography and the electrical properties of the surfaces. Subsequently, observations over the Indian Ocean with the Jindalee radar, employing carefully calibrated transponders, revealed ~25 dB variations in the ocean scattering coefficient, depending on sea state.[76]

Land Clutter.   Mapping of skywave backscatter from terrestrial (land) surfaces is of interest for two main reasons. First, a localized area of enhanced backscatter, such as a city in the central plains of the U.S. or a mountain rising from a tropical

rainforest, provides a geographical reference that can assist with the ever-present problem of coordinate registration[77] (uncertainties in the ray path traversed by the radar signals can lead to target positioning errors of over 100 km under some circumstances). Second, some regions experience strong seasonal variations in vegetation and soil moisture content, which may be reflected in measurable changes to scattering behavior. It is also important to understand the effect of the ground scattering coefficient and the topography when interpreting echoes from targets above the ground.

Sea Clutter.   In contrast with the abrupt changes in scattering behavior that occur at coastlines or over complex terrain, the magnitude of the radar echo from the open ocean, that is, the scattering coefficient $\sigma°$ tends to vary slowly with range and azimuth as a consequence of the scale lengths of typical oceanic meteorological systems and the response time of the ocean surface to varying wind stress. Moreover, much of the time, to a reasonable approximation, the echo power is proportional to the resolution cell area and can be used as an absolute amplitude reference when care is exercised. The reason for this is explained later in the discussion of radar oceanography.

Of far greater interest than the average magnitude of the sea echo is the wealth of information embedded in its doppler spectrum.[78] The waves on the sea surface introduce a complex modulation on the reflected radar signal, which is manifested in the signal's doppler spectrum. Estimation and interpretation of this modulation yields information on the time-varying sea surface geometry with major implications for ship detection as discussed below.

It transpires that a relatively simple model accounts for the observed properties of sea clutter with remarkable fidelity, provided the sea is not too rough. This model is based on two assumptions:

1. The sea surface can be represented to a good approximation as a superposition or spectrum $S(\vec{\kappa})$ of surface gravity waves satisfying the dispersion relation

$$\omega^2 = g\kappa \tanh(\kappa d) \tag{20.3}$$

where ω is the wave angular frequency, g is the acceleration due to gravity, κ is the wave number of the water wave, and d is the water depth. For deep water, this reduces to

$$\omega^2 = g\kappa \tag{20.4}$$

from which the water wave phase velocity can be written

$$v \equiv \frac{\omega}{\kappa} = \left[\frac{gL}{2\pi}\right]^{1/2} \tag{20.5}$$

where L is the wavelength of the water wave.

2. In terms of HF wavelengths, the sea surface can be regarded as only slightly rough, therefore admitting an approximate solution for the scattered field in the form of a perturbation series expansion in the parameter ka, where k is the radio wavenumber and a is a representative ocean wave amplitude. This approach, formulated by Rice[79] for the case of a static surface and extended by Barrick[80,81] to the case where the surface is evolving according to the dispersion relation (Eq. 20.4), leads to an equation for the doppler spectrum of the reflected radiowaves:

$$\sigma(\omega) = 2^6 \pi k_0^4 \sum_{m=\pm 1} S(-m(\vec{k}_{\text{scat}} - \vec{k}_{\text{inc}}))(\delta(\omega - \omega_B)$$

$$+ 2^6 \pi k_0^4 \sum_{m_1, m_2 = \pm 1} \iint \Gamma(m_1 \vec{\kappa}_1, m_2 \vec{\kappa}_2)^2 S(m_1 \vec{\kappa}_1) S(m_2 \vec{\kappa}_2) \qquad (20.6)$$

$$\delta\left(\omega - m_1 \sqrt{g \kappa_1} - m_2 \sqrt{g \kappa_2}\right) d\vec{\kappa}_1 d\vec{\kappa}_2$$

where $\vec{k}_{\text{inc}}$ and $\vec{k}_{\text{scat}}$ are the incident and scattered radio wave vectors, $k_0 = |\vec{k}_{\text{inc}}|$, ω is the doppler frequency, $S(\vec{\kappa})$ is the sea directional wave spectrum, $\delta(.)$ is the Dirac delta function, and the Bragg frequency ω_B is given by $\omega_B = \sqrt{g|\vec{k}_{\text{scat}} - \vec{k}_{\text{inc}}|}$. The kernel $\Gamma(\vec{\kappa}_1, \vec{\kappa}_2)$ is discussed below. Eq. 20.6 reveals that the Barrick-Rice solution has a simple interpretation in terms of spatial resonance or Bragg scattering. Although the disorganized-looking ocean surface is represented as the Fourier sum of an infinite number of sinusoidal wave trains, each with its characteristic wavenumber and direction, the principal "first-order" contributions to the scattered field arise from only two ocean wave trains,[82] namely those whose wave vectors satisfy the relation

$$\vec{\kappa}_\pm = \pm (\vec{k}_{\text{scat}} - \vec{k}_{\text{inc}}) \qquad (20.7)$$

For the simple case of backscatter at grazing incidence, the geometry for monostatic surface wave radar, $\vec{k}_{\text{scat}} = -\vec{k}_{\text{inc}}$, so these resonant ocean waves have a wavelength equal to one-half of the radar wavelength, with one solution corresponding to a wave directly approaching the radar and the other receding from it. The corresponding doppler shifts are those associated with the phase velocity of the resonant waves, that is

$$f_d = \pm \sqrt{\frac{g}{\pi \lambda}} = \pm \sqrt{\frac{g f}{\pi c}} \approx \pm 0.102 \sqrt{f(MHz)} \qquad (20.8)$$

where the doppler shift f_d is in Hz; g is the gravitational acceleration (9.8 ms^{-2}), f is the radar frequency, and c the velocity of light.

With this insight, the second-order term in Eq. 20.6 can be interpreted as "double-bounce" processes involving Bragg scatter from first one and then another wave train, with the twice-scattered radiowave directed toward the receiver. Of course, there are, in principle, infinitely many pairs of wave trains that can satisfy this condition, hence, the integral. And there is another complication. The individual ocean wave trains are not completely independent—they interact weakly and produce evanescent nonlinear product waves that, while not freely propagating, change the geometry of the sea surface and contribute to the scattered field at second order, also via Bragg scattering. Thus, as shown first by Barrick,[81] the second-order scattering kernel is made up of electromagnetic and hydrodynamic terms, $\Gamma = \Gamma_{\text{EM}} + \Gamma_{\text{HYD}}$. The resulting piecewise continuous second-order doppler spectrum is usually some 20–30 dB weaker than the first-order Bragg peaks but, being spread in doppler, has the potential to mask ship echoes over much more of doppler space. Figure 20.10 is an example of the numerical evaluation of Eq. 20.6 for a specific ocean wave spectrum.

Polarization dependence arises through Γ. For a highly conducting medium such as seawater, viewed at typical HF radar geometries, the copolar surface scattering
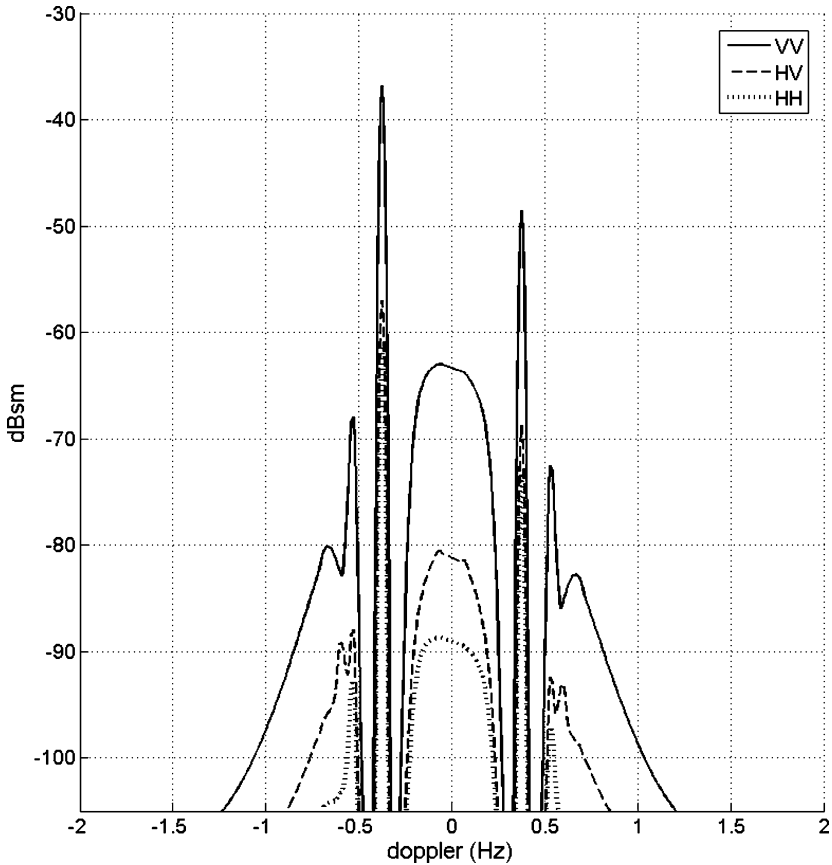
FIGURE 20.10 Computed doppler spectra of sea clutter for various polarizations; the radar frequency here is 15 MHz while the directional wave spectrum adopted is a Pierson-Moskowitz wave-number spectrum combined with a $\cos^4(\varphi/2)$ angular spreading pattern.

coefficient, or RCS per unit surface area, is much larger for vertical than for horizontal polarization, with the crosspolar scattering coefficients typically assuming intermediate values for moderate bistatic scattering geometries, $\sigma^{\circ}_{vv} \gg \sigma^{\circ}_{hv} \approx \sigma^{\circ}_{vh} > \sigma^{\circ}_{hh}$, as illustrated in Figure 20.10.

Eq. 20.6 is of fundamental importance to many HF radar applications, including ship detection, remote sensing (see following section), waveform selection, and other radar management functions. For example, Figure 20.11 shows a measured doppler spectrum and, superimposed, representative estimates of the magnitudes of the echoes that might be received from a number of different ship types for the same radar design and waveform parameters. Also shown, at left, are the speed bands within which the ship echoes would be obscured by the clutter. The ability to predict these obscured bands by means of Eq. 20.6 can be exploited for HF radar design and siting and for scheduling ship detection operations. Thus combining Eq. 20.6 with an ocean wave climatology for any region enables the statistical prediction of radar ship detection performance.[83]
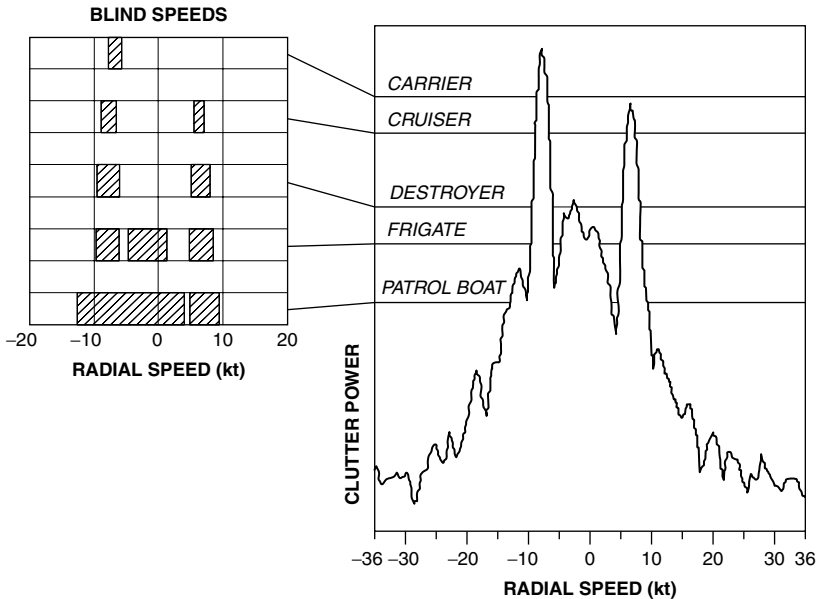
BLIND SPEEDS

FIGURE 20.11 Schematic representation of blind speed bands in which ship echoes are obscured by sea clutter

Similarly, choice of the waveform frequency and bandwidth can be guided by calculation of the clutter power spectral density as a function of these parameters for any given sea state, taking into account any information about target course, speed, and RCS.

A very important operational consideration here is the potential for an adversary to exploit the sea clutter spectrum by contriving to place his ship echo at the Bragg frequency where it would be obscured by sea clutter. The adversary can achieve this by choosing any combination of course and speed that makes the velocity component toward the radar equal to the equivalent phase velocity of the Bragg peak. The radar operator must counter this by exploiting his understanding of the detailed structure of the spectrum and its variation with radar frequency to unmask the target.

Radar Oceanography. The existence of the relation expressed in Eq. 20.6 between the sea surface representation as a directional wave spectrum $S(\vec{\kappa})$ and the doppler spectrum measured by an HF radar provides an opportunity to determine the detailed state of the sea surface by remote sensing with skywave (or surface wave) radar. In order to extract sea parameters from radar doppler spectra, and to optimize the choice of radar parameters for the radar's surveillance missions, it is helpful to understand some elementary oceanography.

The ocean waves that contribute most to the HF radar returns have wavelengths in the range of 5–100 m; these waves are excited by the surface winds. If a wind blows at a constant velocity long enough and over sufficient fetch (the distance over which the wind is blowing), a steady-state condition will be achieved where the wind provides just enough energy to the waves to balance that lost by breaking and other dissipation mechanisms. Moreover, in this state of dynamic equilibrium, energy will be transferred
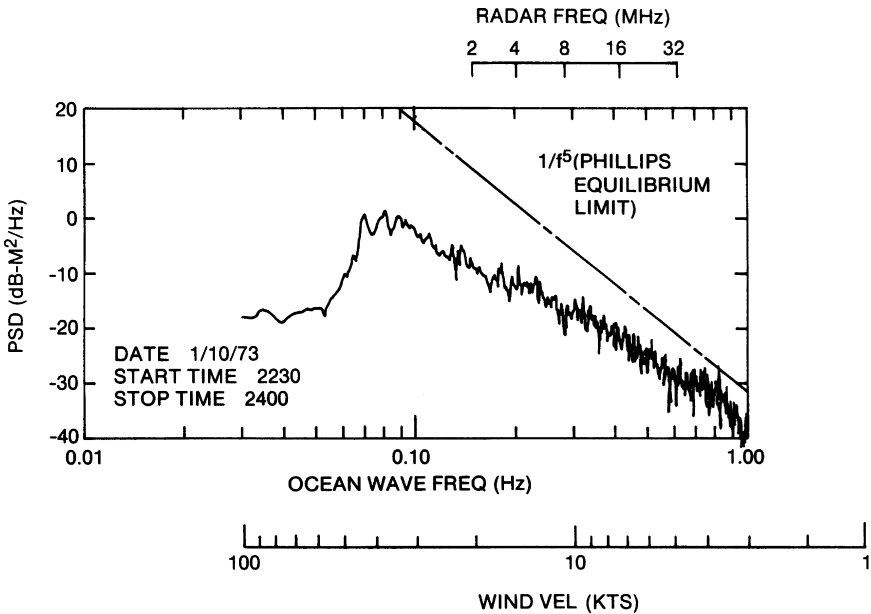
FIGURE 20.12 Nondirectional waveheight power spectral density, as measured with a wave buoy, showing power law behavior. The straight line is the original Phillips saturation asymptote, which is approached at high frequencies in this example. The scale marked "wind velocity" can be used to deduce that winds up to 40 kt have excited waves with frequencies as low as 0.08 Hz, but that either the duration or fetch, or both, have not been sufficient for full development. The scale across the top gives the radar frequency corresponding to resonant backscatter.

predominantly to waves whose velocities are fairly closely matched to the wind velocity and undergo redistribution across wavenumber space through the mechanism of nonlinear wave interactions to preserve the equilibrium spectral form.

There are a number of models that have been proposed to describe the equilibrium spectral form, and indeed, models that attempt the more ambitious task of modeling nonequilibrium spectra. Most of these models are based on experimental measurements, illustrated here by Figure 20.12, which shows an example of the frequency spectrum derived from wave buoy measurements. A common feature of such wave spectra is that waves of a given wavelength tend to reach a limiting spectral density, beyond which the processes of dissipation and nonlinear transfer of energy to other wavenumbers prevents further growth. This condition—known as saturation, or being fully developed—is reached at quite modest wind speeds for those waves responsible for first-order scatter at HF, that is 5–10 knots.

Of the various nondirectional ocean wave models reported in the literature, that of Pierson and Moskowitz has been most widely used by the radar community. They derived the following relation for a fully developed nondirectional spectrum based upon empirical data[84]:

$$F(\kappa) = \frac{\beta_e}{2\pi\kappa^4} \exp\left[-\nu\left(\frac{\kappa_c}{\kappa}\right)^2\right] \tag{20.9}$$

or equivalently, in terms of wave frequency,

$$\tilde{F}(\omega) = \frac{\beta_e g^2}{\omega^5} \exp\left[-v\left(\frac{g}{\omega u}\right)^4\right] \tag{20.10}$$

where

u = wind speed
κ_c = g/u^2
v = 0.74 and β_e = 0.0081

The exponential term approximates the decay in the spectrum for wave speeds above the wind maximum velocity. Models that take account of the consequences of finite fetch and finite duration of the wind stress include the JONSWAP spectrum[85] and the model of Elfouhaily et al.[86]; such effects can lead to substantial changes in the HF doppler spectrum and hence target detectability, so these models should be used when applicable.

The decrease of wave spectral density with wavenumber is observed to lie close to a κ^{-4} power law, as adopted by most models, and by a natural coincidence, this is balanced by the k_0^4 factor in the first-order scattering coefficient in Eq. 20.6, so the resulting σ^0 is roughly independent of frequency over the range of frequencies for which the power law behavior is observed. An important consequence is that with such a reference, propagation path losses may be estimated.

To test this idea, the magnitude and variability of $\sigma_{vv}°$ was examined with the San Clemente Island HF surface wave radar.[78] This radar facility had several valuable and unique features: a transmission path out over the open sea, multiple-frequency operation within a repetition period, calibrated antennas, known transmitter power, and ground truth in the form of ocean waveheight recordings. When looking into an approximately 20 knot wind, values of $\sigma_{vv}°$ were found to be constant within a few decibels for operating frequencies where the ocean wave spectrum was approximately fully developed; these observations provided a confirmation of Barrick's first-order theory.[80] By using the antenna gain conventions stated earlier and assuming a semi-isotropic sea directional spectrum, the value of $\sigma_{vv}°$ was calculated as –29 dB; the measured values were grouped between –7 and +3 dB of this value over a 5 to 20 MHz frequency span. This experiment provided the first direct measurements of the sea surface scattering coefficient.

Of course, when the Bragg resonant waves are not fully developed, the scattering coefficient will be proportionately less, as shown in Figure 20.13, compiled from data sets recorded looking upwind or downwind with the Jindalee radar.[76] Occasions when the wind speed was insufficient to arouse the Bragg resonant waves to saturation levels yielded scattering coefficient values up to 20 dB below the peak values.

Low scattering coefficient values can also arise because the angular spectrum of the wave system is not being sampled along a direction that presents the maximum amplitude component at the Bragg resonant wavenumber. The directional wave spectrum can be written as

$$S(\vec{k}) \equiv S(k,\phi) = F(k).G(\phi,k) \tag{20.11}$$

where $F(k)$ is the nondirectional spectrum,

$$F(k) = \int_0^{2\pi} S(k,\phi)d\phi$$
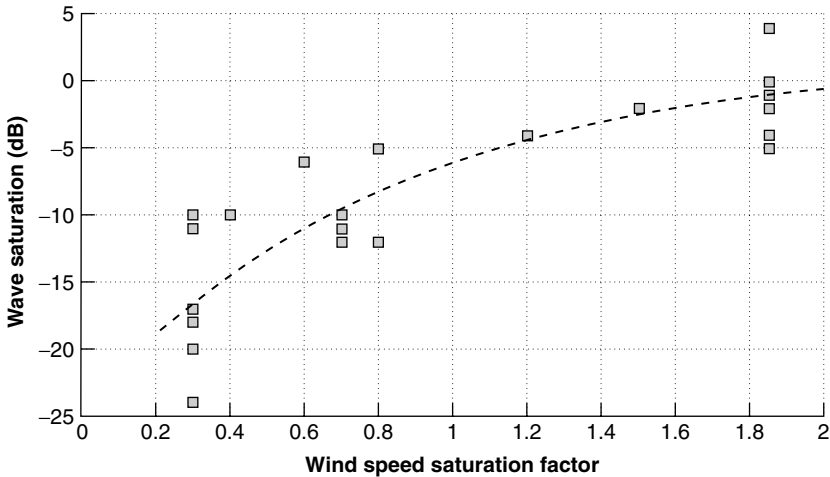
FIGURE 20.13 Calibrated measurements of the ratio of the measured scattering coefficient to the saturated sea scattering coefficient, plotted as a function of the ratio of wind speed to the phase speed of the Bragg-resonant waves for upwind/downwind observations

and $G(\phi,k)$ is the normalized angular spreading function that describes how the wave energy is distributed in azimuth,

$$\int_0^{2\pi} G(\phi,k)\,d\phi = 1$$

The non-zero wave spectrum is not confined to directions having a component parallel to the wind direction $\phi = 0$, i.e., $G(\phi,k)$ for $\frac{\pi}{2} \le \phi \le \frac{3\pi}{2}$, nor is it semi-isotropic, $G(\phi,k) = \frac{1}{\pi}$ for $\frac{-\pi}{2} \le \phi \le \frac{\pi}{2}$. In general, the angular spectrum is non-zero through 360°, with the spreading function depending on many variables, including the recent surface wind history. HF radar has sufficient sensitivity to measure the relative amplitude of the waves running against the wind, even though they may have a power spectral density (and hence an RCS) several orders of magnitude below those running with the wind. These upwind-propagating ocean waves are caused predominantly by third-order nonlinear wave-wave interactions, reflection processes, wave-current interactions, and propagation from neighboring regions with different wind stress. They are very important for remote sensing and impact strongly on target detection because the second-order scattering processes are heavily dependent on $G(\phi,k)$. They also serve as a sensitive indicator of backscatter coefficient estimation since, taking account of only the first-order scattered field,

$$\sigma^0 \propto [G(\phi-\phi_W,k) + G(\phi-\phi_W+\pi)]$$

where ϕ_W is the wind direction. To quantify this, if the wave angular spectrum model of Long and Trizna[87] is used, the maximum value of σ° for a saturated sea is –27 dB in the upwind or downwind direction (longitudinal sea) and only –39 dB in the crosswind direction (transverse sea). Figure 20.14 shows the scattering coefficient for this and some simple parametric angular spreading functions versus angle with respect to wind direction, as computed from the first-order contributions.

Peak spectral backscatter coefficient
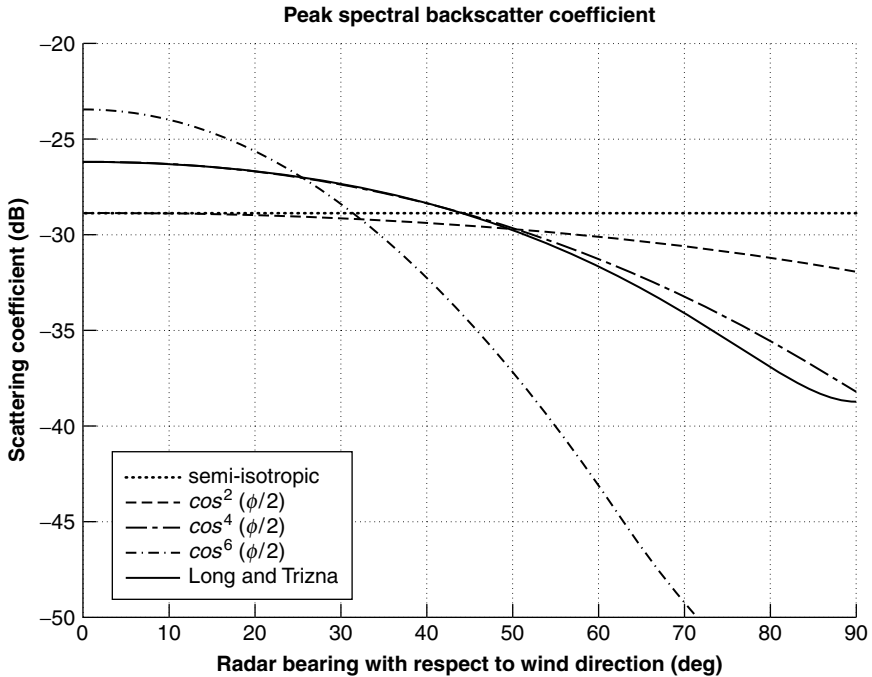
FIGURE 20.14 Variation of the peak backscatter coefficient as a function of wind direction relative to the radar look direction for various spreading functions, assuming a sea fully developed at the Bragg-resonant wave frequency

In summary, the sea echo power in a resolution cell (1) is generally the largest echo signal; (2) generally exists in the open ocean even in relative calm; (3) varies as the square of resonant waveheight, which is frequently saturated at the higher frequencies; and (4) varies with direction, being greatest for seas running toward or away from the radar. The doppler spectrum of the echo has sharp variations that require careful processing to preserve. The receiver and processor must be able to handle both the high-level signal due to this large RCS and those much smaller signals due to targets, especially when the latter are adjacent to the strongest clutter components. An HF radar must be designed to accommodate such clutter levels; even though, they will not exist all the time, or at any one time, over all areas, especially at the lower operating frequencies.

Estimation of Sea State, Wave Spectra, and Surface Winds. Techniques for extracting ocean wave field information from measured doppler spectra have been reported by numerous authors, working in almost all cases from the Barrick solution for the scattered field and dealing almost exclusively with HF surface wave radar data, uncorrupted by ionospheric propagation. Inversion of the relation in Eq. 20.6 to obtain an estimate of $S(\vec{\kappa})$ is mathematically nontrivial, requiring some additional assumptions to obtain a unique, stable solution. Some of these methods address the problem of full directional wave spectrum estimation,[88–90] whereas others propose estimators for integrated measures of sea roughness such as significant waveheight.[91]

Ocean currents can be determined when a zero doppler reference (such as an island) is in the radar footprint.[92] The NOAA Wavewatch website[93] provides access to archived maps of significant waveheight, dominant wave period, and other parameters; such information is extremely helpful when designing a radar for remote sensing applications.

In addition to providing information about the sea surface, HF radar can be used to infer surface wind speed and direction.[87,94] Wind direction is commonly estimated by taking the ratio of the first-order resonant Bragg peaks and employing an empirical relationship between this ratio and the wind direction relative to the radar look axis, as pioneered by Long and Trizna.[87] By scanning over a radar's coverage area, a map of inferred wind direction can be constructed; surface-wind direction maps are a routine byproduct of the Jindalee radar.[76]

While waveheight and wave spectrum estimates can, in principle, be extracted from higher-order features of skywave radar sea-echo spectra, a major difficulty arises due to the myriad forms of contamination and distortion introduced by the ionosphere. This has led to the development of numerous techniques for estimating and removing the various forms of signal corruption.[95–97] As an alternative, Trizna[98] and Pilon and Headrick[99] have reported a method for estimating σ° from simple measurements made directly on the corrupted radar echo spectrum. While this approach may be relatively insensitive to some forms of corruption, it is not applicable to seas far from equilibrium.

All the methods for estimating sea state or scattering coefficients require long coherent integration times, usually combined with noncoherent averaging of a number of CITs in order to achieve a distinct and stable spectrum. This type of radar operation will frequently be incompatible with other radar missions. But because the sea echo is generally a very large signal, it may be obtained with an adjunct oblique sounder operating in an appropriate radar mode.

Scattering from Meteor Trails and Other Irregularities in the Ionosphere.   Clutter from ionospheric irregularities such as those mentioned in Section 20.4 can severely limit radar performance. Unlike the terrestrial or ocean environments where velocities of natural scatterers tend to be low, the ionosphere is home to phenomena with apparent speeds of 10^2–10^3 ms^{-1} and more, obscuring much of the relevant doppler domain where manmade targets might be found. Many of these scatterers have a transient existence, much less than the coherent integration time, so conventional signal processing causes their echoes to appear spread in doppler, as well as doppler shifted. The generic term *spread-doppler clutter* is used to cover all these phenomena where the scatterers responsible for the clutter do not have a well-defined doppler shift. The same term is used to describe the entirely different mechanism where clutter smearing in doppler occurs as a consequence of rapid variations in the propagation path rather than in the motion of the scatterer.

Meteors and their trails are the most ubiquitous source of transient echoes.[100–103] They display a reasonably well-defined diurnal and geographical distribution specific to any given radar site, but they can cause problems over a wide range extent because they can be illuminated by a variety of propagation modes,[19] as shown schematically in Figure 20.15. Normal incidence as shown yields the largest echo, but oblique incidence echoes and scattering from the meteor "head" are also observed. Figure 20.16 compares a simple predictive model with measurements, confirming that the observed behavior is understood and thus can be taken into account in radar design and operations.
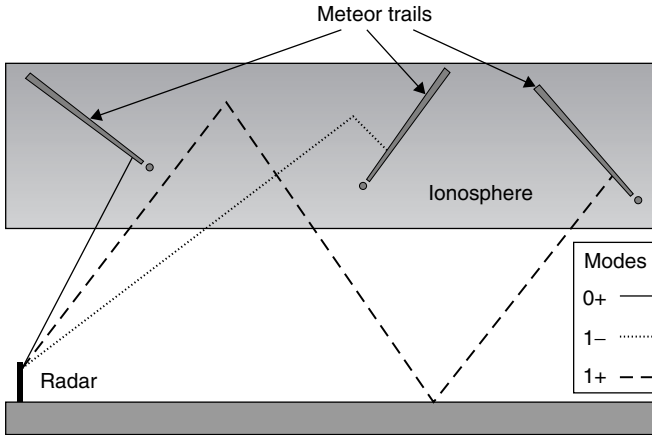
FIGURE 20.15 Meteor trail specular scattering geometry for several propagation modes

Meteors are usually classified as *sporadic*, occurring more or less randomly as the Earth moves around the sun, and *showers*, such as the Leonids and the Eta Aquarids, which occur on predictable dates where their orbits intersect the Earth's orbit.
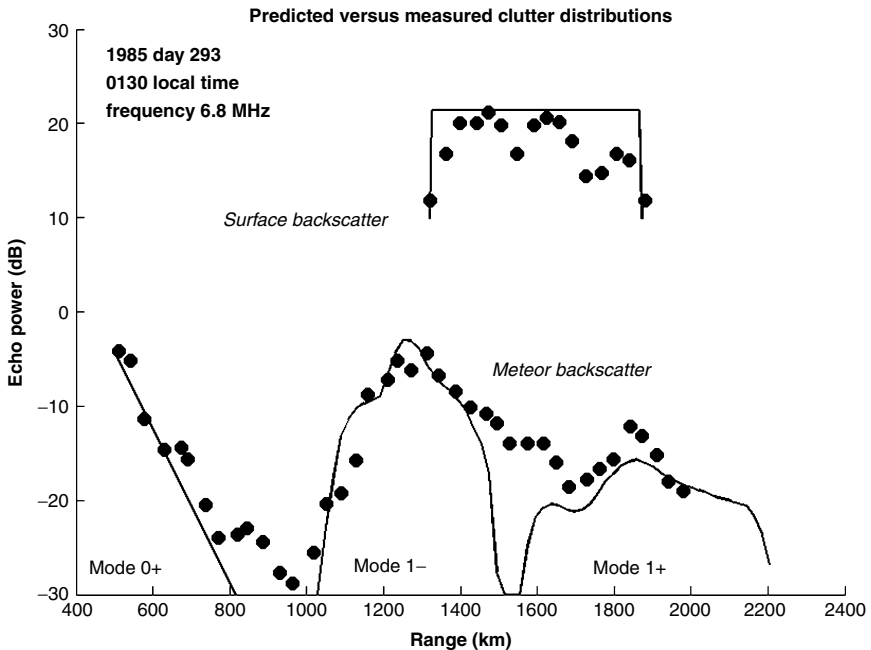
FIGURE 20.16 Predicted range dependence of meteor echo strength compared with measurements; ground clutter returns are also shown. The distribution of meteor radiants determines this variation.

On these occasions, the flux of meteors can be so high that they can cause serious obscuration of target echoes. As radars become more sensitive, they register smaller and smaller meteors, which are far more abundant, so at times, the flux of countless small meteor trails sets the effective detection threshold.

Meteor echo suppression can be attempted in the spatial domain if the receiving array has vertical directivity, but for most radars, the only option is rejection by signal processing, exploiting the transient nature of the echoes to detect and censor them in the time domain.

Echoes from the aurorae similarly involve transient scattering processes that appear in the radar data as highly doppler-spread echoes with the potential to obscure targets. Scattering from the auroral region has been studied extensively using the SuperDARN HF radar network initiated by Greenwald,[17] and an auroral echo-scattering model has been developed by Elkins[104]; this can be used to predict target obscuration when the transmission path is through the auroral region. Provided the radar is well removed from the auroral zone, the waveform can often be chosen so as to manipulate the clutter echoes within range-doppler space, unmasking targets hitherto obscured. Often several waveforms with different repetition frequencies are interleaved to achieve this. For radars close to the auroral zone, the options are generally more limited.

Ionospheric irregularities that scatter back to the radar receiver occur much more often at night than by day at any latitude. Sensible siting of the radar, ensuring good front-to-back ratios on the antennas, employing vertical nulling if available, and using adaptive signal processing techniques (or at least maintaining low receive array sidelobes) are all effective tools for mitigating auroral, meteor, and other ionospheric clutter.

20.9   NOISE, INTERFERENCE, AND SPECTRUM OCCUPANCY

In the HF band, the average noise power spectral density at mid-band, near 15 MHz, say, may exceed –150 dBW/Hz and will generally exceed –175 dBW/Hz, compared with typical receiver internal noise spectral densities of perhaps –195 dBW/Hz. Thus, unlike the microwave radar case, external noise is almost always dominant. This has fundamental implications for receiving system design and signal processing. Another critical issue is the observed systematic variation of the external noise level, which has a direct impact on radar performance.

The major source of quasi-continuum background noise at the lower frequencies is lightning discharges ionospherically propagated from all over the world *(sferics)*. At the high-end of the band, extraterrestrial or galactic noise may be greater than that due to sferics. Receive sites in an area of extensive electrical equipment use can find anthropogenic noise dominant. But most importantly, the HF band is densely occupied by other users, especially powerful HF broadcasters relying on the prevailing frequency window for satisfactory propagation. Even out-of-band signal levels are a consideration in receiver front-end design, where it is common to have bandwidths much wider than that of the radar signal. There are a large number of broadcast stations that have 500-kW transmitters and antennas with more than 20-dB gain. Measurements made on the middle Atlantic coast of the United States show HF broadcast-band signals with strengths of 5 to 10 mV/m. These ambient levels must be accommodated in receiver design because a wideband front end is desirable for rapid and frequent frequency changes.

The practice in allocations for HF radar operation is to permit use of broad bands of the spectrum with a requirement to cause no discernible interference to an existing service and to provide a lockout feature for channels that need protection. Thus, an integral part of an HF radar is a channel occupancy analyzer that provides a real-time description of spectrum availability, as illustrated in Figures 20.17 and 20.18.
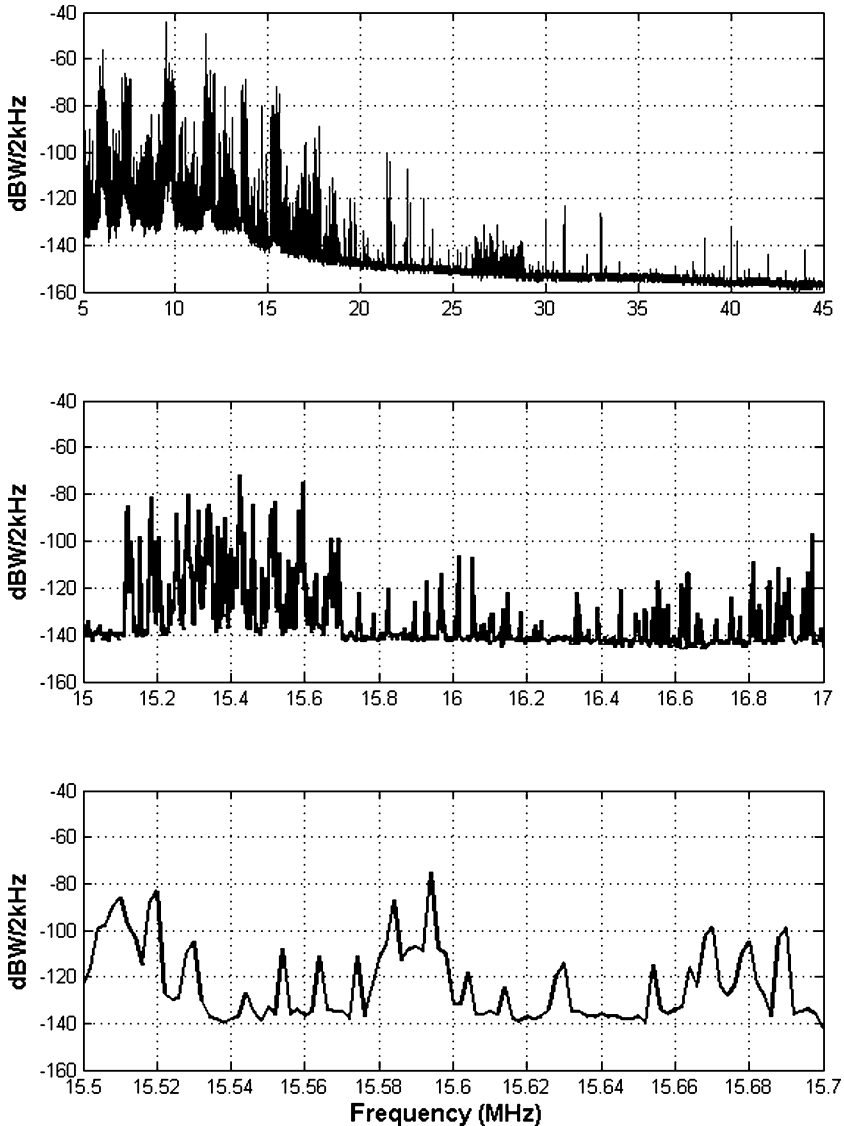
FIGURE 20.17   A snapshot of the HF spectrum at noon in summer and at a low sunspot number, zooming in progressively to show a section of the spectrum where a 20 kHz clear channel is evident, centered on 15.640 MHz. The data was recorded at latitude 23.6 S, longitude 133.1 E.

Almost without exception, HF radars have operated on this principle of noninterference, making do with "clear" channels between other users.

Patterns in Spectrum Occupancy.   When the HF band is scanned with a spectrum analyzer, it can be seen that the gross features of occupancy at any particular hour are remarkably stationary over the days of a season. This is due to broadcast stations, fixed-service point-to-point transmitters, and many other spectrum users having regular schedules, as is evident from Figure 20.18, which plots the power spectral density at 2kHz resolution for high and low solar activity, summer and winter, day and night.
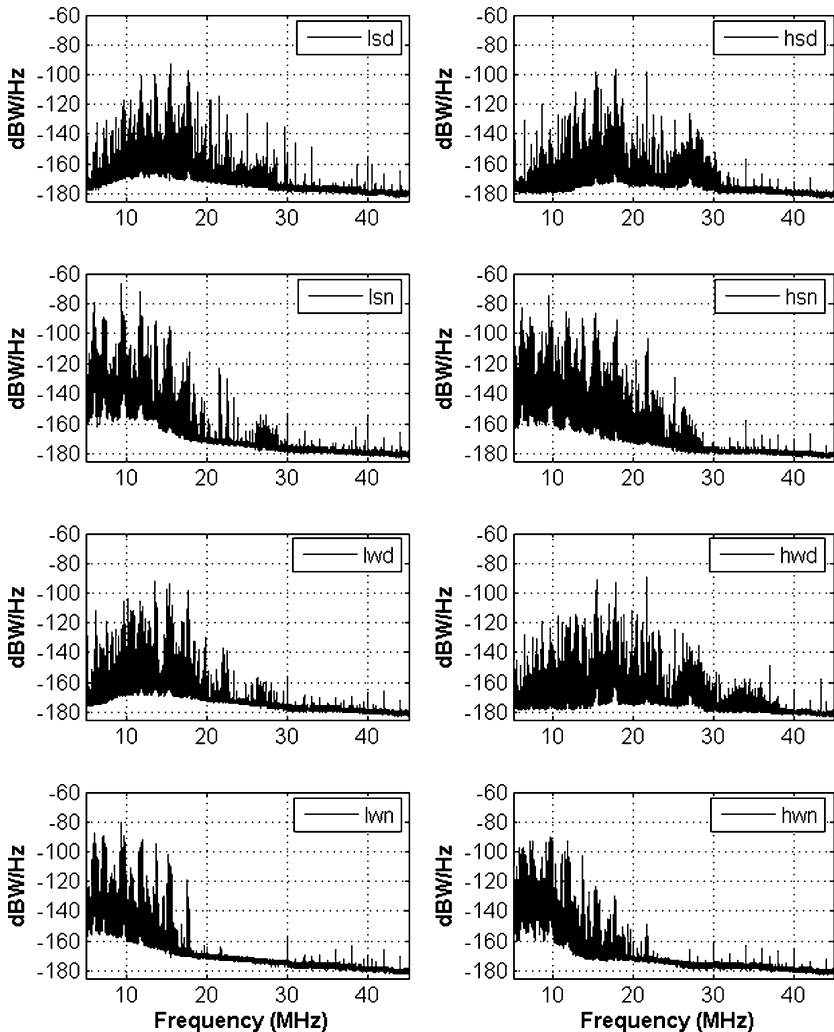
FIGURE 20.18   HF activity over the 5–45 MHz for low and high sunspot numbers (l, h), summer and winter (s, w), and day and night (d, n), as measured at latitude 23.6 S, longitude 133.1 E. The data is taken from Julian days 180 and 360 of 2000 and 2005.

As remarked earlier, the maximum frequency that will reflect energy back to the Earth during the day may be more than twice that at night; therefore, the occupancy tends to be denser at night than during the day—a problem compounded by the lower absorption and, hence, reception of more distant signals.

Looked at over longer timescales, various patterns and trends emerge. Most obviously, the 11-year solar cycle forces changes to spectrum usage and the density of users, with a resultant impact on HF radar channel selection. Another trend that has become apparent in recent years is the gradual reduction in HF users as services move to satellite communications, microwave links, fiber optics, and other media. Nevertheless, the increased number of HF radars has led to a new challenge: inter-radar interference and the need for frequency arbitration.

Noise Models. The widely used reference on noise is the International Radio Consultative Committee (CCIR) Report 322.[105] This report is based upon measurements made at 16 locations throughout the world. The measurement and data analysis were performed to exclude individual collection site local thunderstorm contributions. Spaulding and Washburn[106] added data from the former U.S.S.R. for two revised CCIR reports.[105] Noise-level medians as a function of frequency are given in the form of worldwide maps by season and 4-h time blocks. Lucas and Harper[107] have provided a numerical representation of CCIR Report 322-1, which is useful for computer computations, and this has been revised by adding the work of Spaulding and Washburn. The maps of median values are accompanied by decile values to indicate distributions over days of the season. (CCIR Report 322-3 (1988) has a significant discrepancy, as pointed out by Sailors,[108] so it should be used with caution.) These noise maps provide the level that an omnidirectional antenna would receive. Even though assuming isotropic CCIR noise has limitations, it does provide a reference level for initial radar design. A number of operational and experimental HF systems have accumulated their own noise databases and compared them with CCIR model data; the report of Northey and Whitham gives a detailed analysis.[109]

An HF radar is generally designed to take advantage of what the environment permits; that is, the receiver noise figure should be good enough to make environmental noise the limitation.

An example of the CCIR Report 322 data will now be discussed. Figure 20.19 was drawn from Lucas and Harper.[107] Noise power in a 1-Hz band relative to 1 W (dBW) is given as a function of frequency for three different sources of noise: galactic, atmospheric, and anthropogenic. The practice in use is to select the largest. This is a winter daytime example at a United States east coast location. The three straight lines are estimates of anthropogenic noise for three different types of sites. The shape of the anthropogenic curves is described by the equations

$$N_o = -136 - 12.6 \ln (f/3) \quad \text{residential}$$
$$N_o = -148 - 12.6 \ln (f/3) \quad \text{rural}$$
$$N_o = -164 - 12.6 \ln (f/3) \quad \text{remote} \qquad (20.12)$$

where the frequency f is in megahertz and ln indicates the natural logarithm.

These frequency trends approximate many measurements of human-made noise but ideally the curve would be based on measurements at the particular radar site. The galactic-noise curve should be selected when it is the largest and when there is a path through the ionosphere; the path will not exist for the lower operating frequencies in the daytime. The atmospheric noise rises from low frequencies to about 12 MHz and
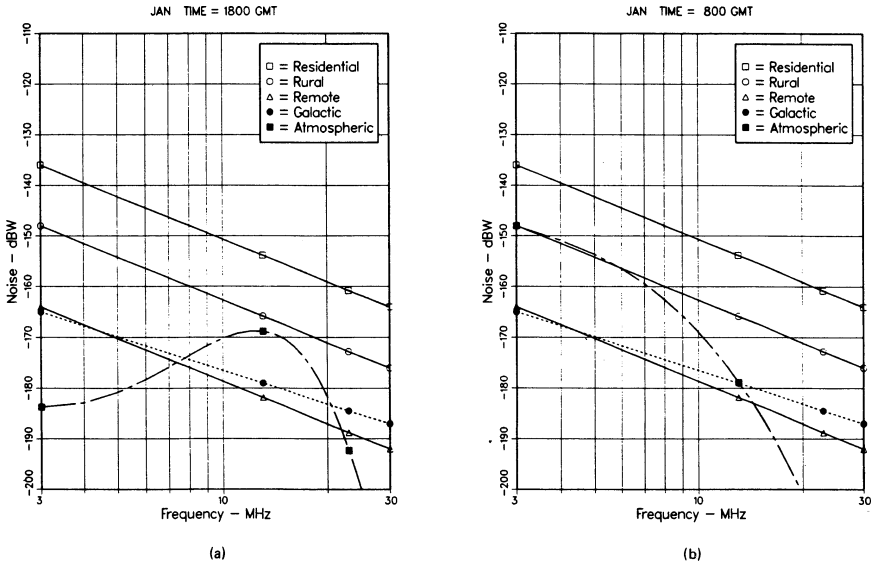
FIGURE 20.19   Noise power per hertz is given for 38.65' north latitude and 76.53' west longitude in winter: (*a*) 1800 UTC is given as a daytime example and (*b*) 0800 UTC is given as a nighttime example.

then rapidly falls. Figure 20.19*b* is for nighttime. All the curves are the same as in Figure 20.19*a* except for atmospheric noise. At 10 MHz, the night and day levels are the same; below 10 MHz, the noise decreases with decreasing frequency in daytime and increases at night. Above 10 MHz, daytime levels are greater than those at night. These effects can be partially explained by the very lossy long-range paths in day that attenuate the long-range noise at the lower frequencies and by there being few or no skywave paths to noise terrestrial sources at the higher frequencies at night. In general, nighttime noise will be greater than daytime noise for skywave illumination of a selected range. This is evident in Figure 20.20, recorded at time zone UT + 9½. The general trends of atmospheric noise in other seasons are similar to those in winter. However, there can be large differences in levels at other locations on the Earth.

For more detailed analysis and system optimization, it is no longer acceptable to treat the noise as an isotropic field. Strong azimuth- and elevation-angle dependence of the sferics field is inevitable: examination of maps produced by satellites [110] indicates that tropical rain forests and other regions of concentrated thunderstorm activity are major sources of noise, and these regions are connected with a given radar site by the constraints of skywave propagation. Coleman[111] combined the thunderstorm activity maps of Kotaki[110] with numerical ray-tracing and modeled antenna patterns to demonstrate that the directional variability of noise, coupled with the directional characteristics of different antennas, can lead to marked changes in noise outcomes and hence in optimal radar design.

Another important issue is the behavior of the external noise field as a function of time, that is, within the coherent integration interval since this impacts strongly on signal processing for interference rejection.[112] Other effects that can influence radar performance are sometimes mistaken for the *additive* noise discussed above. One of
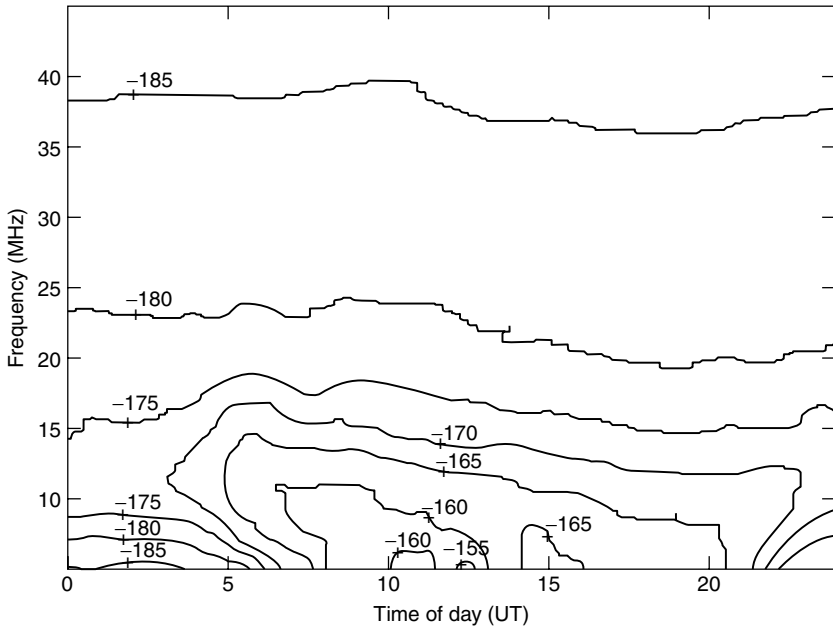
FIGURE 20.20 Diurnal variation of HF noise, measured in dBW/Hz, at latitude 23.6 S, longitude 133.1 E, 5 November 1995

these is the spread doppler clutter discussed in Section 20.8, sometimes referred to as *active* or *multiplicative noise*. The occurrence of this type of clutter is greater at night and is much more prevalent in the auroral zones and around the magnetic equator.

20.10 THE RECEIVING SYSTEM

The receiving system is defined here to embrace only the receiving antenna array and the receivers that convert the antenna outputs to discrete time series, usually at base-band. For ease of reference, the conventional signal processing stages responsible for transforming the receiver outputs into standard radar products are discussed in Section 20.11, together with more specialized techniques.

Antennas. From the reception viewpoint, it is desirable to have fine azimuthal resolution for several reasons, including (i) to improve target location accuracy and tracking performance, (ii) for detailed clutter mapping, and (iii) to reduce the clutter amplitude levels to values permitted by system dynamic range and slow-target detection requirements. As mentioned earlier, most HF skywave radars employ a broad transmit beam to illuminate a zone of interest, and then process the echoes via a number of much higher resolution simultaneous "finger" beams. It is well known that the classical resolution of an array improves linearly with aperture up to some limiting value determined by the environment. Horizontal apertures of 2–3 km and even greater

have been shown to support spatially coherent processing.[113,114] Hence, the receiving array apertures of skywave radars may range from ~ 0.3 km for systems concerned only with aircraft and ballistic missiles to more than 4 km in systems designed for ship detection and tracking. Taking 3 km as a receive aperture, conventional beamwidth at 15 MHz is ~ 0.5°, so 20 simultaneous beams span ~ 10°, which sets the required transmit aperture in this example at 120–150 m, depending on the variation in gain that can be tolerated across the set of receive beams. The most versatile beamforming techniques rely on having a receiver for each array element, but as the number of elements may approach 500, the cost of such a solution may be prohibitive. It is then advantageous to configure the array elements into subarrays, possibly overlapped or sharing elements, with one receiver per subarray. For instance, the original Jindalee radar grouped 462 elements spanning 2.766 km into 32 overlapped subarrays.[115] While this constrains the resultant beams to lie within the subarray angular response pattern, it has the advantage of reducing receiver dynamic range requirements by suppressing interference from other angular sectors.

Linear arrays provide the most economical route to high spatial resolution in azimuth, but the existence of multiple paths for signal reception, typically via the E, F1, and F2 layers, has motivated some designers to employ two-dimensional arrays, horizontally or, at greater cost, vertically deployed. The relative merits of these designs can be measured only with respect to the priorities accorded to the various missions assigned to a given radar.

The choice of receiving antenna element has traditionally been based on the precept that, at HF, the external noise almost always exceeds the internal noise by a substantial margin. On this logic, improving antenna efficiency increases the output external noise and interference amplitude at the same rate that it improves the wanted signals, thereby gaining no advantage in SNR. Selection of antenna element type, such as monopoles, dipoles, Beverage antennas, phased endfire rows of monopoles, or biconical antennas, for instance, can then be based on frequency response over the anticipated band of interest and suitability for the chosen array geometry, as well as terrain constraints such as the soil conductivity. Studies have shown that this argument is not necessarily valid when advanced adaptive spatial and temporal processing techniques are employed because interference rejection efficacy is enhanced by higher interference-to-internal noise ratios.

It has been widely argued that the inevitability of time-varying polarization transformation in the course of ionospheric propagation greatly reduces the possible utility of being able to measure the polarization state of the signals arriving at the receiving array. This is an open question at this time, though experiments aimed at assessing skywave radar polarimetry are underway.[116]

Receivers.   There are many demands on the receivers for OTH radar, including high dynamic range, linearity, wide bandwidth, and uniformity between receivers when used in multireceiver systems. For most civil aircraft and ships, target radar cross section (RCS) at HF is roughly of the same order as the microwave RCS, that is, ~10–20 dBsm for aircraft and ~30–50 dBsm for ships, but the range is 10–100 times greater, so the extra loss associated with R^{-4} is in the range 40–80 dB. Moreover, each target echo is immersed in clutter from the illuminated footprint, which may have an area of many thousands of square kilometers. Further, the HF signal environment includes (one-way) transmissions from powerful radio stations around the world, as discussed in the previous section. Imperfections in the receiver result in some of this

noise and clutter energy being superimposed on the wanted radar echoes, either additively or multiplicatively. Hence, careful attention to receiver design is imperative if the radar designer wishes to avoid self-inflicted performance limitations.[117]

Attempts to reduce contamination from external broadcast signals by inserting narrow-band filters at the receiver front-end sacrifice the high agility that is needed when the radar is changing frequency, typically by several MHz, second by second, as it jumps between tasks. There are also penalties from (i) filter switching time, (ii) settling time, (iii) distortion caused by group delay dispersion, and (iv) reduced reliability when there are hundreds of receivers. Further, each channel will need to account for the gain and phase variation for each filter, increasing the overheads on band switching. It is better to zero in on the bandwidth of interest by nonswitched filters later in the receiver, using a variable frequency local oscillator to position the desired subband(s) over the selective filters. Of course the switched LO can also suffer from imperfections, but only one local oscillator is needed, as opposed to hundreds of receivers. Whichever design path is followed, the demands on receiver linearity and spurious-free dynamic range are extreme.

There are five dominant mechanisms known to degrade HF radar receivers: the nonlinear processes of analog-to-digital conversion, out-of-band inter-modulation (IMD), cross-modulation, and in-band inter-modulation, and the pseudo-linear process of reciprocal mixing.

Analog-to-digital Conversion. Analog-to-digital conversion involves two stages—sampling and quantization—each with potential for distorting the received signal. The received signals must be sampled with sufficient precision and uniformity to preserve the inherent spectral content across the dynamic range spanned by the signal components—target echoes, clutter, and external noise—after taking account of the artifacts introduced by quantization and timing jitter, especially in multi-receiver systems.[118,119]

Out-of-band Inter-modulation. Out-of-band IMD arises from nonlinear mixing of two (or more) strong interferers such as broadcast stations, where the powerful signals enter the front end of the receiving system and generate IMD products within the radar signal bandwidth before they, the original interferers, are rejected by selective filtering.[120,121]

Cross-modulation. Cross-modulation involves nonlinear mixing of a strong interferer with the received radar echoes, transferring the interferer modulation onto the radar signal.[120,121]

In-band Inter-modulation. A single resolution cell in the radar footprint may have an area of 50–500 square kilometers, and there may be hundreds of cells in the radar footprint, so using representative values of target RCS (Figure 20.9) and surface scattering coefficient σ° (Figure 20.14), the signal-to-clutter ratio in an OTH radar receiver may be as low as –80 dB for systems employing FM-CW waveforms. Nonlinearity at any stage has the potential to mask target echoes by mixing the clutter echo with itself, generating IMD products that extend beyond the intrinsic doppler band of the clutter. Unlike the out-of-band IMD, in-band IMD can occur at any stage through the receiver, and hence even second-order products may cause problems.[122]

Reciprocal Mixing. Analog receivers of heterodyne design generally involve a number of local oscillators for signal mixing and perhaps a waveform generator used to implement a matched filter. These ancillary sources are inevitably of finite spectral purity, with a phase noise floor that may extend over a wide band of frequencies, albeit at a very low level. Any powerful interfering signals entering the first mixer stage of the receiver will combine with the phase noise floor and potentially generate products in the radar signal bandwidth.[123,124] In the case of digital receivers, sampling noise will have an equivalent effect.

Digital Receiver Technology. HF receivers can employ direct digital conversion at RF, avoiding some of the limitations of analog devices. Issues such as reciprocal mixing are still present, though in slightly modified form. Comparisons with analog receivers have demonstrated that little or no penalty is incurred with such designs if a band preselector filter is installed at the front-end. On the other hand, there are major advantages to be had, such as simultaneous reception of several radar signals on different frequencies, so a single receiver can service more than one radar transmitter.

Calibration. The conventional beamforming process in an ideal multi-channel receiving system should deliver a single output, assigned to the correct direction, for a plane wave incident on the antenna array. Inevitable variations in gain and phase arising from small antenna positioning errors, ground screen inhomogeneities, differences between preamplifiers, mutual coupling, cable mismatch, thermal and other variations of cable characteristics, and all the analog stages of the receiver result in distortion of the beam shape (and hence degraded radar resolution), elevated sidelobes (and hence vulnerability to clutter and interference), pointing errors (and hence increased tracking errors), and interferer wavefront geometry perturbations (and hence wasted degrees of freedom in adaptive beamforming).

To mitigate these effects, HF radars must employ sophisticated calibration schemes. Several approaches have been tried:

- Use of an external radiating element in the near-field in front of the array. This scheme is vulnerable to variations in the soil electrical and magnetic properties, such as those resulting from seasonal changes in soil moisture levels.

- Injection of a calibration waveform at the antennas, or at the receiver inputs behind the antenna array, by means of an independent "open loop" signal feeder network.[125] This scheme cannot calibrate the antennas and initial feeders; it applies only from the point where the signal is injected.

- Use of a distant radiating source that illuminates the array via skywave or even a discrete target echo. This scheme presumes that the arriving signal wavefronts are essentially planar or smooth after ionospheric reflection, which is not always the case.[126]

- Joint analysis of multiple discrete meteor echoes.[127,128] This scheme is appealing but relies on having enough identifiable discrete echoes. For a 32-element array it may be generally viable, but less frequently for a 500-element array.

- Receiver and plane wave rejection tests applied to injected broadband noise.[129] This approach provides useful metrics of calibration performance and relative performance, but does so only downstream from the receiver inputs, as with (ii) above.

Each of these approaches has its advantages and drawbacks in the context of conventional (Fourier) beamforming. When adaptive processing techniques are being employed, it is also important that the effective look direction matches the array steering vector or else cancellation of the wanted signal will occur.

20.11 SIGNAL PROCESSING AND TRACKING

Signal Analysis and Target Detection.   The objective of signal processing is to detect and characterize echoes from scatterers of interest, either discrete (aircraft or ships) or extended (the sea surface), and this is customarily achieved by decomposing the time series data from the receivers into the natural radar domain dimensions of group range (based on time delay), direction of arrival (beam space), and doppler frequency, hopefully separating the echoes of interest from unwanted clutter and noise. The standard tool for this decomposition is the FFT, at least in operational skywave radars, in part because it is computationally quite feasible to analyze the incoming signal into typically $\sim 10^2$ range bins, $10^1 - 10^2$ beams, and $\sim 10^2$ doppler cells, in perhaps $\sim 10^0$ seconds, using general purpose computing hardware. Thus, the FFT (or DFT for short transforms) is commonly used for the three dimensions of analysis. Alternative analysis techniques have been implemented in some systems for applications such as detection of accelerating targets,[130–132] the detection of harmonically related signals,[133] and when high doppler resolution is required but only short coherent integration times can be accommodated in the radar timeline.[134]

Some important processor design considerations emerge from an analysis of high quality HF radar data, as illustrated by the following example. Figure 20.21 shows a sequence of sea clutter doppler spectra from the AN/FPS-118 radar, presented as received power amplitude versus doppler frequency. To generate this plot, 15 power spectra from a single range bin were computed from nonoverlapping time intervals, and then grouped into blocks of five and averaged noncoherently. The waveform repetition frequency (WRF) in this case was 20 Hz, with a coherent integration time of 12.8 s, resulting in a nominal doppler filter bandwidth of 0.08 Hz. Noise (N) samples were taken from the maximum doppler bin, target samples (T) on the target peak, and Bragg line amplitudes (A) and (R) from the clutter peaks corresponding to the approaching and receding resonant ocean waves, as described in Section 20.8. N, T, A, and R are plotted in Figure 20.22a. The sub-clutter visibility (SCV), widely used in HF radar as a measure of sensitivity and defined as R/N, is 76 dB in this example. (In microwave radar, the term *sub-clutter* visibility is sensibly defined as the ratio by which the target echo power may be weaker than the clutter power and still be detected. In the HF radar literature, historically the detection threshold component has not been included, so SCV is essentially the clutter-to-noise ratio.)

For a representative effective clutter RCS of 65 dBsm per resolution cell, the target RCS can be estimated as

$$RCS = 65 - R(dB) + T(dB) = 65 - 76 + 34 = 23 \text{ dBsm}$$

and supposing that the SNR required for registering a detection is 15 dB, the minimum detectable RCS (MDRCS) in this example can be computed as

$$MDRCS = 65 - R + N + 15 = 65 - 76 + 15 = 4 \text{ dBsm}$$
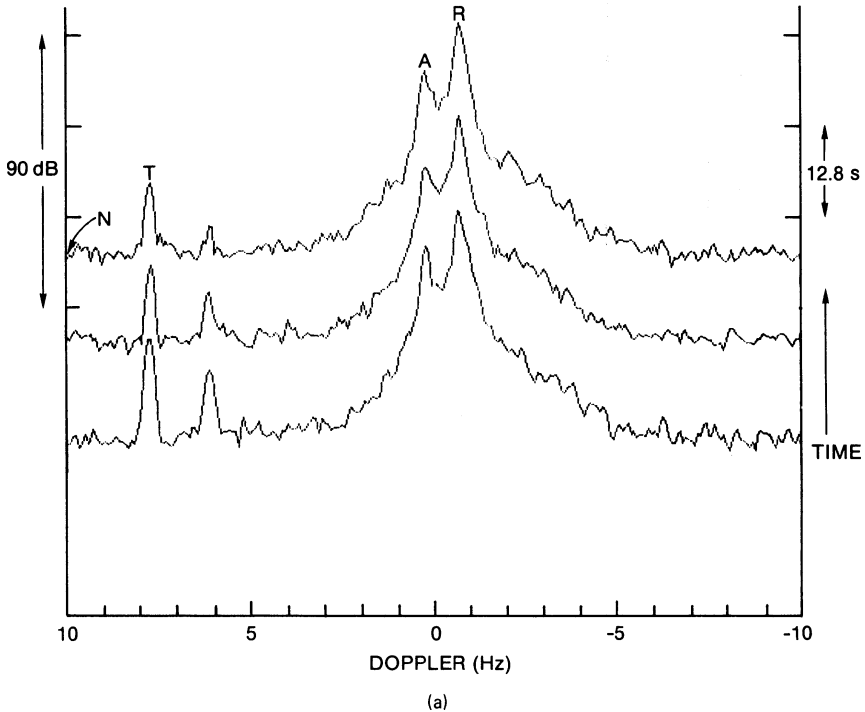
FIGURE 20.21   Noncoherently averaged power spectra from three contiguous time intervals, plotted with an offset for clarity. The target lies well outside the clutter region where the Bragg lines are clearly visible, so the signal-to-noise ratio, not the signal-to-clutter ratio, determines detectability. Note the ~10 dB variation in target echo strength due to changes in the ionosphere over 128 seconds.

This is a quite low RCS at HF, indicating that when conditions are favorable, very small targets are potentially detectable.

The experimental demonstration that, on occasion, the environment supports ~80 dB sub-clutter visibility obliges the radar designer to ensure that the receiving system and signal processing operations do not unwittingly degrade the radar performance. Some appropriate design considerations are

- An analog-to-digital (A/D) converter of at least 16-bit precision is in order for HF radars with high power-gain products, $P_{av}G_TG_R$.
- Receiving apertures, waveform bandwidths, and coherent integration times should provide enough samples and high enough sampling rates to resolve unambiguously distinct features of the clutter spectrum where such resolution impacts on target detectability or the extraction of important information.
- The window functions used to control leakage during conventional spectrum analysis must have sufficiently low sidelobes when transforms are to be applied directly to high dynamic range data.

The basic steps of range, azimuth, and doppler analysis are not the only stages of signal processing. As explained in Section 20.4, HF skywave radar signals are subject
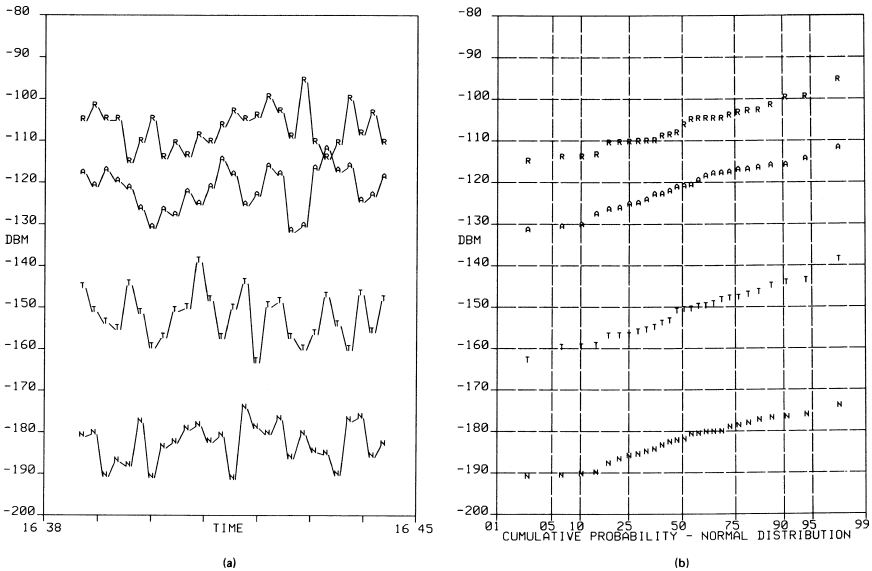
FIGURE 20.22 (*a*) Temporal fading and (*b*) distribution properties of the target, clutter peaks, and noise features in the doppler spectrum of Figure 20.21, computed from an extended data sequence

to various forms of contamination and distortion, many ionospherically induced, so methods to deal with these have long been part of the radar signal processing toolbox.[135,136] Moreover, the need to deal with these deleterious effects has become more pressing as the achievable dynamic range of receiving systems has increased, revealing a greater variety of signal distortion mechanisms. Hence, in addition to performing the basic decomposition described above, and calibrating the receiver chain for the current waveform, the signal processing stage may be tasked with a number of signal conditioning operations. Signal conditioning here refers to filtering and scaling processes aimed at removing contamination and distortion that, if left on the signal, would degrade the results of the primary processing operations, such as doppler analysis, and be more difficult to remove after that primary processing. Typically, there are (optional) processing algorithms available to remove impulsive noise originating from lightning, transient echoes from meteors, and field-aligned irregularities in the ionosphere, strong directional interference, and clutter echoes from beyond the maximum unambiguous range. In addition, the radar designer now has the option to compensate for signal path fluctuations in both spatial and temporal domains, within limits, by employing processing schemes that diagnose the nature of the signal corruption on a first pass and then reprocess with algorithms that compensate for the observed corrupting mechanisms.[96,97] The signal processing stage may also be tasked with extracting environmental information from the radar echoes, as mentioned in Section 20.8. This includes remote sensing of ocean winds and sea state, land-sea mapping for coastline recognition to assist with coordinate registration, measurements of the ionosphere for assimilation into ionospheric models, extraction of echoes from remote beacons deployed to assist with coordinate registration and calibration, and many other byproducts of the basic detection mission.

At present, the most powerful tools for dealing with additive interference, as well as some classes of spread-doppler clutter, are the techniques of adaptive processing. Originally, these techniques were developed for airborne microwave radars, but they have been shown to have wide applicability in HF radar.[135–138] The primary domain where major performance gains are realized is spatial analysis, that is, beamforming. In this context, a "snapshot" of the outputs from the all the receivers across the array is taken and used to compute a set of complex-valued weights for each desired beam direction; these are then applied to the receiver outputs before summing to form the adapted beams. The reason for the efficacy of adaptivity here is that, as remarked previously, HF radars are almost always external noise–limited. The azimuthal distribution of noise from thunderstorms, industrial sites and other sources is far from uniformly distributed. Furthermore, even so-called clear channels selected for radar operations are contaminated with directional noise of natural or industrial origin, albeit at a much lower level. Conventional FFT-type beamforming makes no allowance for this, so a lot of noise energy leaks into each computed beam through those of its (regularly spaced) sidelobes that are pointing toward strong noise sources. Spatially adaptive processing (SAP) reduces this problem by adjusting the amplitude and phase of the sampled receiver outputs in such a way as to minimize the integrated noise power leakage, while preserving the gain/sensitivity of the beam being synthesized.

Figure 20.23 compares conventional processing and SAP applied to the same block of radar data. A reduction of some 20 dB is achieved in this example, where noise, not clutter, is the problem. The pattern here has adapted to minimize the total energy collected in the doppler bands [–5,–1] Hz and [1,5] Hz, whilst maintaining the array
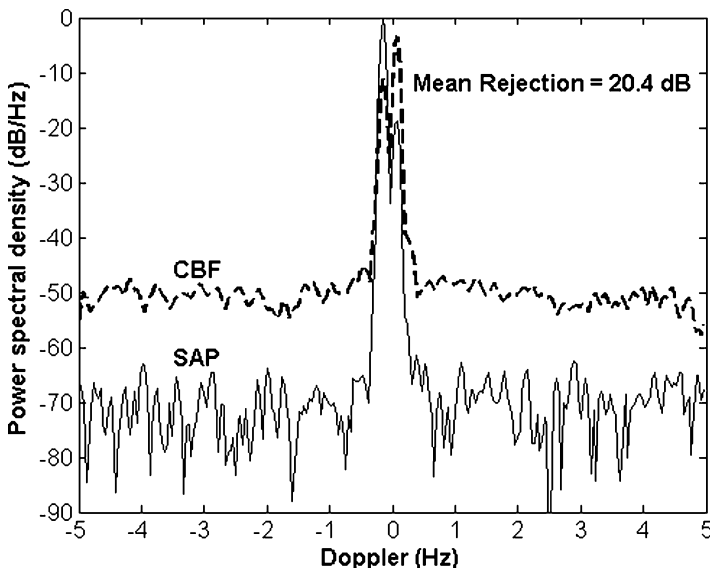
FIGURE 20.23 Comparison of doppler spectra estimated by (i) conventional beam-forming (CBF) and (ii) spatially adaptive processing designed to minimize energy outside the low-doppler clutter. The noise (and any fast clutter) has been reduced by ~ 20 dB, which improves detectability of fast targets; note that the sea clutter spectrum changes as a consequence of the new array pattern, i.e., the clutter spectrum does not necessarily represent the clutter spectrum from the cell of interest.

response in the specified direction. Of course, depending on the angular distribution of the noise sources, the array response pattern may have very high sidelobes, but they will lie in directions where the noise levels are lowest. The same may not be true of the clutter that occupies the low doppler band, [–1,1] Hz, which has not been used to guide the adaptation of the array response. Indeed, the resultant clutter spectrum may well have characteristics very different from those found in the steer direction. This is the case in the example shown in Figure 20.23, where the Bragg line ratio has changed dramatically and even reversed in sign.

In the example just given, the SAP weights were kept fixed for the entire CIT. When the external noise field is changing rapidly, as happens when the ionosphere is disturbed, it is necessary to adapt the weights during the CIT to maintain effective rejection of the noise as its azimuthal distribution changes, even for short (~1 s) dwells as used for aircraft detection. This is the province of space-time adaptive processing or STAP.[136] Here, the data used to determine the weights requires not just a single snapshot or average of snapshots but a number of snapshots of the array outputs; this block of data is then used to construct weights that are applied to the block of data before beamforming and doppler analysis. STAP is of particular importance to ship detection, where the external noise field almost invariably changes substantially during the long CIT. The complexity of STAP in this context arises from the fact that each time the weights are changed according to the SAP rules, the main beam experiences a phase shift, even though its amplitude gain/sensitivity is preserved. Thus, over the entire CIT, a sequence of phase shifts is applied, that is, a modulation, which is imposed on the received signal. As a consequence, the strong clutter echoes are spread in doppler, masking targets. To overcome this problem, Abramovich et al.[139] developed a technique known as the *method of stochastic constraints,* which uses different rules for weight adjustment, preserving not only the gain but also, to a good approximation, the phase of the clutter received via the main beam response.

Although these modern spatio-temporal adaptive processing techniques have been proven to be highly effective,[136] the computational and data requirements are so high that most of them cannot be implemented in their most powerful forms for real-time processing. Instead, simplified algorithms with impressive but nonetheless suboptimum performance are employed.[137,138]

In view of the number of simultaneous spatial cells to be considered, detection is generally based on a constant false alarm rate (CFAR) algorithm adapted to the particular clutter environment. In most implementations, the CFAR detection threshold is computed for each resolution cell as a linear combination of order statistics extracted from ranked sample values over a window spanning neighboring range bins, antenna beams, and doppler cells, with provisions for adapting the window shape near strong variations in noise or clutter power. Often the results are similar to those predicted by the log-normal distribution, as evidenced by the experimental data shown in Figure 20.22*b*, which gives the power-level distributions for the example shown in Figure 20.21. These approximately log-normal distributions are typical for benign conditions.

Tracking. Perhaps the most fundamental difference between skywave radar and other radars is the existence of multiple propagation paths, with distinct time delays, angles of incidence, doppler shifts, and fluctuation properties. The tracking stage must deal with the multiplicity of echoes associated with each individual target and, by extracting and assimilating information about the prevailing ionosphere, infer the number of genuine targets, their true locations and velocities, and perhaps

other information such as target altitude.[140] (Estimates of aircraft target altitude are very useful, but skywave radar has not proved to be a reliable means of obtaining accurate estimates.)

The problem of converting from radar coordinates to geographical coordinates is referred to as *coordinate registration (CR)*. Dozens of CR techniques have been explored, including (i) inference from a regional ionospheric model, (ii) deploying a network of repeaters or beacons in the radar footprint, (iii) correlating coastlines with land clutter—sea clutter boundaries in the radar data, (iv) correlating other parameters such as scattering coefficient, (v) using known target information such as reports from ships and commercial airline flights, and (vi) registering airports, where tracks originate or terminate. The key to robust CR is the fusion of all available information in a consistent probabilistic framework.[141] Most radars implement target tracking as a separate stage that operates on the candidate targets after they have been registered, initiating, updating, or terminating tracks, as appropriate. Experience with many different types of tracking schemes has led a number of operational radars to converge on algorithms based on variants of probabilistic data association (PDA),[142] sometimes generalized to maintain multihypothesis models.[143] Unlike traditional tracking filters such as the Kalman filter, which selects a single detection (i.e., peak or plot) to associate with each maintained track, PDA filters combine the influence of all the candidate peaks within a prescribed radius to compute a track update. In the skywave radar context, this has yielded superior results.

An important decision relates to where the coordinate registration is implemented. Some systems establish tracks in radar coordinates and then pass the tracks, including multiple tracks from a single target, to the CR system, which must identify and reconcile any multiple tracks as well as perform the registration. Alternatively, the problem of target tracking can be integrated with the problem of determining the ionospheric propagation paths. By augmenting the state vector used for representing a target with additional parameters that characterize the propagation path structure, a joint estimation problem can be formulated and solved.[144–147] In this way, the targets contribute to registering their own coordinates.

20.12   RADAR RESOURCE MANAGEMENT

The complexity of the HF radar operating environment—the ionosphere, clutter, noise, and other users of the band—necessitates a commensurate complexity in system design so that the radar can adapt to prevailing conditions by selecting the best frequency (or combination of frequencies[148]), waveform, signal processing, detection thresholds, and so on, for the task at hand. Achieving this optimum control is important because experience has shown that HF skywave radar performance may degrade dramatically with only modest departures from optimum settings. Thus, there is a demand for two ingredients: (i) information about the environment and (ii) a mechanism, or at least a strategy, for using that information to control the radar parameters.

At the very minimum, HF skywave radars must maintain a real-time awareness of propagation conditions as a function of frequency, range, and bearing (azimuth), as well as a detailed knowledge of spectrum occupancy. This is usually achieved by providing auxiliary facilities, including some or all of the following: (i) Conventional ionospheric sounders (vertical and oblique incidence), which determine the ionospheric electron density profile by measuring the time of flight of reflected radiowaves over a range of frequencies; this electron density profile information is assimilated into

local real-time ionospheric models. (ii) A wideband backscatter sounder, that is, a low-power, low-resolution radar that sweeps across the HF band, measuring echo strength versus time delay (group range), to see which frequencies are illuminating any given region. (iii) A mini-radar, similar to a backscatter sounder, that employs a narrowband waveform to study the doppler structure of the echoes as a function of group range for selected frequencies. (iv) A network of remote beacons or transponders to provide coordinate registration. (v) Spectrum monitoring receivers to locate clear channels for possible use and to assess their properties. A detailed description of the suite of auxiliaries for the Jindalee radar can be found in Earl and Ward.[149,150]

Traditionally, the control mechanism has been the expert radar operator. For many reasons, this is not wholly satisfactory, so various alternatives have been explored, including packaged "recipes" that can be invoked by less skilled operators and expert systems implemented with artificial intelligence constructs.

Apart from the need to adapt to the changing ionosphere and noise environment, HF radars are frequently tasked with a variety of missions to be conducted more or less concurrently, with time-varying priorities. These will generally involve different waveforms, task-specific constraints on frequency (in addition to propagation considerations), differing requirements in terms of acceptable propagation quality, and so on. A common example is the desire to search for ships and aircraft concurrently. Accordingly, optimization of the allocation of resources becomes a critical issue, with significant implications for the way skywave radars operate.

One approach to fitting more tasks into the time available is to partition the radar transmit and receive arrays, together with the transmitter modules and receivers, so that when conditions are favorable, the partitions can operate as independent radars with reduced sensitivity and resolution. For example, the Jindalee and JORN radars are dynamically reconfigurable as full or half radars. Alternatively, it may be acceptable to employ a dual-purpose waveform, able to support two distinct missions, though with suboptimal performance, or for the transmit system to radiate multiple orthogonal waveforms for simultaneous reception and processing at a proportional loss of average power on each transmission but without loss of spatial directivity. But even if these approaches are sometimes applicable, it is almost always necessary to schedule the various tasks such that acceptable revisit times are maintained on important missions, with low priority tasks, such as weather monitoring, activated less frequently, and challenging tasks activated when suitable propagation conditions occur.[151]

One other important issue arises with resource management and that is the ability to diagnose faults and failures as soon as they occur. Not only is this necessary to hasten the repair procedure, but also it enables the radar to adapt its configuration to do the best it can with impaired equipment. For example, if the receiver connected to the middle element in an antenna array were to fail, beamforming would be more seriously degraded than if the failure were to occur in a receiver connected to an element at the end of the array. Automatic detection of such a failure and reallocation of an end element receiver to the middle element of the array would minimize the degradation.
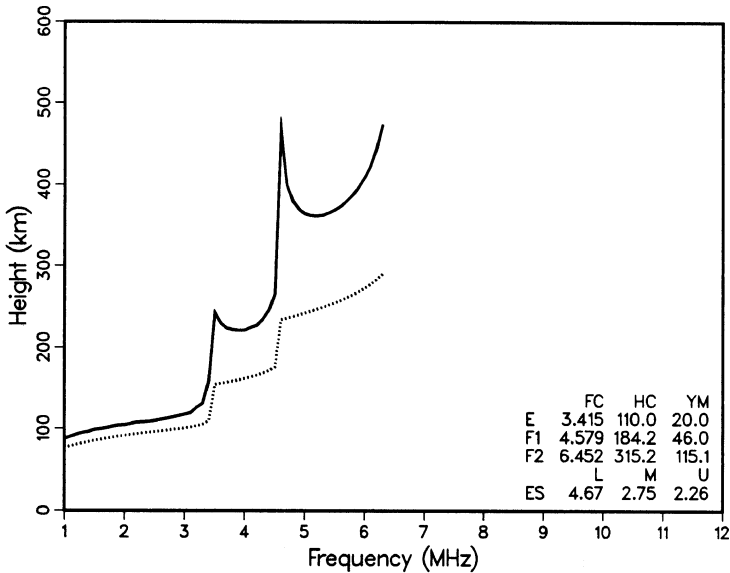
20.13   *RADAR PERFORMANCE MODELING*

Modeling is an essential part of the radar design process and also as a means to predict the performance of existing or proposed radars to which one does not expect access. In these roles, the emphasis is on fidelity. In HF skywave radar systems, modeling has

another role—as a real-time monitor of what is expected under the prevailing conditions, so as to alert the radar operator if a discrepancy emerges, which might be indicative of natural, equipment-related, or intentional events warranting attention.
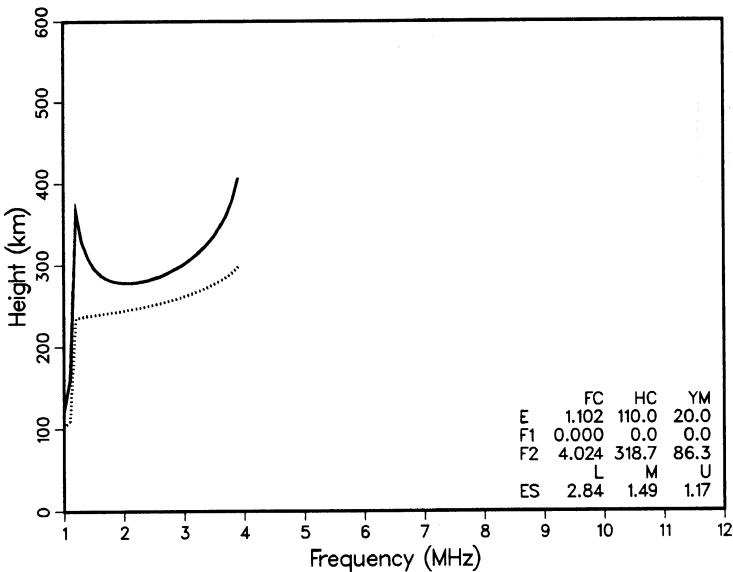
An issue one encounters when discussing radar performance is the choice of performance criterion. From the user's perspective, it may seem logical to measure performance in terms of time taken to establish a track on a given target, averaged over time and coverage, since tracks are the essential product delivered to users by the radar. Of course, this places the onus on the tracking system, so one might step back a little and choose instead SNR achievable on a given target, again averaged over time and coverage. But this ignores the precision of the measurement, associated with both resolution, which may impact on the utility of the detections, and accuracy, in the sense of registration in absolute (geographical) coordinates. And what of the smallest detectable target? Coverage and coverage rate? Ship detection capability versus aircraft detection capability? Clearly, there is no single preferred metric.

The measure adopted here for illustrative purposes is the achievable signal-to-noise ratio (SNR) as defined by the radar equation (Eq. 20.2). The constituent variables that appear in the equation have been discussed in Sections 20.4–20.11, emphasizing the unique considerations that arise with HF skywave radar, so the tools for performance modeling and analysis are available. By considering the case of noise-limited detection, as applies especially to aircraft targets, the additional complications of clutter-limited detection are avoided. In the following paragraphs, two different approaches to performance modeling for the case of noise-limited detection are described in some detail.

The NRL-ITS Radar Performance Model.   The NRL-ITS Radar Performance Model developed by Lucas et al.[152] provides a number of tools for radar performance estimation. It does not employ full 3D ray-tracing, such as the code described by Jones and Stephenson,[50] which can provide paths in three dimensions, including delays and losses for both ordinary and extraordinary rays (see Section 20.4). Arguing that such comprehensive calculations are excessive when there are significant uncertainties in the electron density distribution, NRL Memorandum Report 2500[152] describes the basic technique used for path determinations. A simple closed-form virtual path trace, Snell's law for a spherically symmetric medium, is sequenced through elevation radiation angles in 1° increments. This process is incremented in 1-MHz steps over the radar's operating band. In the present example, a vertical sounding of the ionosphere 700 km downrange has been used as the electron distribution for all one-hop paths, and a sounding 1400 km downrange is used for two-hop paths. Figure 20.24 gives night and day examples of ionograms showing the ionosphere 700 km downrange from a radar located at 38.65°N and 76.50°W looking east, in summer at a median sunspot number of 50. The corresponding winter case is presented in Figure 20.25. Such plots can be used to determine the maximum frequency that will propagate to a given range; in most cases, the optimum frequency is just below the maximum frequency. For the little tables shown in Figure. 20.24 and 20.25, FC is the critical frequency, in megahertz; HC is the height of maximum ionization or the nose of the parabola, in kilometers; and YM is the semilayer thickness, in kilometers. Es describes the statistical range of variation of sporadic-E as M (median), L (lower decile), and U (upper decile) critical frequencies, in megahertz.
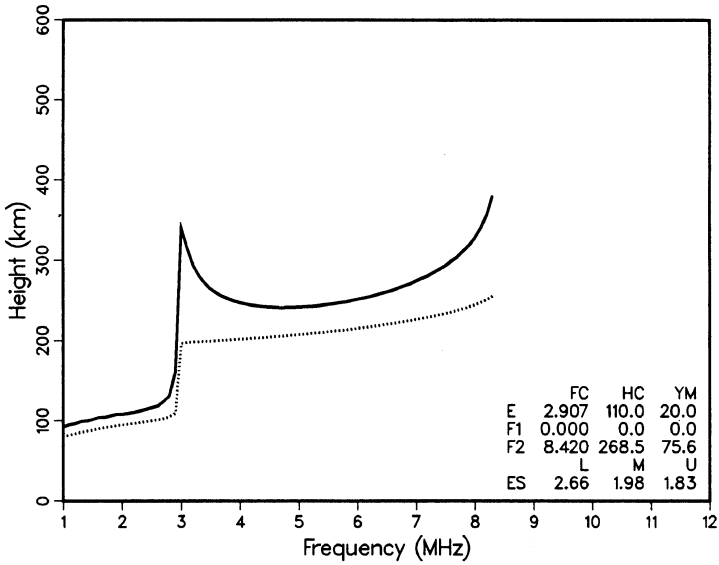
	FC	HC	YM
E	3.415	110.0	20.0
F1	4.579	184.2	46.0
F2	6.452	315.2	115.1
	L	M	U
ES	4.67	2.75	2.26

(a)

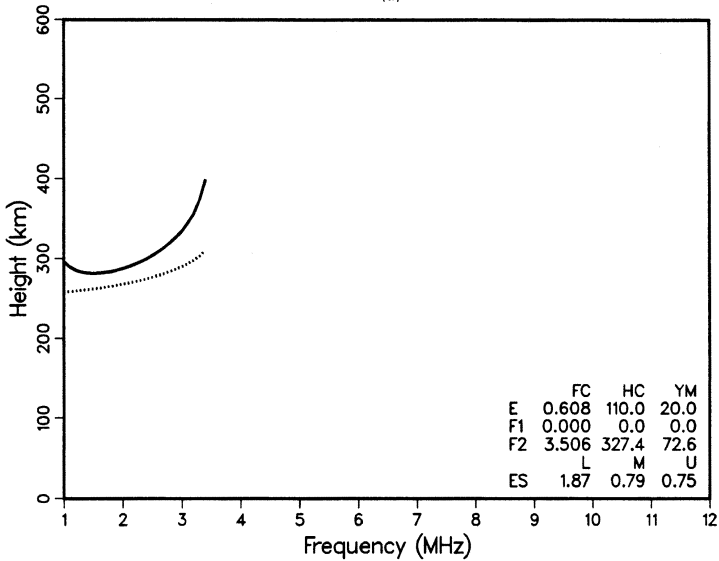|	FC	HC	YM
E	1.102	110.0	20.0
F1	0.000	0.0	0.0
F2	4.024	318.7	86.3
	L	M	U
ES	2.84	1.49	1.17

(b)

FIGURE 20.24 The virtual (solid line) and true (dashed line) reflection heights are given for July, SSN = 50, and a mid-Atlantic coast refraction area: (*a*) 1800 UT is a daytime example, single hop and (*b*) 0800 UT is a nighttime example. See text for an explanation of the table in the lower right of the figure.

	FC	HC	YM
E	2.907	110.0	20.0
F1	0.000	0.0	0.0
F2	8.420	268.5	75.6
	L	M	U
ES	2.66	1.98	1.83

(a)

	FC	HC	YM
E	0.608	110.0	20.0
F1	0.000	0.0	0.0
F2	3.506	327.4	72.6
	L	M	U
ES	1.87	0.79	0.75

(b)

FIGURE 20.25   Predicted ionograms as in Figure 20.24, but for January: (*a*) 1800 UTC for day and (*b*) 0800 UTC for night. See text for an explanation of the table in the lower right of the figure.

Constant plasma-frequency contours versus range from the radar for 0800 UTC, SSN 50, January (night) and 1800 UTC (day) are presented in Figures 20.26 and 20.27 to illustrate the tilt of the ionosphere. For the night case, the concentric
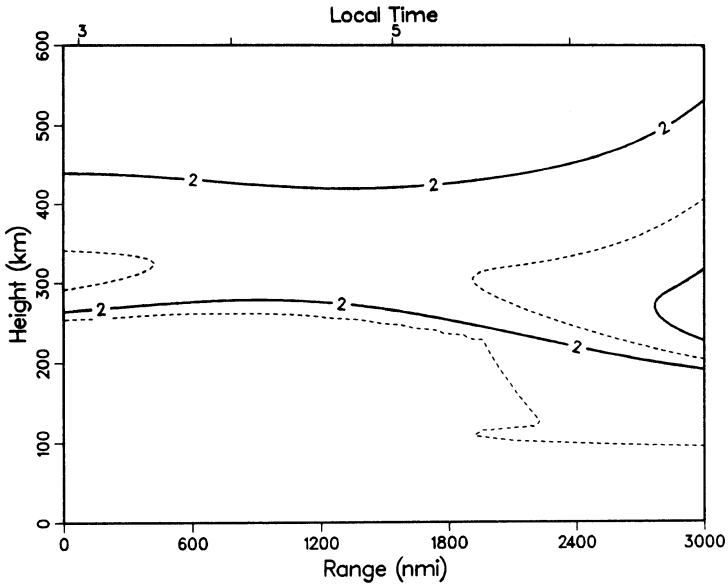
FIGURE 20.26 Plasma-frequency contours are given in MHz, extending from the radar to a point east 3000 nmi downrange, for a January night example.
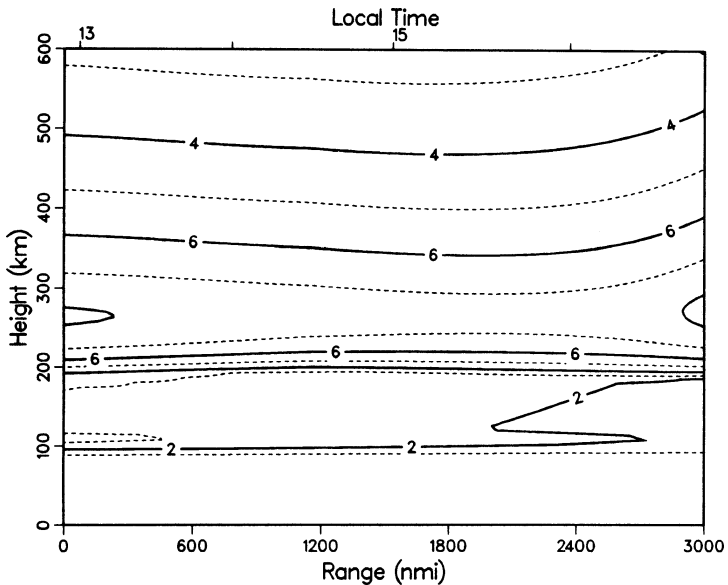
FIGURE 20.27 Plasma-frequency contours are given in MHz, extending from the radar to a point east 3000 nmi downrange, for a January day example.

spherical assumption from the 700-km downrange position will give paths that are slightly long for one-hop ranges. In the two-hop ranges, the no-gradient assumption causes more distortion. In general, errors of this nature have little impact on performance prediction. However, near-real-time analysis for virtual range and azimuth correction to great-circle distance and bearing (grid registration) requires that tilt or gradient effects be taken into account. The daytime example has little horizontal gradient, and the simplifying assumption makes little difference. When better accuracy is desired, the correct vertical profile can be used for each radiation angle; also, gradients can be simulated by making the ionosphere nonconcentric with the Earth. A more complete path analysis should be used in radar performance assessment and management, but these plasma density contours can be used to estimate the magnitude of the errors introduced by the assumption of a spherically symmetric ionosphere.

Figure 20.28 shows a performance prediction for a hypothetical radar in the form of an oblique sounding. A typical skywave radar is supported by one or more vertical sounders and oblique backscatter sounders for transmission-path analysis and to aid in radar-frequency management. Of course, the radar itself is an oblique sounder, but its sounding data is restricted to the frequency, waveform, and scan program of its primary surveillance task. An adjunct oblique sounder can provide information in
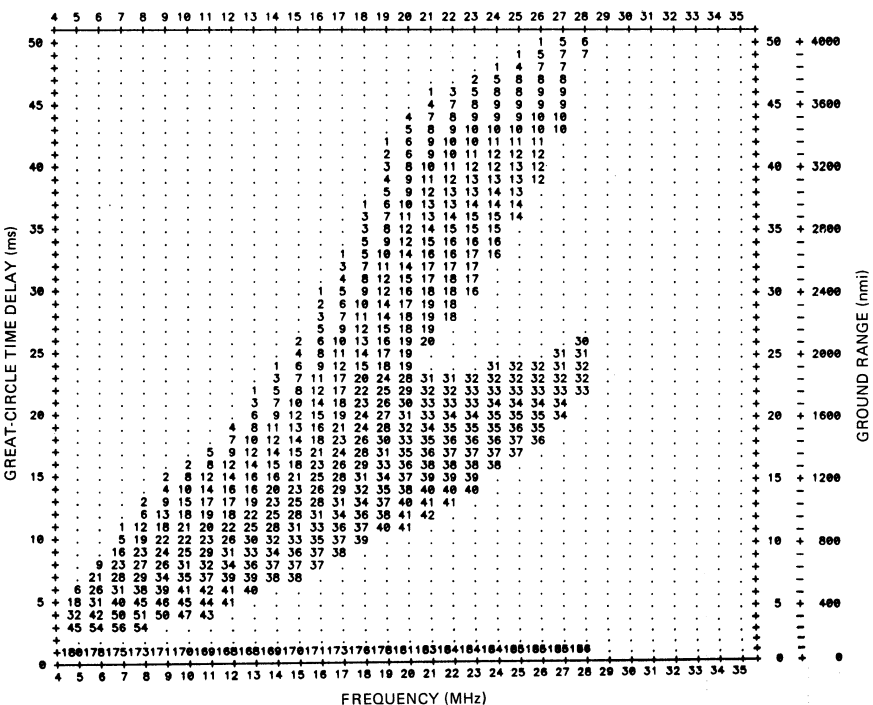
FIGURE 20.28 The numbers in this figure show the SNR in dB as a function of frequency and range in the form of a typical oblique backscatter sounding: January, 1800 GMT (day), SSN 50, location 38.65°N and 76.53°W, bearing 90°. See the text for a description of radar parameters.

the form of Figure 20.28 on Earth backscatter echo power. Estimates for noise power spectral density are derived from CCIR Report 322-3, as described in Section 20.9. In this prediction, SNR in decibels is plotted as a function of operating frequency and great-circle time delay or ground range. The numbers just above the abscissa (at 1-ms delay) are the noise powers in decibels below 1 W/Hz. For this plot, the UTC time is 1800, SSN = 50, P_{av} = 200 kW, G_tG_r = 50 dB, T = 1 s, and σ = 20 dBsm. Figure 20.29 gives the corresponding night plot.

The shape of these displays is quite similar to what would be seen with a diagnostic oblique sounding; the levels would generally be greater because the resolution cell area times the surface scattering coefficient is generally much larger than 20 dBsm. Some of the night-day contrasts, such as available frequencies and difference in noise level for the same range, are evident. Also note that at night the 5-MHz lower frequency limit does not provide coverage closer than about 900 km. It should be remembered that this is a median SSN 50 calculation, and if consistent performance for ranges as close as 900 km is required during nights, a lower frequency limit should be selected to deal with periods of lower solar activity and the critical frequency distribution. The plots show that operation on a single frequency may experience less than ±3 dB variation over a range interval of 1000 km. Also, if frequency selection had been made with a 2-MHz granularity instead of the 1 MHz used, the SNR would be reduced by only a decibel or so.
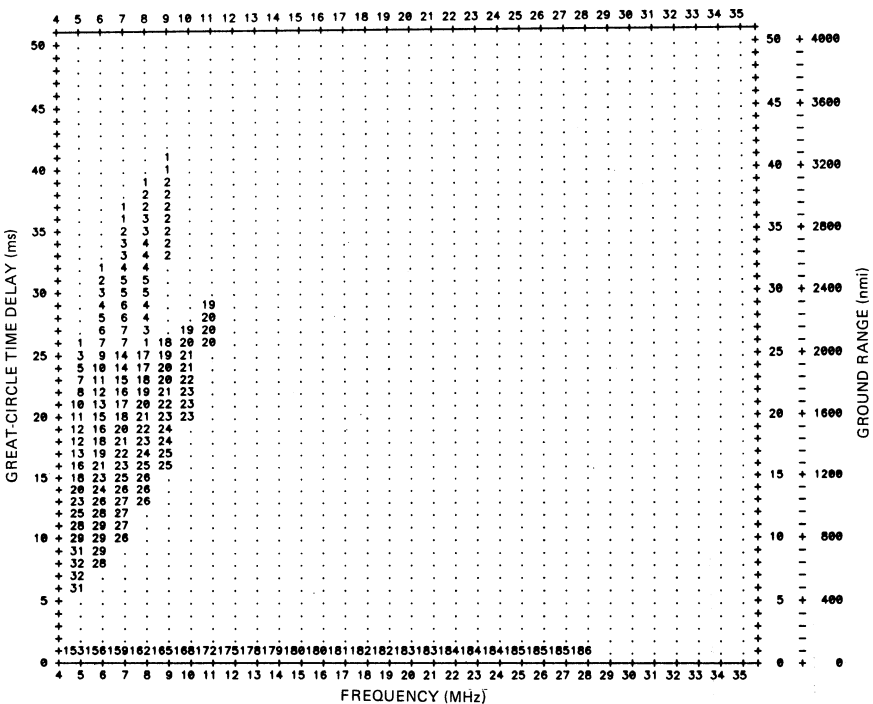
FIGURE 20.29   The numbers in this figure show the SNR in dB as a function of frequency and range in the form of an oblique sounding, as in Figure 20.28, but for 0800 GMT (night). See the text for a description of radar parameters.

The performance estimation charts that follow come from analyses as described above. After performing oblique sounding calculations, a range-indexed table of propagation and noise parameters is compiled. Parameter selections are made on the basis of the best SNR in each nominal 50-nmi interval, but the selection is adjusted to come from the adjacent lower frequency to avoid an optimistic bias. Then parameter plots are generated as a function of range. The variables adopted here as parameters are propagation losses, frequency, noise, and elevation radiation angle. The choice of range as the independent variable may seem artificial, but it is a useful approach for performance examination. With these curves, the impact on radar SNR performance can be estimated for selected antenna gain patterns, transmitted powers, target RCS, and coherent integration times (CIT).

Figure 20.30 is an example for January with moderate solar activity, SSN = 50, in daytime. The R^4 loss is the fourth power of range to the target in meters, expressed in decibels. $R^4 + L$ adds nondeviative absorption, deviative absorption, sporadic-E obscuration, and ground-reflection losses if there is more than one hop. The sharp increase in loss just before 2000 nmi is caused by transition from one to two hops; for two hops, the lossy D region is transited twice as many times, ground-reflection loss is added, and required operation at a lower frequency increases loss. The jagged curve in the transition region is due to the parameter selection process; in radar operation, the frequency would be selected to minimize transition effects. The frequency, radiation angle, and noise power per hertz that go with this site and look direction are also plotted.
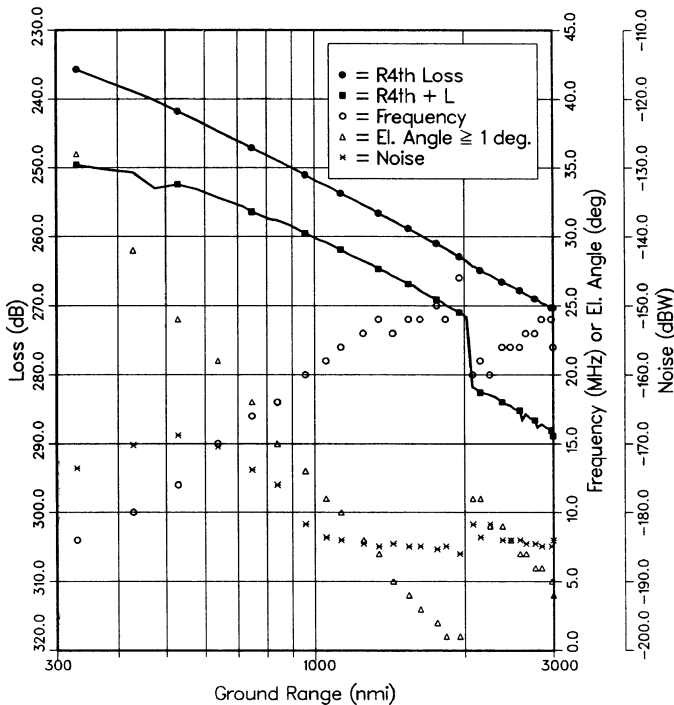

FIGURE 20.30   Radar performance-controlling variables plotted as a function of range for January, 1800 UTC, SSN 50.

An example will serve to illustrate the use of such plots. Select 1000 nmi as the range. Then, the frequency is 20.5 MHz (wavelength = 14.6 m and $\lambda^2 = 23$ dB), noise power = −182 dB, and $R^4 + L = 260$ dB. Choose 53 dBW for P_{av}, 20 dB for G_t, 30 dB for G_r, 0 dBs for T, 20 dBsm for RCS, and 6 dB for F_p. Substituting in Eq. 20.2,

$$SNR = 53 + 20 + 30 + 23 + 0 + 20 + 6 - 33 - 260 - (-182) = 41 \, dB$$

Figure 20.31 shows the performance indicated with these assumptions for all ranges. A path factor enhancement of 6 dB has been chosen as a representative value of constructive multipath interference for an aircraft target. The beamwidth has been taken to be 5.7° and the surface scattering coefficient to be −35 dB, and with a 12 dB path enhancement, the clutter level has been plotted. The clutter-to-noise ratio (CNR) at 1000 nmi is about 88 dB. For the constant beamwidth assumed, the clutter-to-signal ratio increases with range and is 47 dB at 1000 nmi. Large clutter-to-signal ratios are typical of HF radar; some form of doppler filtering is used to separate targets from clutter.

In Figures 20.32, 20.33, 20.34, and 20.35, performance estimation curves are given for winter and summer seasons, night and day, and low solar activity. The permissible frequency selection is set between 5 and 28 MHz, and antenna radiation is not considered below an elevation angle of 1°. The analyses were made for a radar off the mid-Atlantic coast of the United States and should be a good approximation for any location where transmission paths are through the middle magnetic latitudes.
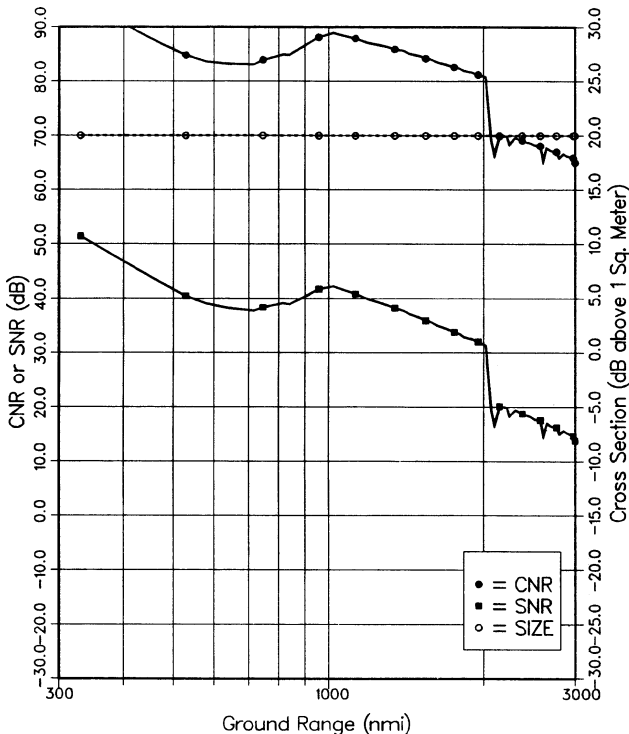
FIGURE 20.31 A specific example of SNR and clutter-to-noise ratio (CNR) as determined by using Figure 20.30. The target RCS is labeled "size" and is treated as constant.
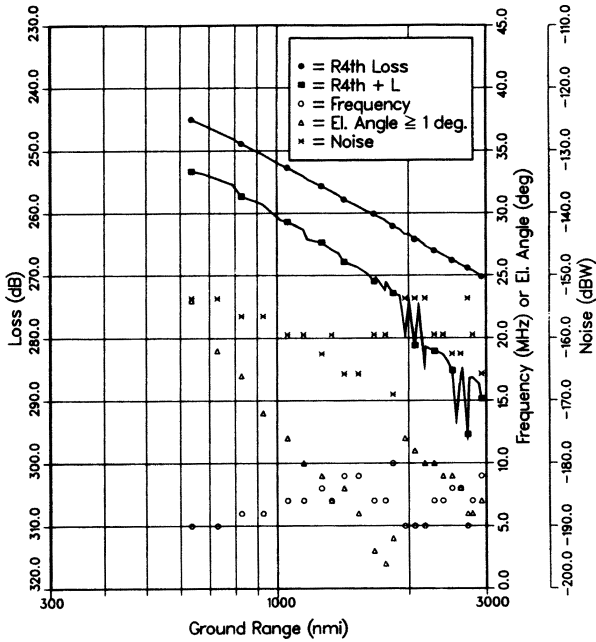
FIGURE 20.32 Radar performance estimate for January 0800 UTC, SSN = 10
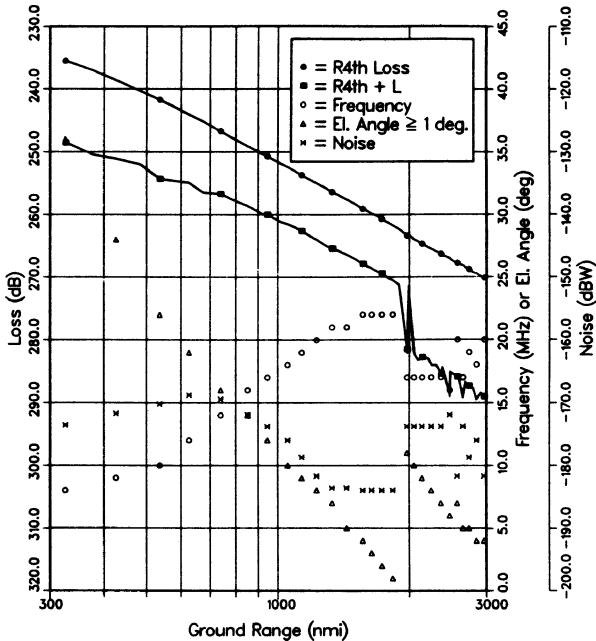

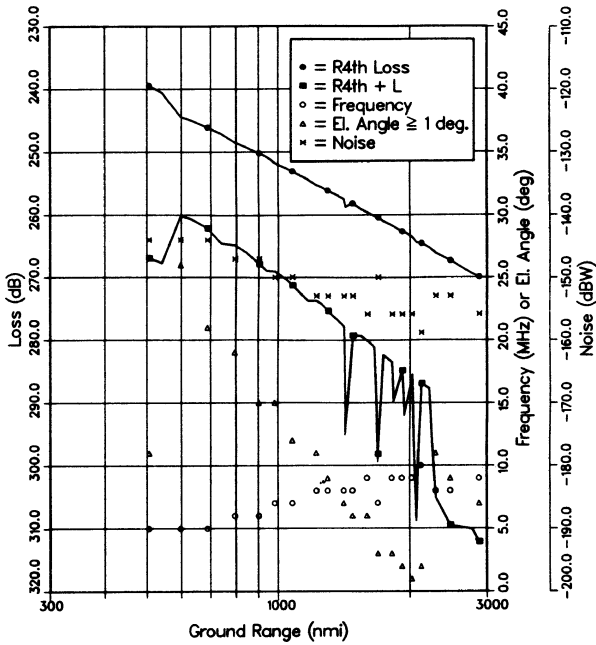**FIGURE 20.33** Radar performance estimate for January 1800 UTC, SSN = 10

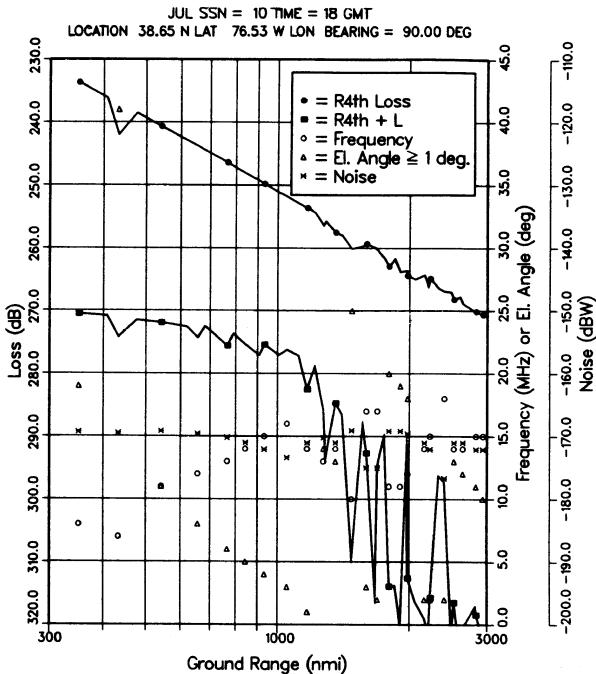**FIGURE 20.34** Radar performance estimate for July 0800 UTC, SSN =10

FIGURE 20.35 Radar performance estimate for July 1800 UTC, SSN = 10

These performance estimation curves can be used to show extremes in SNR variation, antenna elevation angles required, and expected clutter-to-noise ratios. The expected performance of a particular radar design can be explored with these graphs because summer and winter do give good coverage of the important variables. The performance curves have been limited in almost all examples to the case of low solar activity, since, in general, this is the most difficult time. The higher frequency availability and performance afforded at high solar activity is illustrated in Figure 20.36, which treats the case of July 1800 UTC for SSN = 100.

Analysis of performance estimation curves for all combinations of (i) the four seasons, (ii) day and night, and (iii) high and low solar activity[153] reveals consistent behavior:

(i) Summer shows much greater losses than winter.

(ii) Except for summer, night losses are only slightly less than day losses.

(iii) Night noise is much greater than day noise.

(iv) For a specific range, optimum frequencies vary by 3:1.

This OTH performance presentation format can be used to decide on the antenna patterns and powers required for specific targets and missions, or it can be used to exhibit periods of enhanced or degraded performance for an existing design.[154]
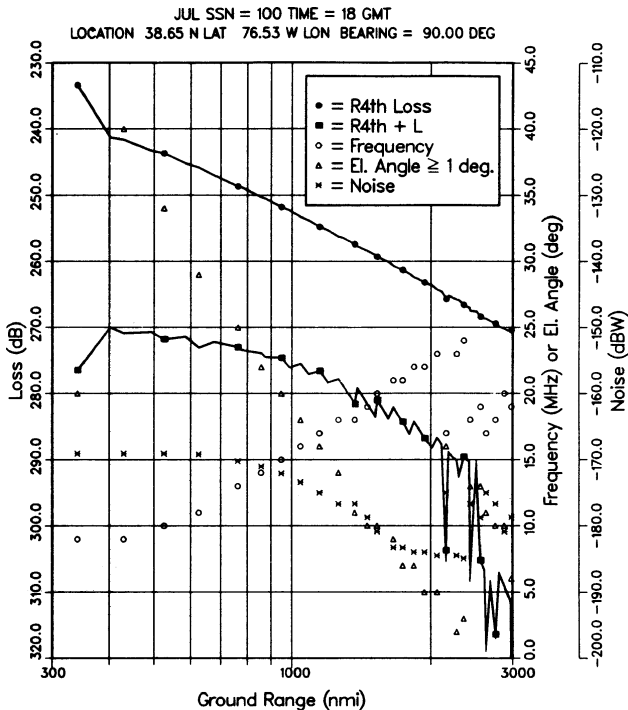

FIGURE 20.36 Radar performance estimate for July 1800 UTC, SSN = 100

Several qualifiers should be kept in mind. At other geographic locations, the appropriate CCIR noise should be selected or, better yet, noise measurements made in situ. For radars that use auroral zone paths, specific analyses are required and target obscuration by spread-in-doppler clutter must be considered. The performance estimates shown in the figures assume that the radar design and waveforms are such that external noise is the control. The use of a single description for night and day gives a fair representation, but the transition from night to day is very abrupt and requires careful frequency management in radar operation. The ionospheric description that has been used is for what has been termed the *quiet ionosphere,* conditions that apply most of the time. Under disturbed conditions, performance may be markedly inferior to that predicted.

The Jindalee Radar Performance Model.   The Jindalee Radar Performance Model draws on several unique databases. Since 1984, oblique backscatter soundings have been recorded on a 10 minute cycle, scanning from 5 to 30 or (optionally) 45 MHz.[149,150] Eight simultaneous beams spanning a 90° arc are formed. Prior to 1991, the system used a single receiver scanning the 8 receive beams, servicing each receive beam for 25 kHz of each 200 kHz portion of a backscatter ionogram. Post-1991, each beam has been serviced continuously with its own receiver. Background noise data used in conjunction with the backscatter data for the Excess Power analysis is collected using the same eight directional beams as the backscatter sounder.

While there are a few significant gaps in these time series, they span two solar cycles; further, integrity has been maintained by extensive vetting before entering new data into the database. The unique advantage of this database is that the noise and propagation data are recorded under identical ionospheric conditions, whereas combining independent clutter and noise statistical models such as IRI-2001 with CCIR 322-3 preserves no correlations, however strong they may be.

Several forms of data analysis and display are accessible, but perhaps the most useful are the maps of (i) Excess Power and (ii) Optimum Frequency. The Excess Power parameter is constructed as follows. Consider a specific target whose RCS is known or estimated as a function of frequency. Suppose a prediction of median radar detection performance is required for a specific month of the year and a particular sunspot number or year of solar cycle.

Analysis is initiated by selecting from the database a month that matches the requirements. Individual backscatter ionograms are paired with the concurrent background noise data and the ratio taken to yield a population of estimates of true sub-clutter visibility (SCV) for each frequency step, each beam, and each range bin. Next, using a specified time granularity—typically one hour—median values of SCV are calculated for each spatial cell and time interval from the statistical population of individual SCV estimates. Note again that these median values are the median values of the SCV population, not a statistic derived by combining median values of clutter with median values of noise.

The median SCV values are related directly to the backscatter sounder transmit power and the transmit antenna gain. From the radar equation (Eq. 20.2), the SCV can be scaled to that which would be expected for the main radar, with its different radiated power P_T, aperture, radar bandwidth, etc. Combining these scaled SCV values with (i) a model of the surface backscattering coefficient versus frequency (almost all the OTH radar coverage is ocean, so based on regional wave statistics, the constant value –23 dB is used); (ii) the target RCS versus frequency model; and (iii) an estimate of the target echo signal processing loss, typically ~ 12 dB, which arises predominantly from FFT analysis, yields the predicted median target SNR at each spatial location as

a function of frequency. This can be used directly, but it is convenient to define the Excess Power at each frequency as follows.

Suppose:

- An SNR threshold of M dB is required before the signal processing will register a detection and

- The SNR calculated for a particular range-azimuth cell in the coverage is $\text{SNR}(f)$ dB (which may be negative)

Then, in dB,

$$\text{Excess Power }(f) = M - \text{SNR}(f) + P_T - P_{\text{REF}}$$

is the amount of extra power, relative to any chosen reference power P_{REF}, needed to achieve detection as a function of frequency. A negative value indicates that the radar has greater sensitivity than required. Figure 20.37 shows an example presented as a contour plot. The second parameter of special interest is optimum frequency, defined as the value of the frequency at each range-time location that maximizes the SNR for the given target, taking all radar equation factors into account. Again, a contour plot format is used here in Figure 20.38.

Other Modeling Approaches.   The models described above are formulated in the context of the radar equation (Eq. 20.2). An alternative is to employ a coherent "process model," in which the field amplitude and phase are tracked from transmitter to receiver. This approach has been used to simulate the effects of multipath, diffuse scattering, polarization effects, and nonlinearity.[69,70,155] For example, Figure 20.39 shows
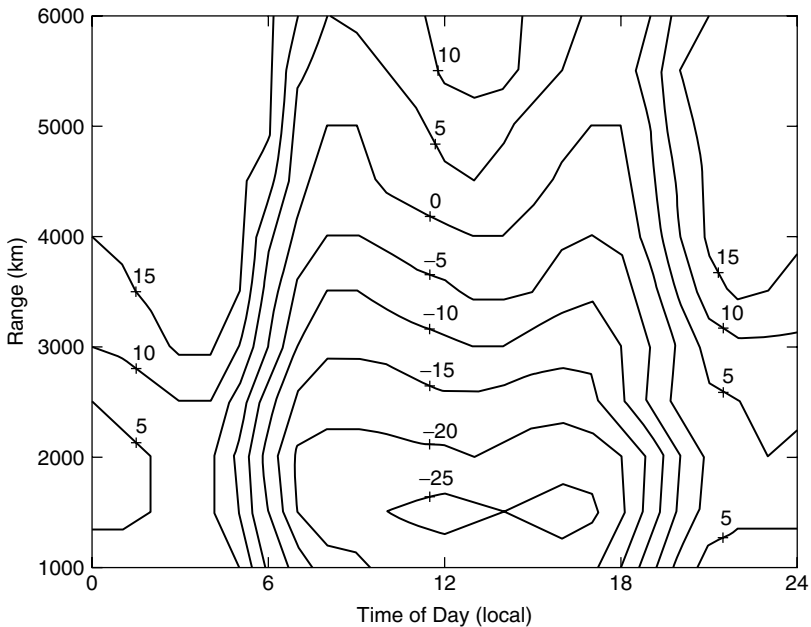
FIGURE 20.37   Range-time map of power required, relative to a P_{REF} of 100 kW, to detect a specific target, as a function of range and time-of-day, for a particular month and level of solar activity
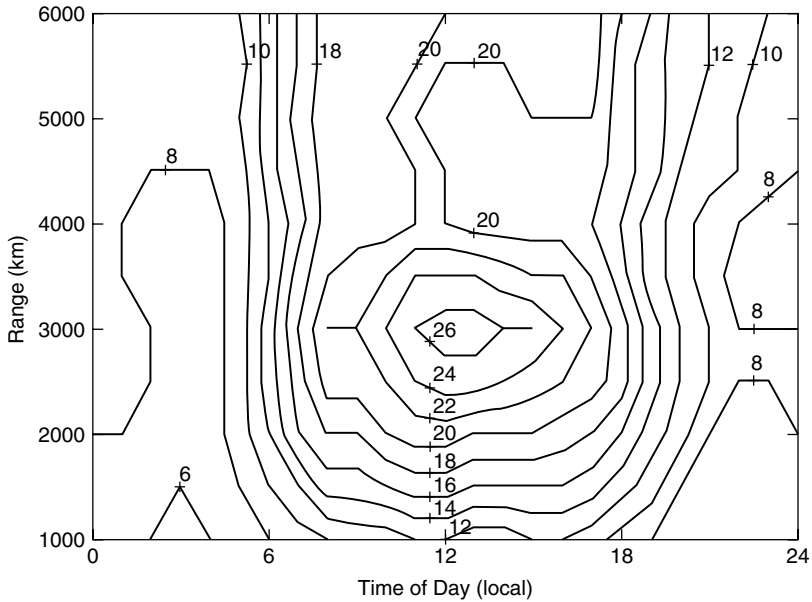
FIGURE 20.38   Range-time map of optimum frequency in MHz to detect a specific target, as a function of range and time-of-day, for a particular month and level of solar activity

the predicted distribution of the resultant radar cross section when multipath and Faraday rotation are taken into account. The relevant physics—rough surface forward scattering coefficient, bistatic (in the vertical plane) free-space target scattering cross
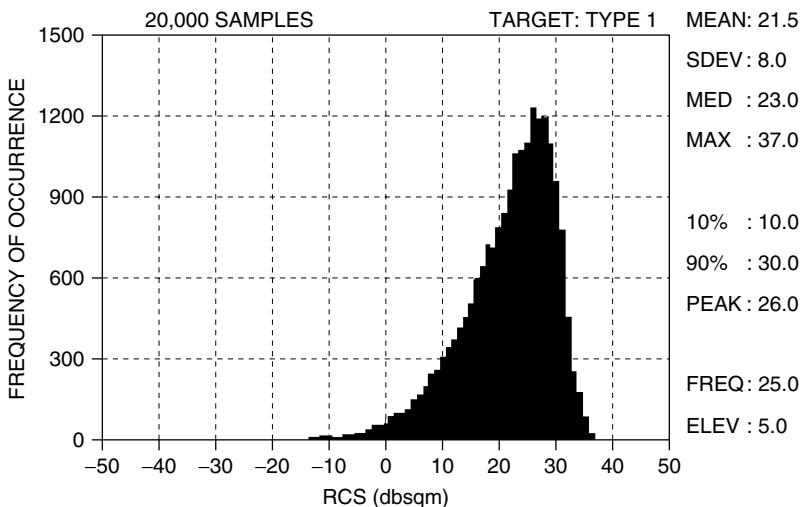
FIGURE 20.39   Predicted distribution of effective RCS for the Aermacchi MB326H trainer jet aircraft viewed nose-on at a height of 1000 feet when ground-reflection multipath and Faraday rotation are taken into account.

section for hybrid multipath, Faraday rotation, and differential Faraday rotation—are incorporated via parametric models derived from measurements or computational electromagnetics and the distribution obtained by Monte Carlo simulation.

APPENDIX: HF SURFACE WAVE RADAR

General Characteristics and Capabilities. Although skywave propagation provides the unique capability of low altitude target detection at ranges of thousands of kilometers, other forms of propagation at HF can be exploited in radar applications. By far the most common of these is *ground wave* or *surface wave* propagation, which is most effective for vertically polarized radiowaves traveling over highly conductive surfaces such as seawater. In addition, there are applications for which line-of-sight or spacewave propagation is appropriate, such as measurement of the HF RCS of aerospace vehicles. Furthermore, in many instances, bistatic configurations can be employed, with the possibility of using different propagation mechanisms for transmitter-target and target-receiver paths. In view of the familiarity of space wave propagation and the preceding discussion of skywave systems, it suffices here to address the main features of HF surface wave (or ground wave) radar (HFSWR).

HFSWR systems tend to fall into two categories: (i) low-power radars intended primarily for oceanographic remote sensing, especially of ocean currents, and (ii) larger and more powerful systems with target detection as their primary mission. The former are in widespread operation around the world; only a few of the latter are operational in surveillance roles. The ability of the low-power remote sensing radars to detect ships at over-the-horizon ranges, although modest, has been exploited in some dual-purpose deployments.

The principal virtue of HFSWR as an ocean surveillance radar lies in its ability to detect small surface vessels and low-flying aircraft at ranges far beyond the visible horizon. As with skywave radar, performance depends strongly on environmental and target parameters, as well as radar design; the detection ranges cited in Table 20.3 provide some indication of capability against surface vessels and low-flying aircraft, as claimed or reported for several established HFSWR systems.

TABLE 20.3 Nominal or Claimed Maximum Detection Ranges (kilometers) of Some HFSWR Systems
(SeaSonde is a compact low-power radar designed primarily for remote sensing; it is available with an upgraded performance option. The other radars shown were designed for surveillance. In all cases, performance may fall far short of the cited values under inclement environmental conditions.)

TARGET TYPE	SWR 503 Raytheon Canada	HFSWR BAE Systems UK	SECAR Daronmont Australia	Podsolnukh-E Niidar Russia	SeaSonde Codar US
Frigate	520	> 200	> 400	260	190
Offshore trawler	450	85	> 250	180	120
Small fishing boat			120		65
Go-fast speed boat			70		35
Rigid inflatable boat		22			
Low-flying fighter-sized aircraft		75	> 200		

Much of the discussion relating to skywave radar carries over directly to HFSWR, but there are a few areas where differences are significant:

- The antennas must be designed and positioned to achieve high efficiency in coupling to the surface wave mode. Experiments have shown that higher field strengths are generated at over-the-horizon ranges when the transmitting antenna is located close to sea level, rather than in an elevated position; placing the antenna even just one or two wavelengths above sea level can introduce several dB of additional loss.[156]

- Most HFSWR systems use a very broad "floodlight" transmit beam to illuminate the entire coverage arc; multiple simultaneous receive beams are formed to fill the arc and update all tracks simultaneously. This reduces cost and complexity but incurs some loss of sensitivity for noise-limited target detection.

- Coherent integration times may extend to hundreds of seconds, as HFSWR is not reliant on the ionosphere as a medium for propagation.

- Only vertically polarized electromagnetic waves propagate effectively in the surface wave mode over the sea, so the HFSWR signal-receiving antennas are necessarily vertically polarized. On the other hand, unwanted signals and interference arriving by skywave may have any polarization. This presents a means for rejection of interference by filtering in polarization space: any signals correlated with those received on an auxiliary horizontally polarized receive antenna can be cancelled from the outputs of the vertically polarized array.

- The increasingly rapid attenuation of propagation to ranges beyond about 200 km, as shown in Figure 20.40, means that at longer ranges, relatively little detection performance improvement is gained by large increases in transmitted power.

- The rate of decay of the surface waves rises sharply with increasing frequency, as shown in Figure 20.40, whereas the RCS of small targets tends to increase rapidly and external noise decreases. It follows that radar design is sensitive to the classes of targets to be detected.

- While HFSWR does not rely on the ionosphere, echoes from irregularities in the ionosphere may appear at ranges in excess of ~100 km, Similarly, ground reflections received via oblique skywave propagation may appear at ranges in excess of ~200 km. Such echoes may be spread in doppler and can constitute a serious problem for HFSWR systems. Accordingly, antennas should be designed with low gain at higher elevation angles.

The main design parameters of a representative HFSWR system—the Daronmont SECAR radar—are listed in Table 20.4. (The corresponding values for skywave radars can be found in Table 20.2.)

Propagation Considerations in HFSWR Systems.   To a good approximation, when a target of interest is above the optical horizon of an HFSWR, the field incident on the target can be decomposed into terms that correspond to (i) direct line-of-sight, (ii) sea-surface reflection, and (iii) a lateral or "surface-attached" wave. Beyond the horizon, the surface wave is the dominant contributor, but at shorter ranges, all three mechanisms must be taken into account. Accordingly, the relationship between (i) target echo strength and (ii) the range and altitude of the target is not a simple one. Moreover, the calculation of the field distribution is computationally expensive if

TABLE 20.4 Specifications of SECAR, an HF Surface Wave Radar Designed for Surveillance of the 200 nmi Exclusive Economic Zone

Radar	SECAR
Manufacturer	Daronmont Technologies
Type	Bistatic HF surface wave radar
Tx-Rx site separation (km)	50–150
Power (average) (kW)	5
Power (peak) (kW)	5
Frequency band (MHz)	4–16
Waveform	linear FM-CW
Bandwidth (kHz)	10–50
Waveform repetition frequency (Hz)	4–50
Tx antenna design	Single vertical log-periodic antenna with ground screen
Rx antenna design	16 or 32 endfire monopole doublets with ground screen
Rx aperture (m)	200 – 500
Beamwidth 4 MHz	> 9°
16 MHz	> 2°
No. of simultaneous beams	16 or 32
Instantaneous range depth (km)	100–500
No. of range bins	10–200
Coherent integration time (CIT) (s)	1–120
No. of doppler cells	32–512
Max. velocity resolution (ms^{-1})	< 0.5
Primary mission	Ship detection
Revisit time for entire coverage area	Equal to CIT
Secondary missions	Aircraft detection Remote sensing
Number of simultaneous targets tracked	> 200

accurate predictions are required. The difficulties are compounded when mixed paths are involved; that is, when part of the propagation path lies over land, as happens where islands are present in the coverage area.

Focusing attention here on over-the-horizon detection, Figure 20.40 shows how the surface wave decays with range, parametric in frequency for the case in which both the radar antenna and the target are near the sea surface. These curves are for a smooth surface and use a 4/3 earth radius to approximate atmospheric refraction effects. The propagation code used here is due to Berry and Chrisman,[157] and it is quite flexible, permitting antenna and target altitudes, surface conductivity and permittivity, polarization, and frequency to be specified. The key points to be drawn from this example are (i) the apparent advantage to be gained by operating at low frequencies where propagation losses are minimized, though this benefit must be balanced against antenna size, the higher noise environment, and (often) reduced target RCS; and (ii) the rapidly accelerating fall-off in signal strength at ranges beyond a few hundred kilometers, where 10 dB of extra transmit power may buy only on the order of 10 kilometers of additional detection range.

A more widely used propagation code is GRWAVE,[158] which employs different mathematical representations for the field, depending on range and other parameters, so as to maximize computational efficiency. Some indication of the accuracy of this model
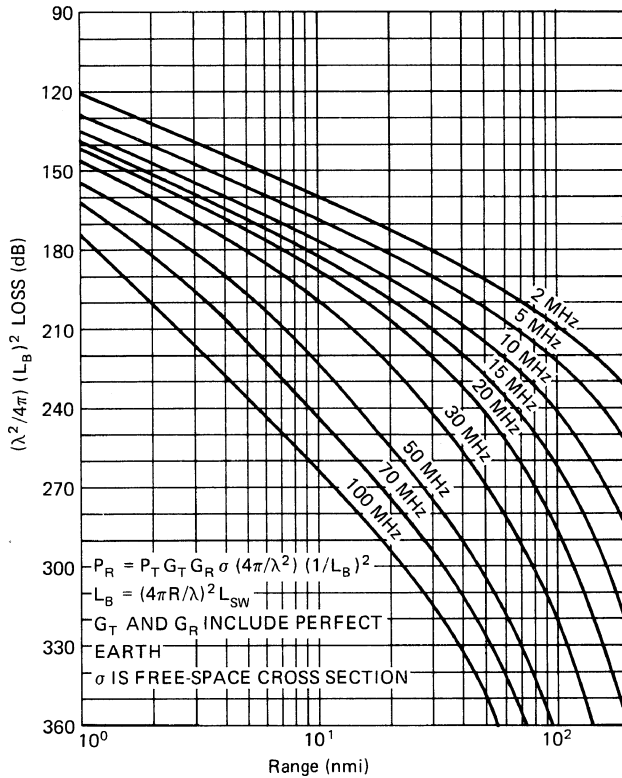
FIGURE 20.40 Curves of propagation loss versus range, as used for estimating surface wave radar performance. The surface is assumed to be smooth, target and antenna heights are 2 m, conductivity is taken as 5 S/m, and the dielectric constant is 80.

can be found in Figure 20.41, which compares GRWAVE predictions with experimental measurements of the signal strength received at a shore-based HFSWR when the transmitter was carried by a small boat traveling out to a range of ~110 km.[156] To avoid peripheral issues concerning antennas, the GRWAVE curves have been arbitrarily normalized here to align with the measurements at a range of 40 km. It is clear that, with this normalization, the predictions match reasonably well over the whole range extent, with small but systematic departures. GRWAVE seems to underestimate attenuation slightly at 7.72 MHz but over-estimate at 12.42 MHz. The sea roughness in this case was low (sea state 1–2). The impact of sea roughness on signal amplitude can be taken into account by using the expressions for roughness loss derived by Barrick.[159]

Another surface wave propagation modeling code has been developed by Sevgi,[160] paying particular attention to the calculation of propagation over hybrid paths with multiple islands.

The effect of the time-varying sea roughness on the signal phase and wavefront structure, manifested in the time delay, doppler spectrum, and direction-of-arrival spectrum of the received signal, can be computed using the multiple scattering theory of Anderson et al.[161]

GROUND WAVE PROPAGATION

GRWAVE MODEL ——— POL = V

ILUKA DATA ········· NORMALISED AT 40 km
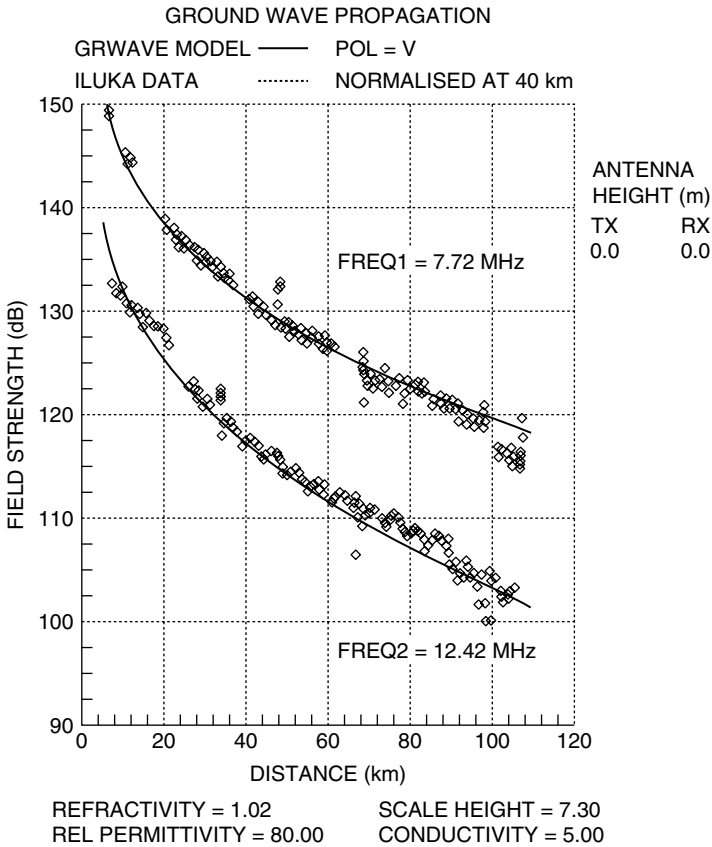
FIGURE 20.41 Experimental measurements of one-way surface wave attenuation, compared with GRWAVE predictions. Note the fluctuations due to scalloping loss as the source moved through FFT range bins.

Scattering: Targets and Clutter. The discussion of HF RCS and sea clutter in Sections 20.7 and 20.8 applies equally to HFSWR; indeed, the absence of the corrupting effects of the ionosphere provides even greater scope for exploiting the scattered signals. Furthermore, although the increased rate of decay of the surface wave at higher frequencies imposes a limit on the range of frequencies that might be used to detect a target at a given range, the situation is by no means as restrictive as for skywave propagation. This raises the possibility of exploiting multiple frequencies more effectively, so as to extract additional target and sea-state information and unmask targets hidden in clutter.

A compelling example is presented in Figure 20.42, where a range cell containing a ship target traveling at a speed of 13 knots has been interrogated at eight radar frequencies and the resulting doppler spectra plotted in a nested display.

The two columns of plots show received power versus doppler frequency for the eight operating frequencies as labeled, and for the target approaching (right column) and receding (left column). The abscissa units are in doppler normalized to
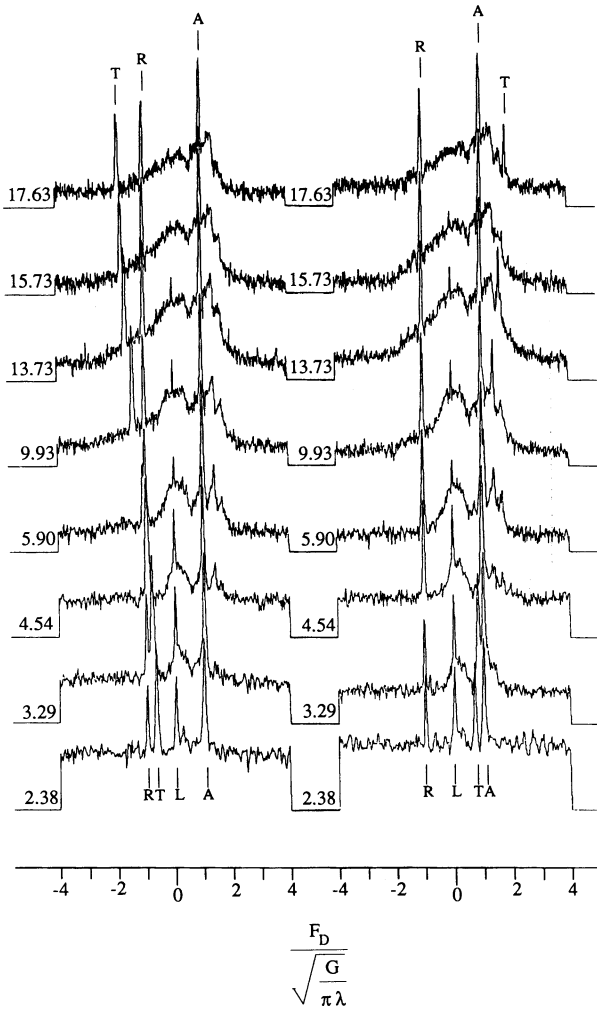
FIGURE 20.42 Multifrequency HFSWR doppler spectra showing the different frequency dependence of (i) target and (ii) clutter spectrum characteristics. The target T is shown when approaching (right) and receding (left) in the presence of the sea echo, with Bragg peaks marked A for approaching and R for receding. The curves plot received power versus normalized doppler (i.e., in units of the Bragg frequency) for eight radar operating frequencies. The peak at zero frequency is due to a stationary target in an antenna sidelobe.

the resonant wave or Bragg frequency; therefore, the resonant wave responses peak at ±1. The amplitude range for each plot is 60 dB. The narrow peaks at zero doppler frequency are due to land in an antenna sidelobe. The target doppler and Bragg line frequency coincide at a radar frequency of 4.93 MHz; the target doppler lies between the Bragg lines for radar frequencies below that frequency and outside them for

frequencies above. The positive doppler resonant wave peak is about 20 dB larger than the negative doppler peak, indicating a sea driven by winds blowing toward the radar. The processing used in developing these displays was 200-s CIT and 30-min averaging.

Performance Modeling. Examples of HFSWR system performance modeling[160,162] generally follow the precepts described in Section 20.12. The main difference here is the availability of path-loss descriptors such as those shown in Figure 20.40. For example, consider a radar at 5 MHz with an average power of 10 kW (40 dBW), a transmit-receive antenna gain product of 15 dB, and a target at 100 nmi with an RCS of 20 dBsm; then the received power is

$$P_r = 40 + 15 + 20 - 222 = -147\,dBW$$

By using the January nighttime noise as given in Figure 20.19*b*,

$$SNR = P_r - N = -147 + 153 = 6\,dB$$

and if 10 s coherent processing time is used,

$$SNR = 16\,dB$$

As noted earlier, propagation loss accelerates rapidly with distance, especially at higher frequencies, while atmospheric and surface roughness effects will accumulate and contamination of the surface wave return with echoes received via skywave paths will become increasingly severe, so quantitative performance predictions at long ranges, beyond ~200 km, should be treated with caution.

REFERENCES

1. A. H. Taylor and E. O. Hulbert, "The propagation of radio waves over the earth," *Physical Review*, vol. 27, February 1926.

2. L. A. Gebhard, "Evolution of naval radio-electronics and contributions of the Naval Research Laboratory," Naval Res. Lab. Rept. 8300, 1979.

3. J. M. Headrick and M. I. Skolnik, "Over-the-Horizon Radar in the HF Band," *Proc. IEEE*, vol. 62, pp. 664–673, June 1974.

4. D. A. Boutacoff, "Backscatter radar extends early warning times," *Defense Electronics.*, vol. 17, pp. 71–83, May 1985.

5. Guest editorial and invited papers in special issue on high-frequency and ice mapping and ship location, *IEEE J. Oceanic Eng.*, vol. OE-11, April 1986.

6. J. R. Barnum, "Ship detection with high resolution HF skywave radar," *ibid.*, pp. 196–210, April 1986.

7. J. M. Headrick, "Looking over the horizon," *IEEE Spectrum*, vol. 27, pp. 36–39, July 1990.

8. D. H. Sinnott, "The Jindalee over-the-horizon radar system," *Conf. Air Power in the Defence of Australia*, Australian National University, Research School of Pacific Studies, Strategic and Defence Studies Centre, Canberra, Australia, July 14–18, 1986.

9. J. Wylder, "The frontier for sensor technology," *Signal*, vol. 41, pp. 73–76, 1987.

10. V. A. Yakunin, F. F. Evstratov, F. I. Shustov, V. A. Alebastrov, and Y. I. Abramovich, "Thirty years of eastern OTH radars: history, achievements and forecast," *L'Onde Electrique*, vol. 74, no. 3, May–June 1994.

11. C. Goutelard, "The NOSTRADAMUS project: French OTH-B radar design studies," *47th AGARD Symposium on 'Use or Reduction of Propagation and Noise Effects in Distributed Military Systems'*, AGARD CP-488 (Supp.), Greece, October 1990.

12. C. Goutelard, "STUDIO father of NOSTRADAMUS. Some considerations on the limits of detection possibilities of HF radars," *Int. Conf. HF Radio Systems and Techniques*, IEE Conference Publication no. 474, July 2000.

13. V. Bazin, J. P. Molinie, J. Munoz, P. Dorey, S. Saillant, G. Auffray, V. Rannou, and M. Lesturgie, "A general presentation about the OTH-Radar NOSTRADAMUS," *IEEE Radar Conference*, Syracuse, NY, May 2006. Also reprinted in *IEEE AES Systems Magazine*, vol. 21, no. 10, pp. 3–11, October 2006.

14. Zhou Wenyu and Mao Xu, "Bistatic FMCW OTH-B experimental radar," *Proc. Int. Conf. Radar ICR-91*, China Institute of Electronics, 1991, pp. 138–141.

15. Guest editorial and invited papers reviewing OTH radar technology, with emphasis on recent progress, *Radio Science*, vol. 33, July–August 1998.

16. A. A. Kolosov (ed.), *Fundamentals of Over-the-Horizon Radar*, in Russian, Radio i svyaz, 1984. Also a translation by W. F. Barton, Norwood, MA: Artech House, 1987.

17. R. A. Greenwald, K. B. Baker, R. A. Hutchins, and C. Hanuise, "An HF phased array radar for studying small-scale structure in the high latitude ionosphere," *Radio Science*, vol. 20, pp. 63–79, January–February 1985.

18. P. A. Bernhardt, G. Ganguli, M. C. Kelley, and W. E. Swartz, "Enhanced radar backscatter from space shuttle exhaust in the ionosphere," *J. Geophys. Res.*, vol. 100, pp. 23,811–23,818, 1995.

19. R. M. Thomas, P. S. Whitham, and W. G. Elford, "Response of high frequency radar to meteor backscatter," *J. Atmos. Terr. Phys.*, vol. 50, pp. 703–724, 1988.

20. A. Cameron, "The Jindalee operational radar network: its architecture and surveillance capability," *Proc. IEEE Int. Radar Conf.*, 1995, pp. 692–697.

21. K. Davies, *Ionospheric Radio,* London: P. Peregrinus, 1990.

22. J. Thomason, G. Skaggs, and J. Lloyd, "A global ionospheric model," Naval Res. Lab. Rept. 8321, August 20, 1979.

23. K. Hocke and K. Schlegel, "A Review of atmospheric gravity waves and travelling ionospheric disturbances: 1982–1995," *Annales Geophysicae*, vol. 14, pp. 917–940, 1996.

24. A. Bourdillon, J. Delloue, and J. Parent, "Effects of geomagnetic pulsations on the doppler shift of HF backscatter radar echoes," *Radio Science*, vol. 24, pp. 183–195, 1989.

25. B.G. Fejer and M. C. Kelley, "Ionospheric irregularities," *Rev. Geophys. and Space Phys.*, vol. 18, pp. 401–454, 1980.

26. C.-S. Huang, M. C. Kelley, and D. L. Hysell, "Nonlinear Rayleigh-Taylor instabilities, atmospheric gravity waves, and equatorial spread F," *J. Geophys. Res.*, vol. 9, pp. 15,631–15,642, 1993.

27. D. L. Lucas and G. W. Haydon, "Predicting statistical performance indexes for high frequency telecommunications systems," ESSA Tech. Rept. IER 1 ITSA 1*,* U.S. Department of Commerce, 1966.

28. A. L. Barghausen, J. W. Finney, L. L. Proctor, and L. D. Schultz, "Predicting long-term operational parameters of high-frequency sky-wave communications systems," ESSA Tech. Rept. ERL 110-ITS 78, U.S. Department of Commerce, 1969.

29. J. M. Headrick, J. F. Thomason, D. L. Lucas, S. McCammon, R. Hanson, and J. L. Lloyd, "Virtual path tracing for HF Radar including an ionospheric model," Naval Res. Lab. Memo. Rept. 2226, March 1971.

30. L. R., Teters, J. L. Lloyd, G. W. Haydon, and D. L. Lucas, "Estimating the performance of telecommunication systems using the ionospheric transmission channel—ionospheric communications analysis and prediction program users manual," Nat. Telecom. Inf. Adm. NTIA Rept. 83–127, July 1983.

31. V. E. Hatfield, "HF communications predictions 1978 (An economical up-to-date computer code, AMBCOM)," *Solar Terrestrial Production Proc.*, vol. 4, in *Prediction of Terrestrial Effects of Solar Activity*, R. F. Donnelley (ed.), National Oceanic and Atmospheric Administration, 1980.

32. D. Lucas, G. Pinson, and R. Pilon, "Some results of RADARC-2 equatorial spread doppler clutter predictions," *Proc. 7th Int. Ionospheric Effects Symp*., Alexandria, Virginia, pp. 2A5-1–2A5-8, May 1993.

33. D. L. Lucas, "Ionospheric parameters used in predicting the performance of high frequency skywave circuits," Interim Report on NRL Contract N00014-87-K-20009, Account 153-6943, University of Colorado, Boulder, April 15, 1987.

34. D. C. Miller and J. Gibbs, "Ionospheric analysis and ionospheric modeling," AFCRL Tech. Rept. 75-549, July 1975.

35. D. Bilitza, "International reference ionosphere," http://modelweb.gsfc.nasa.gov/ionos/iri.html.

36. Index of /models/ionospheric/iri/iri2001, http://nssdcftp.gsfc.nasa.gov/models/ionospheric/iri/iri2001.

37. A. G. Kim, Z. F. Zumbrava, V. P. Grozov, G. V. Kotovich, Y. S. Mikhaylov, and A. V. Oinats, "The correction technique for IRI model on the basis of oblique sounding data and simulation of ionospheric disturbance parameters," *Proc. XXVIIIth URSI General Assembly*, New Delhi, October 2005.

38. R. E. Daniell, Jr. and D. N. Anderson, "PIM model 1995," http://modelweb.gsfc.nasa.gov/ionos/pim.html.

39. Parameterized Ionospheric Model, Computational Physics, http://www.cpi.com/products/pim/.

40. R.E. Daniell, L.D. Brown, D. N. Anderson, M. W. Fox, P. H. Doherty, D. T. Decker, J. J. Sojka, and R. W. Schunk, "Parameterized ionospheric model: A global ionospheric parameterization based on first principle models," *Radio Science*, vol. 30, pp. 1499–1510, 1995.

41. R. E. Daniell, "PRISM: assimilating disparate data types for improved low latitude ionospheric specification," presented at the Ionospheric Determination and Specification for Ocean Altimetry and GPS Surface Reflection Workshop at the Jet Propulsion Laboratory, Pasadena, CA, 2–4 December 1997.

42. D. N. Anderson, J. M. Forbes, and M. Codrescu, "A fully analytical, low- and middle-latitude ionospheric model," *J. Geophys. Res*. vol. 94, pp. 1520–1524, 1989.

43. Global Assimilation of Ionospheric Measurements, Park City, Utah, 2001, http://gaim.cass.usu.edu/GAIM/htdocs/present.htm.

44. Global Assimilative Ionospheric Model, JPL, http://iono.jpl.nasa.gov/gaim/index.html.

45. J. D. Huba, G. Joyce, and J. A. Fedder, "SAMI2 (Sami2 is another model of the ionosphere), A new low-latitude ionosphere model," *J. Geophys. Res*., vol. 105, 23,035–23053, 2000.

46. B. Khattatov, M. Murphy, M. Gnedin, T. Fuller- Rowell, and V. Yudin, "Advanced modeling of the ionosphere and upper atmosphere," *Environmental Research Technologies Report*, A550924, June 2004.

47. J. K. Hill, "Exact ray paths in a multisegment quasi-parabolic ionosphere," *Radio Science*, vol. 14, pp. 855–861, 1979.

48. T. A. Croft and H. Hoogasian, "Exact ray calculations in a quasi-parabolic ionosphere with no Magnetic Field," *Radio Science*, vol. 3, pp. 69–74, 1968.

49. R. J. Newton, P. L. Dyson, and J. A. Bennett, "Analytic ray parameters for the quasi-cubic segment model of the ionosphere," *Radio Science*, vol. 32, pp. 567–578, 1997.

50. R. M. Jones and J. J. Stephenson, "A versatile three-dimensional ray tracing computer program for radio waves in the ionosphere," Office Telecom. Rept. 75–76, October 1975.

51. C. J. Coleman, "A general purpose ionospheric ray-tracing procedure," DSTO Technical Report SRL-0131-TR, 1993.

52. Jari Perkiömäki, "High-frequency (HF) ionospheric communications analysis and prediction," VOACAP Quick Guide, http://www.voacap.com/.

53. "Advanced stand alone prediction system," IPS Radio and Space Services, The Australian Space Weather Agency, http://www.ips.gov.au/Products_and_Services/1/1.

54. PROPLAB-PRO version 2.0, http://www.spacew.com/www/proplab.html.

55. B. T. Root and J. M. Headrick, "Comparison of RADARC High-frequency radar performance prediction model and ROTHR Amchitka data," Naval Res. Lab. Rept. NRL/MR/5320-93-7181, July 1993.

56. J. M. Headrick, B. T. Root, and J. F. Thomason, "RADARC model comparisons with Amchitka radar data," *Radio Science*, vol. 30, pp. 729–737, May–June 1995.

57. "New wind model," HWM 93, http://nssdcftp.gsfc.nasa.gov/models/atmospheric/hwm93/hwm93.txt.

58. J. A. Secan, R. M. Bussey, E. J. Fremouw, and Sa. Basu, "An improved model of equatorial scintillation," *Radio Science, 30,* 607–617, 1995.

59. A. V. Gurevich, *Nonlinear Phenomena in the Ionosphere,* New York: Springer-Verlag, 1978.

60. V. A. Alebastrov, A. T. Mal'tsev, V. M. Oros, A. G. Shlionskiy, and O. I. Yarko, "Some characteristics of echo signals," *Telecomm. and Radio Eng*., vol. 48, pp. 92–95, 1993.

61. V. G. Somov, V. A. Leusenko, V. N. Tyapkin, and G. Ya. Shaidurov, "Effect of nonlinear and focusing ionospheric properties on qualitative characteristics of radar in the decametric-wave band," *J. Comm. Technology and Electronics*, vol. 48, pp. 850–858, 2003.

62. ITT Avionics Division, Electro-Physics Laboratories, EPL Model ATL-75 Transmitter for Radar and Communication, IR&D Project Rept. 274, Results of performance measurements, January 1975.

63. D. J. Hoft and Fuat Agi, "Solid state transmitters for modern radar applications," *CIE Int. Radar Conf. Record, Beijing,* November 4–7, 1986, pp. 775–781.

64. F. A. Raab, P. Asbeck, S. Cripps, P. B. Kenington, Z. B. Popovic, N. Pothecary, J. F. Sevic, and N. O. Sokal, "Power amplifiers and transmitters for RF and microwave," *IEEE Trans. Microwave Theor. and Tech.*, vol. 50, pp. 814–826, March 2002.

65. D. J. Netherway and Carson, C. T., "Impedance and scattering matrices of a wideband HF phased Array," *J. Electron. Eng. Aust*., vol. 6, pp. 29–39, 1986.

66. Guest editorial and invited papers in special issue on shortwave broadcasting, *IEEE Trans. Broadcast.,* vol. 34, June 1988.

67. R. C. Johnson and H. Jasik (eds.), *Antenna Engineering Handbook,* 3rd Ed., New York: McGraw-Hill Book Company, 1993.

68. A. G. Kurashov (ed.), *Shortwave Antennas,* 2 Ed., in Russian, *Radio i svyaz,* January 1985.

69. S. J. Anderson, "Limits to the extraction of information from multi-hop skywave radar signals," *Proc. Int. Radar Conf*., Adelaide, September 2003, pp. 497–503.

70. S. J. Anderson, "The doppler structure of diffusely-scattered skywave radar echoes," *Proc. Int. Radar Conf*., Toulouse, October 2004.

71. S. J. Anderson, "Target classification, recognition and identification with HF radar, proc. NATO Research and Technology Agency," *Sensors and Electronics Technology Panel Symposium SET-080/RSY17/RFT 'TARGET IDENTIFICATION AND RECOGNITION USING RF SYSTEMS'*, Oslo, Norway, October 2004.

72. E. K. Walton and J. D. Young, "The Ohio State University compact radar cross section measurement range," *IEEE Trans. Ant. Prop.,* vol. AP-32, pp. 1218–1223, November 1984.

73. G. J. Burke and A. J. Poggio, "Numerical electromagnetic code (nec)-method of moments," NOSC Tech. Doc. 116, 1981.

74. R. W. Bogle and D. B. Trizna, "Small boat radar cross sections," Naval Res. Lab. Memo. Rept. 3322, July 1976.

75. R. Dinger, E. Nelson, S. Anderson, F. Earl, and M. Tyler, "High frequency radar cross section measurements of surrogate go-fast boats in Darwin, Australia," *SPAWAR System Center Tech. Rept. 1805*, September 1999.

76. S. J. Anderson, "Remote sensing with the Jindalee Skywave Radar," *IEEE J. Ocean. Eng.,* vol. OE- II, pp. 158–163, April 1986.

77. J. R. Barnum and E. E. Simpson, "Over-the-horizon radar target registration improvement by terrain feature localization," *Radio Science*, vol. 33, pp. 1067, July–August 1998.

78. D. E., Barrick, J. M. Headrick, R. W. Bogle, and D. D. Crombie, "Sea backscatter at HF: Interpretation and utilization of the echo," *Proc. IEEE,* vol. 62, pp. 673–680, June 1974.

79. S. O. Rice, "Reflection of electromagnetic waves from slightly rough surfaces," in *Theory of Electromagnetic Waves,* M. Kline (ed.), New York: Interscience Publishers, 1951, pp. 351–378.

80. D. E. Barrick, "First order theory and analysis of MF/HF/VHF scatter from the sea," *IEEE Trans.,* vol. AP-20, pp. 2–10, January 1972.

81. D. E. Barrick, "Remote sensing of sea state by radar," Chapter 12 in *Remote Sensing of the Troposphere*, V.E. Derr (ed.), Boulder, CO: NOAA/Environmental Research Laboratories, 1972, pp. 12.1–12.6.

82. D. D. Crombie, "Doppler spectrum of the sea echo at 13.56 Mcs," *Nature,* vol. 175, pp. 681–682, 1955.

83. J. W. Maresca, Jr. and J.R. Barnum, "Theoretical limitation of the sea on the detection of low doppler targets by over-the-horizon radar," *IEEE Trans. Ant. Prop.*, vol. AP-30, pp. 837–845, 1982.

84. W. J. Pierson and L. Moskowitz, "A proposed spectral form for fully developed wind seas based on the similarity theory of S. A. Kitaigordskii," *J. Geophys. Res.,* vol. 69, no. 24, pp. 5181–5190, 1964.

85. K. Hasselmann, D. B. Ross, P. Muller, and W. Sell, "A parametric wave prediction model," *J. Phys. Oceanogr,* vol. 6, pp. 200–228, 1976.

86. T. Elfouhaily, B. Chapron, K. Katsaros, and D. Vandemark, "A unified directional spectrum for long and short wind-driven waves," *J. Geophys. Res.,* vol. 102, pp. 15782–15796, 1997.

87. A. E. Long and D. B. Trizna, "Mapping of North Atlantic winds by HF radar sea backscatter interpretation," *IEEE Trans. Ant. Prop.,* vol. AP-21, pp. 680–685, September 1973.

88. L. R. Wyatt, "A relaxation method for integral inversion applied to HF radar measurement of the ocean wave directional spectrum," *Int. J. Remote Sens.,* vol. 11, pp. 1481–1494, August 1990.

89. Y. Hisaki, "Nonlinear inversion of the integral equation to estimate ocean wave spectra from HF radar," *Radio Science,* vol. 31, pp. 25–39, 1996.

90. N. Hashimoto and M. Tokuda, "A Bayesian approach for estimation of directional wave spectra with HF radar," *Coastal Eng. J.*, vol. 41, pp.137–149, 1999.

91. D. E. Barrick, "Extraction of wave parameters from measured hf radar sea-echo spectra," *Radio Science,* vol, 12, no. 3, p. 415, 1977.

92. T. M. Georges, J. A. Harlan, R. R. Leben, and R. A. Lematta, "A test of ocean surface current mapping with over-the-horizon radar," *IEEE Trans. Geosci. and Rem. Sens.*, vol. 36. pp. 101–110, 1998.

93. H. L. Tolman, WAVEWATCH III, National Weather Service, http://polar.ncep.noaa.gov/waves/wavewatch/wavewatch.html.

94. J. L. Ahearn, S. R. Curley, J. M. Headrick, and D. B. Trizna, "Tests of remote skywave measurement of ocean surface conditions," *Proc. IEEE,* vol. 62, pp. 681–686, June 1974.

95. D. B. Trizna and J. M. Headrick, "Ionospheric effects on HF over-the-horizon radar," in Goodman, J. M. (ed.), *Proc. Effect Ionosphere on Radiowave Systems,* ONR/AFGL-sponsored, April 14–16, 1961, pp. 262–272.

96. J. Parent and A. Bourdillon, "A Method to correct HF skywave backscattered signals for ionospheric frequency modulation," *IEEE Trans. Ant. Prop.*, vol. AP-36, pp. 127–135, 1987.

97. S. J. Anderson and Y.I. Abramovich, "A unified approach to detection, classification and correction of ionospheric distortion in HF skywave radar systems," *Radio Science*, vol. 33, pp.1055–1067, July–August 1998.

98. D. B. Trizna, "Estimation of the sea surface radar cross section at HF from second-order doppler spectrum characteristics," Naval Res. Lab. Rept. 8579, May 1982.

99. R. O. Pilon and J. M. Headrick, "Estimating the scattering coefficient of the ocean surface for high-frequency over-the-horizon radar," Naval Res. Lab. Memo. Rept. 5741, May 1986.

100. J. Jones and P. Brown, "Sporadic meteor radiant distributions: orbital survey results," *Mon. Not. Roy. Astr. Soc*., vol. 265, pp. 524–-532, 1993.

101. M. A. Cervera and W. G. Elford., "The meteor response function: theory and application to narrow beam MST radar," *Planet. Space Sci.*, vol. 52, pp. 591–602, 2004.

102. P. Brown and J. Jones, "A determination of the strengths of the sporadic radio-meteor sources," *Earth, Moon and Planets*, vol. 68, pp. 223–-245, 1995.

103. M. A. Cervera, D. A. Holdsworth, I. M. Reid, and M. Tsutsumi, "The meteor radar response function: Application to the interpretation of meteor backscatter at medium frequency," *J. Geophys. Res.*, vol. A109, pp. 11309, 2004.

104. T. J. Elkins, "A model for high frequency radar auroral clutter," RADC Rept. TR-80-122, March 1980.

105. "World distribution and characteristics of atmospheric radio noise," CCIR Rept. 322, CCIR (International Radio Consultative Committee), International Telecommunications Union, editions 1964, 1983, and 1988.

106. A. D. Spaulding and J. S. Washburn, "Atmospheric radio noise: Worldwide levels and other characteristics," NTIA Rept. 85-173, National Telecommunications and Information Administration, April 1985.

107. D. L. Lucas and J. D. Harper, "A numerical representation of CCIR Report 322 high frequency (3-30 Mcs) atmospheric radio noise data," Nat. Bur. Stand. Note 318, August 5, 1965.

108. D. B. Sailors, "Discrepancy in the International Radio Consultative Committee Report 322-3 radio noise model: The probable cause," *Radio Science*, vol. 30, pp. 713–728, 1995.

109. B. J. Northey and P. S. Whitham, "A comparison of DSTO and DERA HF background Noise measuring systems with the International Radio Consultative Committee (CCIR) model data," DSTO Technical Report DSTO-TR-0855, November 2000.

110. M. Kotaki and C. Katoh, "The global distribution of thunderstorm activity observed by the ionosphere satellite (ISS-b)," *J.Atmos. Terr. Phys.*, vol. 45, pp. 833–850, 1984.

111. C. J. Coleman, "A direction-sensitive model of atmospheric noise and its application to the analysis of HF receiving antennas," *Radio Science*, vol. 37, pp. 3.1–3.10, 2002.

112. Yu. I. Abramovich, N. K. Spencer, and S. J. Anderson, "Experimental study of the spatial dynamics of environmental noise for a surface-wave OTHR application," *Proc. 8th Int. Conf. HF Radio Systems and Techniques*, IEE Conference Publication no. 474, Guildford, UK, July 2000, pp. 357–362.

113. L. E. Sweeney, "Spatial properties of ionospheric radio propagation as determined with half-degree azimuthal resolution," Stanford Electron. Lab. Tech. Rept. 155 SU- SEL-70-034, Stanford University, June 1970.

114. J. T. Lynch, "Aperture synthesis for HF radio signals propagated via the F-layer of the ionosphere," Stanford Electron. Lab. Tech. Rept. 161 SU-SEL-70-066, Stanford University, September 1970.

115. D. H. Sinnott and G. R. Haack, "The use of overlapped subarray techniques in simultaneous receive beam arrays," *Proc. Antenna Appl. Symp.*, University of Illinois, 1983.

116. S. J. Anderson, Y. I. Abramovich, and W-M. Boerner, "Measuring polarization dynamics of the generalized HF skywave channel transfer function," *Proc. Int Symp. Ant. and Prop.*, ISAP 2000, Japan, August 2000.

117. T. H. Pearce, "Receiving array design for over-the-horizon radar," *GEC J. Technology*, vol. 15, pp. 47–55, 1998.

118. G. F. Earl and M. J. Whitington, "HF radar ADC dynamic range requirements," *3rd Int. Conf. on Advanced A/D and D/A Conversion Techniques*, July 1999.

119. G. F. Earl, "FMCW waveform generator requirements for ionospheric over-the-horizon radar," *Radio Science*, vol. 33, pp. 1069–1076, 1998.

120. G. F. Earl, "Receiving system linearity requirements for HF radar," *IEEE Trans. Instrum. Meas.*, vol. 40, pp. 1038–1041, 1991.

121. G. F. Earl, P. C. Kerr, and P. M. Roberts, "OTH radar receiving system design using synoptic HF environmental database," *Proc. 5th Int. Conf. HF Radio Systems and Techniques*, July 1991, pp. 48–53.

122. S. J. Anderson, "Simulation and modeling for the Jindalee over-the-horizon radar," *Math. and Comp. in Simulation*, vol. 27, pp. 241–248, 1985.

123. G. F. Earl, "Consideration of reciprocal mixing in HF OTH radar design," *Proc. 7th Int. Conf. HF Radio Systems and Techniques*, IEE Conference Publication no. 441, July 1997, pp. 256–259.

124. G. F. Earl, "HF radar receiving system image rejection requirements," *Proc. 6th Int. Conf. HF Radio Systems and Techniques*, September 1995, pp. 128–132.

125. T. H. Pearce, "Calibration of a large receiving array for HF radar," *Proc. Int. Conf. HF Radio Systems and Techniques*, IEE Conference Publication No. 411, July 1997, pp. 260–264.

126. D. M. Fernandez J. Vesecky, and C. Teague, "Calibration of HF radar systems with ships of opportunity," *Proc. of the 2003 IEEE Int. Geoscience and Remote Sensing Symp.*, New York, July 2003, pp. 4271–4273.

127. I. S. D. Solomon, D. A. Gray, Y. I. Abramovich, and S. J. Anderson, "Over-the-horizon radar array calibration using echoes from ionized meteor trails," *IEE Proc. Radar, Sonar, and Navigation*, vol. 145, pp. 173–180, June 1998.

128. I. S. D. Solomon, D. A. Gray, Y. I. Abramovich, and S. J. Anderson, "Receiver array calibration using disparate sources," *IEEE Trans. Ant. Prop.*, vol. 47, pp. 496–505, March 1999.

129. G. J. Frazer and Y. I. Abramovich, "Quantifying multi-channel receiver calibration," DSTO Technical Report DSTO-TR-1152, 2001.

130. G. J. Frazer and S. J. Anderson, "Wigner-Ville analysis of HF radar measurements of an accelerating target," *Proc. 5th Int. Symp. Signal Proc. Appl.*, Brisbane, August 1999, pp. 317–320.

131. Y. Zhang, M. G. Amin, and G. J. Frazer, "High-resolution time-frequency distributions for maneuvering target detection in over-the-horizon radars," *IEE Proc. Radar, Sonar, and Navigation*, vol. 150, pp. 299–304, 2003.

132. T. Thayaparan and S. Kennedy, "Detection of a maneuvering air target in sea-clutter using joint time-frequency analysis techniques," *IEE Proc. Radar, Sonar, and Navigation*, vol. 151, pp. 19–30, February 2004.

133. G. J. Frazer and S. J. Anderson, "Estimating the frequency interval of a regularly spaced multi-component harmonic line signal in colored noise," in *Defence Applications of Signal Processing*, D. A. Cochran, B. Moran, and L. White (eds.), New York: Elsevier, 2001, pp. 76–86.

134. G. Fabrizio, L. Scharf, A. Farina, and M. Turley, "Ship detection with HF surface-wave radar using short integration times," *Proc. Int. Conf. Radar 2004*, Toulouse, 2004.

135. D. O. Carhoun, J. D. R. Kramer Jr., and P. K. Rashogi, "Adaptive cancellation of atmospheric noise and ionospheric clutter for high frequency radar," MITRE Report, MTR 95B0000112, September 1995.

136. Y. I. Abramovich, S. J. Anderson, A. Y. Gorokhov, and N. K. Spencer, "Stochastically constrained spatial and spatio-temporal adaptive processing for nonstationary hot-clutter cancellation," in *Applications of Space-time Adaptive Processing*, R. K. Klemm (ed.), London: Springer, 2004, pp. 603–697.

137. Y. I. Abramovich, S. J. Anderson, A. Y. Gorokhov, and N. K. Spencer, "Stochastic constraints method in nonstationary hot clutter cancellation, part I: Fundamentals and supervised training applications," *IEEE Trans. AES*, vol. 34, pp. 1271–1292, October 1998.

138. Y. I. Abramovich, S. J. Anderson, and N. K. Spencer, "Stochastic-constraints method in nonstationary hot clutter cancellation, part II: Unsupervised training applications," *IEEE Trans. AES*, vol. 36, pp. 132–149, January 2000.

139. Y. I. Abramovich, V. N. Mikhaylyukov, and I. P. Malyavin, "Stabilisation of the autoregressive characteristics of spatial clutters in the case of nonstationary spatial filtering," *Sov. J. Commun. Technol. Electron.*, vol. 37, pp. 10–19, 1992, translation of *Radioteknika I Electronika*.

140. R. Anderson, S. Kraut, and J. L. Krolik, "Robust altitude estimation for over-the-horizon radar using a state-space multipath fading model," *IEEE Trans. AES*, vol. 39, pp. 192–201, January 2003.

141. D. J. Percival and K. A. B. White, "Multipath coordinate registration and track fusion for over-the-horizon radar," in *Defence Applications of Signal Processing*, D. A. Cochran, B. Moran, and L. White (eds.), Amsterdam: Elsevier, 2001, pp. 149–155.

142. Y. Bar-Shalom and T. E. Fortmann, *Tracking and Data Association*, New York: Academic Press, January 1988.

143. S. B. Colegrove and S. J. Davey, "PDAF with multiple clutter regions and target models," *IEEE Trans. AES*, vol. 39, pp. 110–124, January 2003.

144. J. L. Krolik and R. H. Anderson, "Maximum likelihood coordinate registration for over-the-horizon radar," *IEEE Trans. Sig. Proc.*, vol. 45, pp. 945–959, 1997.

145. M. G. Rutten and D. J. Percival, "Joint ionospheric and track target state estimation for multipath othr track fusion," *Proc. SPIE Conf. on Signal and Data Processing of Small Targets*, 2001, pp. 118–129.

146. R. H. Anderson and J. L. Krolik, "Track association for over-the-horizon radar with a statistical ionospheric model," *IEEE Trans. Sig. Proc.*, vol. 50, pp. 2632–2643, November 2002.

147. G. W. Pulford, "OTHR multipath tracking with uncertain coordinate registration," *IEEE Trans. AES*, vol. 40, pp. 38–56, 2004.

148. S. J. Anderson, F. J. Mei, and J. Peinan, "Enhanced OTHR ship detection via dual frequency operation," *Proc. China Institute of Electronics Int. Conf. on Radar*, Beijing, October 2001.

149. G. F. Earl and B. D. Ward, "Frequency management support for remote sea-state sensing using the JINDALEE skywave radar," *IEEE J. of Oceanic Engr.*, vol. OE-11, pp. 164–173, April 1986.

150. G. F. Earl and B. D. Ward, "The frequency management system of the Jindalee over-the-horizon backscatter HF radar," *Radio Science*, vol. 22, pp. 275–291, 1987.

151. R. Barnes, "Automated propagation advice for OTHR ship detection," *IEE Proc. Radar, Sonar, and Navigation*, vol. 143, pp. 53–63, February 1996.

152. D. L. Lucas, J. L. Lloyd, J. M. Headrick, and J. F. Thomason, "Computer techniques for planning and management of OTH radars," Naval Res. Lab. Memo. Rept. 2500, September 1972.

153. J. M. Headrick, "HF over-the-horizon radar," Chapter 24 in *Radar Handbook*, M. I. Skolnik (ed.), 2nd Ed., New York: McGraw-Hill, 1990.

154. J. M. Hudnall and S. W. Der, "HF-OTH radar performance results," Naval Res. Lab. Tech. Rept. NRL/MR/5325-93-7326, 1993.

155. R. Fante and S. Dhar, "A model for target detection with over-the-horizon radar," *IEEE Trans. AES*, vol. 26, pp. 68–83, January 1990.

156. L. A. Berry and M. E. Chrisman, "A FORTRAN program for calculation of ground wave propagation over homogeneous spherical earth for dipole antennas," Nat. Bur. Stand. Rept. 9178, 1966.

157. S. Rotheram, "Ground wave propagation, parts 1 and 2," *IEE Proc., Pt. F*, vol. 128, pp. 275–295, 1981.

158. S. J. Anderson, P. J. Edwards, P. Marrone, and Y. I. Abramovich, "Investigations with SECAR—A bistatic HF surface wave radar," *Proc. IEEE Int. Conf. on Radar, RADAR 2003*, Adelaide, September 2003.

159. D. E. Barrick, "Theory of HF and VHF propagation across the rough sea, pts. I and 2," *Radio Science,* vol. 6, pp. 517–533, May 1971.

160. L. Sevgi, *Complex Electromagnetic Problems and Numerical Simulation Approaches,* Hoboken, NJ: IEEE Press, 2003.

161. S. J. Anderson, J. Praschifka, and I. M. Fuks, "Multiple scattering of HF radiowaves propagating across the sea surface," *Waves in Random Media*, vol. 8, pp. 283–302, April 1998.

162. G. H. Millman and G. Nelson, "Surface wave HF radar for over-the-horizon detection," *Proc. IEEE Int. Radar Conf.*, 1980, pp. 106–112.